The interactions of viral matrix proteins with lipid membranes

FREETH, JAMES,ALEXANDER

The interactions of viral matrix proteins with lipid membranes

James Alexander Freeth

A thesis submitted in partial fulfilment of the requirements for the degree of Doctor of Philosophy

Department of Chemistry
Durham University

2014

The interactions of viral matrix proteins with lipid membranes

James Alexander Freeth

Abstract

This thesis describes the work undertaken to study the binding of lipid membranes by the viral matrix proteins hRSV-M and Influenza-A-M1.

hRSV-M was recombinantly expressed and purified. It was the subjected to analysis by Langmuir-Blodgett trough experiments, Brewster angle microscopy, Confocal microscopy of giant unilamellar vesicles (GUVs), and binding studies with lipid nanodiscs. These studies showed hRSV-M having a preference for interacting with negatively charged lipids, namely phosphatidylserine, and for having different behaviours in L_o and L_d phases of membranes.

During work on hRSV-M to improve its stability, it was discovered calcium stabilised the protein. This relationship was explored by ICPMS, differential scanning fluorimetry (DSF), circular dichroism (CD), mass spectrometry and microscale thermophoresis. This showed the hRSV-M is a calcium binding protein, containing two binding sites.

Influenza-A-M1 was cloned into a plasmid vector and subsequently expressed and purified. The stability and structure of the protein was probed by DSF and CD measurements. The lipid interactions of this protein were then also explored by Langmuir-Blodgett trough isotherms and GUV binding under confocal microscopy. These showed that M1 is able to bind to phosphatidylserine containing membranes and causes vesicle budding from those membranes.

Contents

List of Tables

List of Figures

List of abbreviations

BAM	Brewster Angle Microscopy
BSA	Bovine Serum Albumin
CD	Circular Dichroism
Chol	Cholesterol
Cryo-EM	Cryo-electron Microscopy
DNA	Deoxyribonucleic acid
DOPC	1,2-dioleoyl-sn-glycero-3-phosphocholine
DPPC	1,2-dipalmitoyl-sn-glycero-3-phosphocholine
DPPS	1,2-dipalmitoyl-sn-glycero-3-phospho-L-serine
dsDNA	Double Stranded Deoxyribonucleic acid
DSF	Differential Scanning Fluorimetry
FITC	Fluorescein isothiocyanate
FRET	Fluorescence Resonance Energy Transfer
GUV	Giant Unilamellar Vesicle
HCV	Hepatitis C Virus
HMPV	Human metapneumovirus
hRSV	Human Respiratory Syncytial Virus
ICPMS	Inductively coupled plasma mass spectrometry
IMAC	Immobilized Metal Ion Affinity Chromatography
IPTG	Isopropyl β-D-1-thiogalactopyranoside
ITO	Indium-Tin Oxide
MLV	Multi-Lamellar Vesicle
MSP	Membrane Scaffold Protein
NBD	7-nitrobenzofurazan
NDV	Newcastle Disease Virus
PBS	Phosphate buffered Saline
POPC	1-palmitoyl-2-oleoyl-sn-glycero-3-phosphocholine
POPS	1-palmitoyl-2-oleoyl-sn-glycero-3-phospho-L-serine
Rh-PE	1,2-dipalmitoyl-sn-glycero-3-phosphoethanolamine-N-(lissamine rhodamine B sulfonyl)
RNA	Ribonucleic acid
SAXS	Small Angle X-ray Scattering
SDS-PAGE	Sodium Dodecyl Sulfate Polyacrylamide gel electrophoresis
SM	Sphingomyelin
ssRNA	Single Stranded Ribonucleic acid
T_m	Melting Temperature
VLP	Virus-like Particle
vRNA	Viral Ribonucleic acid

Acknowledgments

First I would like to thank my supervisors, John Sanderson and Paul Yeo. I thank them for their guidance, kindness and infinite patience.

Thank you to Dr Jackie Mosely for her help with the mass spec of some difficult samples, to Dr Aruna Prakash for analysing the M-NBD samples for me. Also thanks you Christine Richardson of the EM unit for helping me through samples and providing an expert eye.

I'd like to thank all the students that have passed through our lab, and the groups of 229 and 216 for their friendship and advice. Special thanks go to Lisa Bergman-Bailey and Amy Fry, who helped in the collection of data for the isotherms, and making them a little less boring to do alone.

And finally thanks to my parents and brother for helping me through a difficult year.

1 Introduction

1.1 Viruses

Viruses are infectious biological agents found in all ecosystems and believed to have existed since the earliest organisms. A Virus by itself is not considered to be alive, but must infect another organism in order to reproduce and propagate itself further .[1] In general a virus consists of a genetic code in DNA or RNA surrounded by a nucleocapsid composed of structural proteins with other associated proteins involved in viral replication, fusion and budding. However, there is huge variation in different virus' shape, size, genetics and host organism. Viruses have been found to infect all classes of organisms including eukaryotes, prokaryotes and archaea. However, individual viruses are restricted to being able to infect a small range of hosts.

Broadly, viruses can be divided into 4 structural types. Helical viruses are those in which nucleocapsid proteins forms long oligomeric helical structures surrounding the genetic material inside the central hollow. This causes these viruses to form long filamentous structures. Icosahedral viruses have a symmetrical, almost spherical shell formed by identical nucleocapsid subunits. They consist of 20 triangular faces surrounding the central hollow containing the genetic material and other viral proteins. "Complex" viruses are those whose structures consist of different domains of varying constitution. A typical example of this is the structure of bacteriophages, which have an icosahedral head attached to a helical body segment with additional protein fibres stretching off it. The final type is enveloped viruses. In addition to a nucleocapsid, which may be of any of the above shapes, these viruses are surrounded by a membrane envelope derived from the host cell[1]. It is this class of virus that this project focuses on.

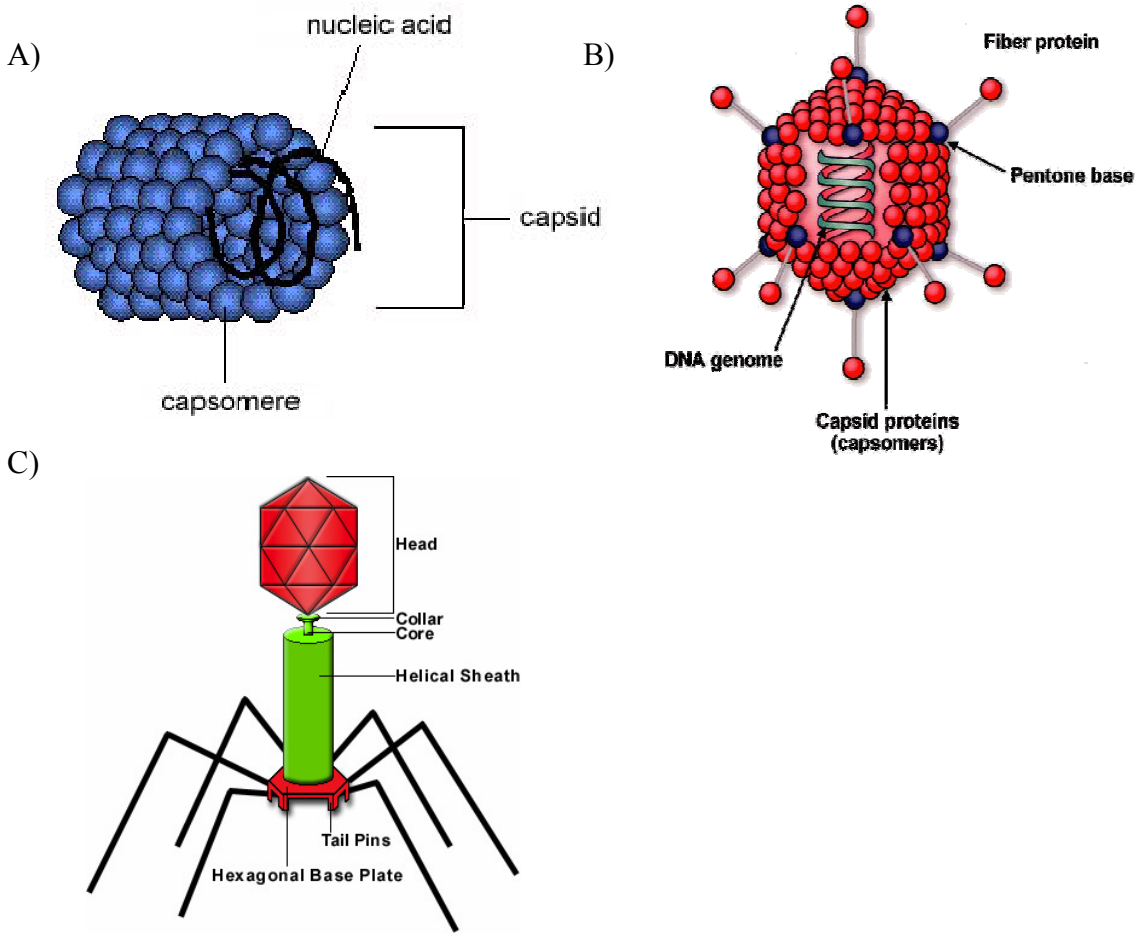

Figure 1 - Diagrams of typical A) Helical, B) Icosahedral and C) Bacteriophage viruses[2] (Reprinted with permission, Nature publishing group)

Enveloped viruses consist of 3 main parts; the genetic material, the capsid and the envelope, along with other associated proteins. The capsid consists of individual repeating units called capsomers, which themselves may be made up of one or more proteins. These units are held together non-covalently to form a solid shell around the virus genome. The function of the capsid is to protect the inner genome and associated proteins from damage, and also to act as a scaffold for other proteins to attach to. For example, receptor proteins attach to the surface of the non-enveloped Polio virus capsid to target the virus to nerve cells. The capsid can also bind to the genome to aid the correct assembly of intact virions. This capsid – genome complex is called the nucleocapsid. The size of the capsid is directly related to how much material the virus has to carry inside it. Viruses have evolved to use the smallest

capsid size possible to fit the genome inside. In the case of enveloped viruses, the capsid may also directly interact with the membranous envelope, or with intermediate proteins which in turn adsorb to the envelope.

The genomics of viruses are very diverse. The genome may consist of either DNA or RNA and in several different conformations. Viruses have been found with both double stranded and single stranded (+ or -) genomes, and genomes that must first undergo reverse transcription in order to be incorporated into the host genome. This variety has led to the Baltimore Classification system for viruses outlined in Table 1.

Class	Genome	Example Virus
I	dsDNA	Herpes Simplex Virus
II	(+)ssDNA	Parvovirus B19
III	dsRNA	Rotavirus
IV	(+)ssRNA	Hepatitis C Virus
V	(-)ssRNA	Influenzavirus A
VI	(+)ssRNA-RT	HIV
VII	dsDNA-RT	Hepatitis B

Table 1 - The Baltimore Classification system for viruses.[3]

The viruses being focused on in this project are of class IV and V, the single-stranded RNA viruses. Some example families of these are outlined in Table 2.

Class	Family	Example Virus	Capsid Shape	Enveloped / Naked State
IV	Picornaviridae	Poliovirus	Icosahedral	Naked
IV	Caliciviridae	Hepatitis E	Icosahedral	Naked
IV	Togaviridae	Rubella Virus	Icosahedral	Enveloped
IV	Flaviviridae	Hepatitis C Virus	Icosahedral	Enveloped
V	Orthomyxoviridae	Influenzavirus A	Helical	Enveloped
V	Paramyxoviridae	hRSV	Helical	Enveloped
V	Rhabdoviridae	Rabies	Helical	Enveloped
V	Filoviridae	Ebola Virus	Helical	Enveloped

Table 2 - Example Families of Class IV and V viruses and their structures.

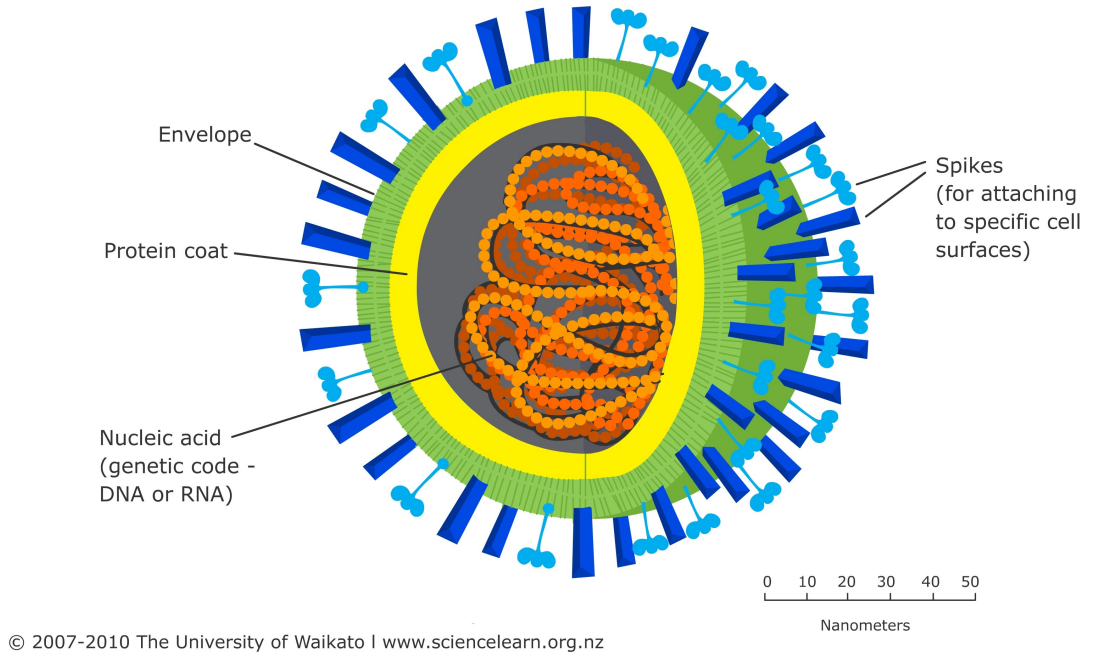

Figure 2 – Simplified structure of a typical enveloped virus. (© The University of Waikato)

The envelope surrounding an enveloped virus is a phospholipid bilayer that forms the outermost layer of the virion. It is derived from the host cell's plasma membrane, formed as the virus buds, and so the lipid composition is similar to the host cell. The membrane can have a number of viral glycoproteins imbedded in it, which then appear on the outside of the virion. Due to the host derived nature, the envelope may also carry host proteins with it, but many of these are displaced by the viral ones. The envelope is attached to the central virus structure either directly, or through matrix proteins which bind to the membrane and nucleocapsid, holding them together. It is these types of membrane binding proteins that this project will focus on. The presence of a lipid envelope does make the virus more susceptible to damage, however the host derived material can help the virus to evade detection by the host organisms immune system, and the fusion that occurs between the envelope and cell membranes can help with the entry of the virus into cells.

1.2 Enveloped Virus Lifecycle

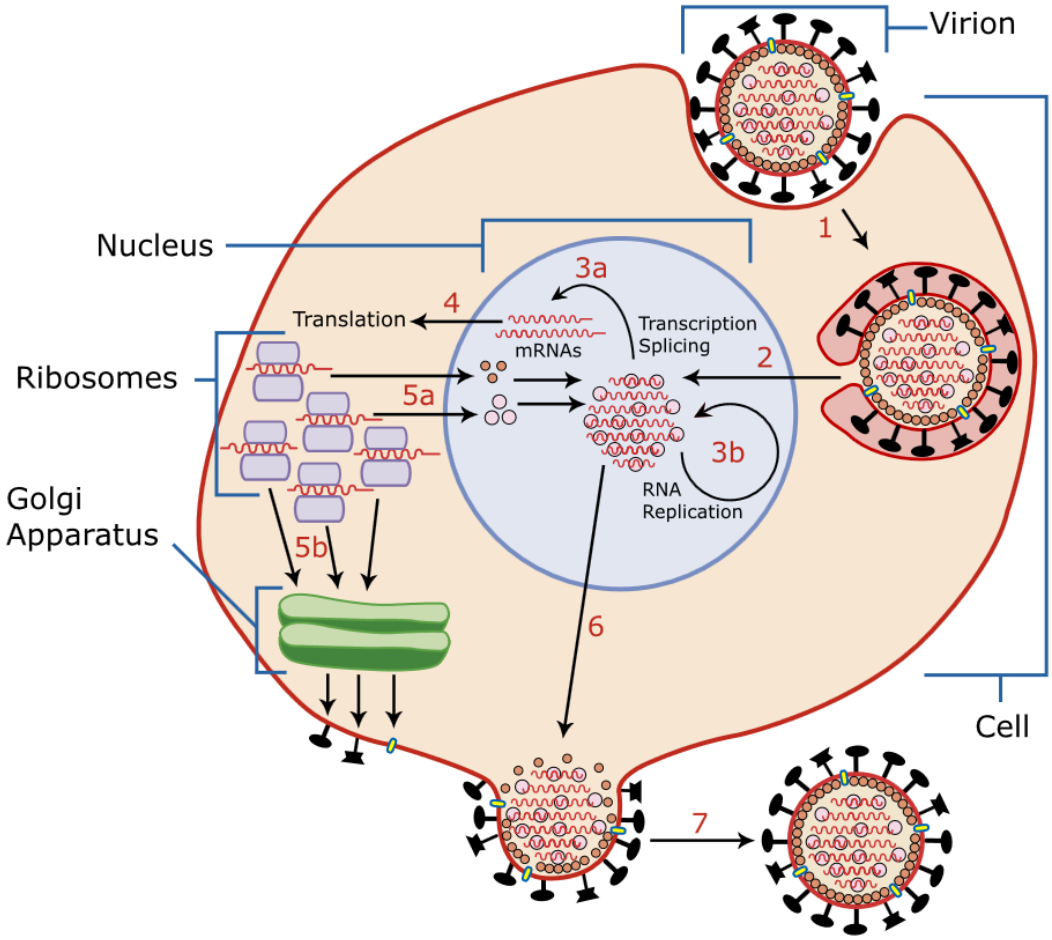

Figure 3 - Host invasion and replication cycle of an influenza virus. Step 1: Binding. Step 2: Entry. Step 3: Complex formation and transcription. Step 4: Translation. Step 5: Secretion. Step 6: Assembly. Step 7: Release. (© Boundless Learning, Inc under creative commons licence Sharealike 4.0)

The lifecycle of a typical enveloped virus can be divided into five stages. The first is the attachment of the virus to the outside of the host cell. This is usually mediated by viral proteins on the outside of the envelope or nucleocapsid binding to receptors on the plasma membrane surface. This binding is followed by the internalisation of the

virus. This can occur by direct penetration of the virus through the cell membrane, however for enveloped viruses the most common method is through direct fusion of the envelope with the plasma membrane or through endocytosis and release at the endosome.[4] Next the nucleocapsid is disassembled through degradation by viral or host proteases, or the capsid may spontaneously fall apart under a change in conditions such as changing pH. The virus is now free to replicate inside the host cell. The replication of a virus is different for all the different classes of viruses; however they all follow the same scheme. The DNA/RNA is replicated by polymerase enzymes and mRNA transcribed from them. This is then used by the host cell's ribosomes to produce viral proteins. The newly produced proteins and genetic material can then be assembled to form the progeny virions. This assembly is an extremely diverse process and will be looked at in more details for the specific viruses to be studies in this project. Finally the virus is released from the cell either through eventual lysis of the whole cell or through budding of the virus from the membrane. It is at this point an enveloped virus normally acquires its envelope.

1.3 Membranes and Lipid Domains

Lipids are one of the most fundamental building blocks of a cell. They consist of a wide range of hydrophobic or amphiphilic molecules, linked either by their biosynthetic pathways or by function. There are so many different species classed as lipid that classification of them all is still not universally agreed.[5] For biological systems, the most important lipids are considered to be the glycerol-phospholipids, along with certain sphingolipids and sterols. Phospholipids can be described as having a variable polar headgroup and two fatty acid tails. On their own, phospholipids will spontaneously form a variety of structures in water depending on their shapes. They arrange into structures that expose the polar headgroups to the water, while burying the hydrophobic fatty acid tails. The relative size differences between the headgroup and tails induce a curvature to any structures formed, the most important of which are detailed in figure 4. This will be important when looking at viral budding.

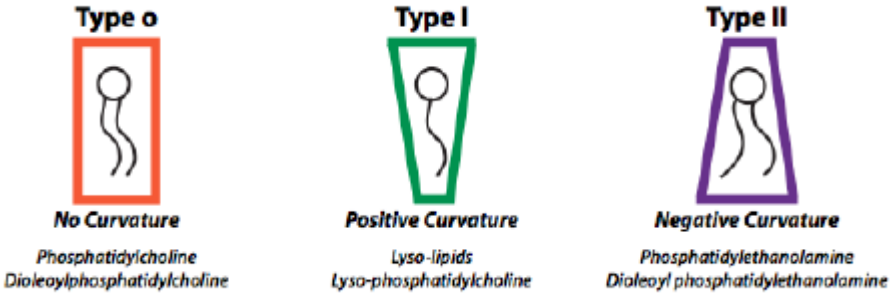

Figure 4 - The membrane curvature caused by different phospholipids, with examples. (© University of California, Davis under creative commons licence, from http://physwiki.ucdavis.edu)

The first model to be developed for biological membranes was the Singer-Nicolson model.[6] This model suggests that the membrane consists of a bilayer of freely diffusible phospholipids, studded with proteins. However this model only describes the gross morphology of membranes, since membranes consist of many different types of lipids showing different properties and a wide variety of proteins.

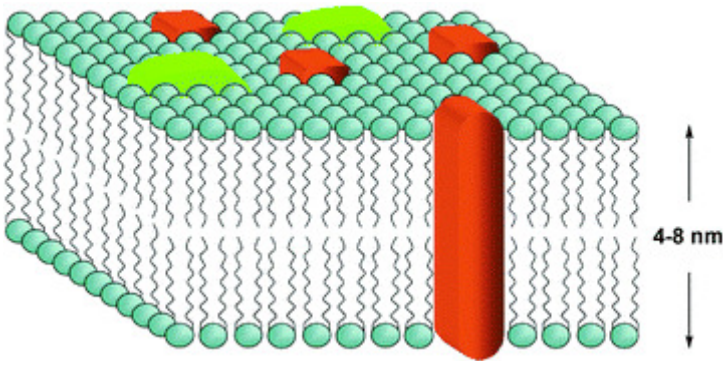

Figure 5 - The Singer-Nicholson model of biological membranes. The green and red molecules are embedded or transmembrane proteins.[7] (Reprinted with permission, Royal Society of Chemistry)

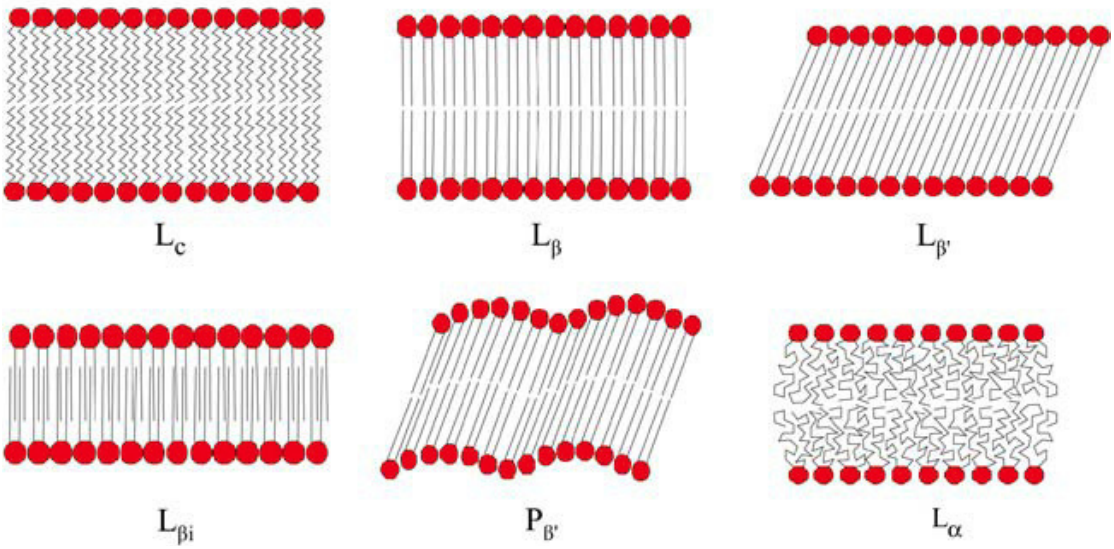

Figure 6 - Phases of DMPC bilayers[8] (Reprinted with permission, Elsevier)

Lipid bilayers exhibit lyotropic liquid crystalline properties. For example, figure 6 shows the properties of DMPC. At low temperatures (<15°C) the $L_{\beta'}$ phase is formed, followed by L_β and L_c over time. Above 15°C $P_{\beta'}$ is formed until above 24°C the L_α phase is formed. However, since biological membranes contain so many different lipid species, the phase behaviour of an actual membrane becomes much more complex and can vary greatly between membranes.

When observing artificial membranes, it has been observed that with certain combinations of lipids two domains can coexist. These have been termed the liquid ordered (L_o) and liquid disordered (L_d) phases. The L_o domains have been observed to be areas enriched in cholesterol and sphingolipids, and lack conformational and rotational freedom.[9] This is believed to be due to the intercalation of cholesterol between the fatty acid tails of the sphingolipids which prevents "kinks" forming in them and so greatly increases the temperature to form the L_α phase. The L_d phase is the surrounding disordered lipids which has full freedom on movement and conformation.

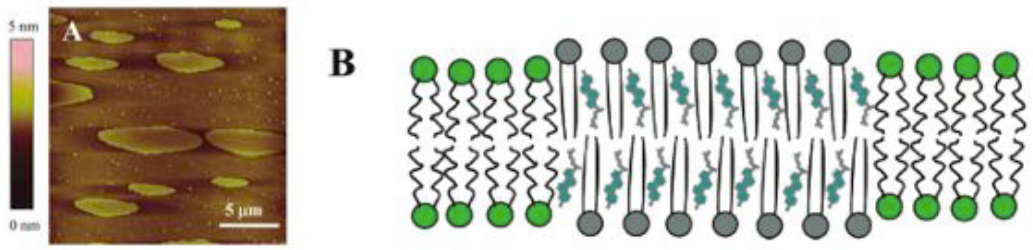

Figure 7 - A) AFM image of a DOPC/Cholesterol/SM membrane. B) Cartoon of L_o and L_d phases of a PC/SM/Chol lipid bilayer.[10] (Reprinted with permission, American Chemical Society)

Interpreting these observations *in vivo* has been more difficult. For most earlier work, L_o domains have been identified with detergent resistant membranes (DRMs). These are membrane fractions found to remain intact after addition of a detergent. Since these fractions contain large amounts of sphingomyelin and cholesterol, and form L_o-like structures, it was thought that these may be the L_o domains from the cell membrane.[11, 12] However while this has been useful experimentally it is contested by some that since using detergents alters the lipid profile of the extracted membrane and that different preparation of DRMs produces different membrane compositions, they cannot be directly identified as existing in this state *in vivo*.[13]

The result has been the "raft" hypothesis of biological membranes, so called because areas of L_o domains are thought to float in the "sea" of lipids in the same way as proteins do in the Singer-Nicolson model. These rafts are distinct transient microdomains, of a scale that makes them difficult to study directly, often showing different behaviour from model L_o/L_d systems.[14] These rafts are thought to exist on both envelopes of the membrane, although whether they must exist together is still unknown.[15] Most evidence for raft formation has come from studies showing that certain proteins and lipids cluster together, however this has only been shown for very small clusters, suggesting that rafts are of a much smaller size than artificial L_o domains or DRMs.[16] However, as new methods are developed we are getting closer to being able to see rafts and raft behaviour at the nano scale on the cell surface.[17]

Rafts domains have been implicated in a large number of processes, ranging from signal transduction[12] to membrane sorting and organising.[18] However, they have also been implicated in the assembly of enveloped viruses.[19] The theory of this is that

when an enveloped virus buds it needs to take viral glycoproteins with it in the envelope membrane, this process is much more efficient when the glycoproteins are clustered together and the uncoated progeny virus is directed towards them. This clustering is thought to take place in lipid rafts, and the matrix protein which surrounds the nucleocapsid interacts with these lipid rafts. This is supported by evidence in several viruses that viral glycoproteins co-localise with other raft markers, such as GM-1,[20, 21] that viral envelopes are enriched in cholesterol and sphingolipids,[22] and efficient viral assembly requires functional raft domains.[23]

1.4 Respiratory Syncytial Virus

1.4.1 The Virus and Disease

Respiratory Syncytial Virus is a member of the family *Paramyxoviridae* of the *Mononegavirales*. It is a class V, enveloped virus with a single stranded negative sense RNA genome. The virus is endemic and is the "single most important cause of severe LRIs in infants and young children"[24]. There are an estimated 64 million cases worldwide every year and 160,000 deaths resulting from respiratory problems. The virus infects the upper respiratory tract before progressing to the lower tract. Symptoms begin with wheezing and shortness of breath caused by the immune system damaging lung epithelial cells in an attempt to remove the infection. This can lead to complications of pneumonia, where fluid from damaged cells leaks into the bronchioles, causing a decrease in oxygen uptake and a risk of secondary infections.[25] The disease has been recognised as an increasing problem in the elderly, and the potential problems this will lead to as populations age.[26] Despite this, there is currently no vaccine or effective treatment beyond broad antiviral drugs. A humanised monoclonal antibody to the fusion (F) protein is available under the name palivizumab however this only provides short term immunity and so must be updated with several doses. The high cost of this treatment makes it unattractive to all but the richest countries.

hRSV consists of 11 proteins, encoded in 10 cistrons of a single stranded RNA genome.

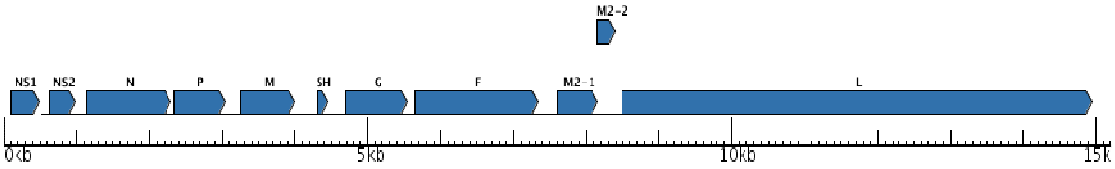

Figure 8 – Genome map of hRSV (©ViPR http://www.viprbrc.org)

The Nucleoprotein (N) encapsulates the RNA genome as a helical complex which protects the genome and serves as a scaffold for the proteins involved in replication to attach. [27, 28] The viral ribonucleoproteins complex (vRNP) consists of this nucleoprotein complex and attached Phosphoprotein (P), Large Polymerase (L), and two Matrix protein 2 isoforms (M2-1 and M2-2). The Phophoprotein acts to stabilise the large polymerase and to aid it correctly binding the N-RNA complex.[29] The L protein itself is responsible for all RNA activity, such are replication, methylation and polyadenylation.[30] M2-1 aids in transcription and processing of RNA through binding the other vRNP components, while M2-2 is less well known but may be involved in the regulation of RNA transcription and regulation. A pair of proteins expressed are called non-structural proteins 1 and 2 (NS1 And NS2). These proteins are very poorly characterised, however have been shown to inhibit apoptosis and limit the host cell's immune response through the interferon pathway.[31, 32]

The viral envelope consists of lipids derived from the host cell, and is studded with three transmembrane proteins. The Fusion Glycoprotein (F) is involved in the fusion of the viral envelope with the target cell upon infection and for cell to cell fusion and syncitium formation.[33] The Attachment Glycoprotein (G) mediates the attachment of the virion to the target cell during infection.[34] The SH (Small hydrophobic) protein is mostly unknown in function, but may be involved in inhibiting apoptosis.[35] Between the viral envelope and the vRNP core sits the Matrix protein (M). This is the main structural protein of the virus and it binds the two components together. As the focus of this project, it will be discussed further below.

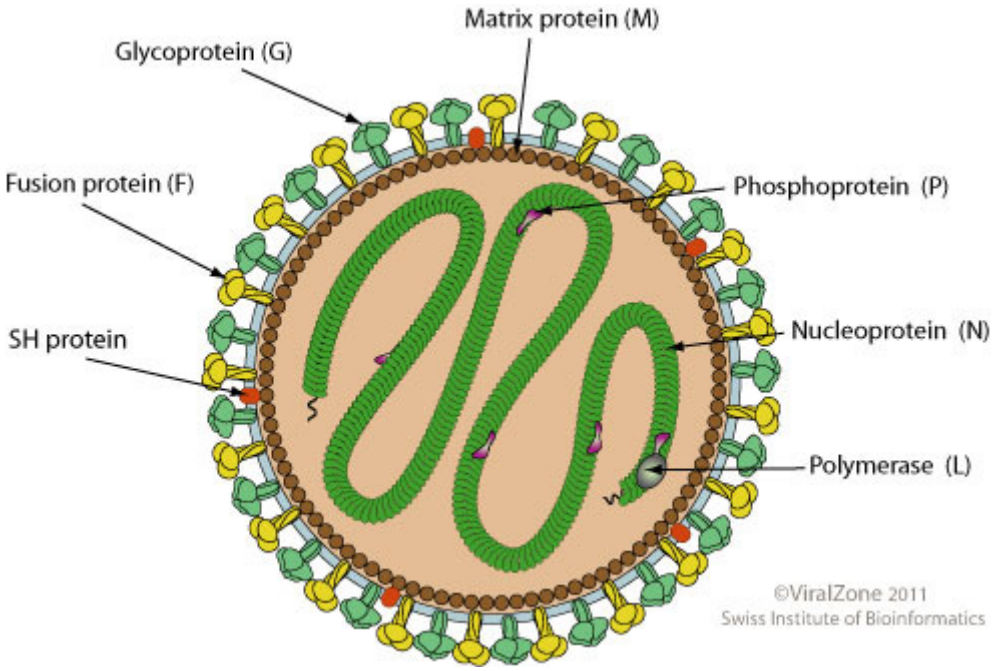

Figure 9 - Schematic of the structure of hRSV (©Swiss Institute of Bioinformatics, with permission)

While the virus replicates in the cytoplasm, assembly and budding of the virus occurs at the cell membrane.[36] In particular it is directed towards the apical membrane of lung epithelial cells, presumably to aid the further spread of the infection in the host.[37, 38] The virion can be spherical or filamentous, with filamentous being the predominant form.[37]

1.4.2 The Matrix Protein

Figure 10 - 3D crystal structure of hRSV-M (PDB = 2VQP). N-terminus is in blue, C-terminus in Red.[39]

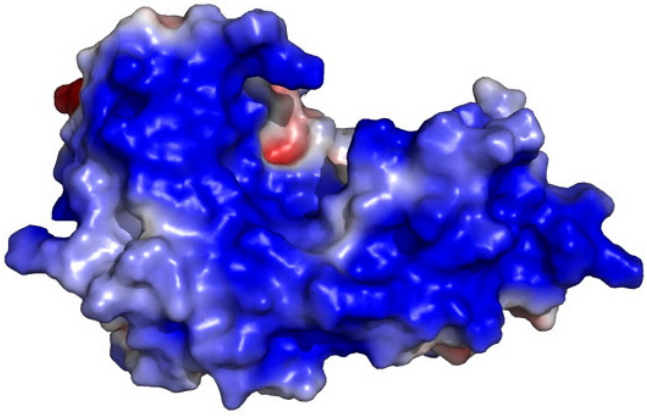

Figure 11 - Electrostatic surface potential (calculated with APBS) for hRSV-M, presented in a colour range from red to blue (−5 to +5 kT/e); uncharged residues are uncoloured.

The matrix protein (M) is an essential part of the virion, being implicated in virus assembly, budding, structural stability and some regulatory functions during the viruses lifecycle. M has two domains, N- and C- terminal, joined by a flexible linker region to give the full 256 amino acid protein. It has a large (600 $Å^2$) positively charged patch on its surface, across both domains, and also contains a large number of exposed tyrosines on the C-terminal.[39] Both of these may contribute to the M protein's ability to bind membranes,[40] with it hypothesised that the C terminal is most responsible for membrane binding, and the N terminal for protein-protein interactions.[41] By interacting with the host cell plasma membranes and the

nucleocapsid, the matrix protein holds the two together and facilitates the final assembly and budding of the virus.[42] M binds the envelope via interactions with F, G and with the membrane itself,[39, 43] and binds to the nucleocapsid via M2-1.[44] It has also been found that M is one of the few proteins needed to make virion-like particles (VLPs), while in other related viruses matrix proteins can form VLPs by themselves.[45, 46] This suggests that M may be very important in assembly of the virus into the correct shape.

Data collected by our group previously suggests that M is able to adsorb to the L_o phase surface of a DOPC / Sphingomyelin / Cholesterol monolayer.[47] In-vivo studies have also shown the M is co-purified with detergent resistant membranes, although whether this is dependent on viral glycoprotein presence is disputed.[48, 49]

M protein has also been shown to have other possible functions. Early on in viral infection the protein localises to the nucleus and may limit host RNA translation. [21] Late in the viruses life cycle M can be found in inclusion bodies, along with vRNPs, so it is suggested that M plays a role in the halting of transcription through an interaction with N.[21, 50]

1.5 Influenza A

1.5.1 The virus and disease

Influenza A is a virus of the family Orthomyxoviridae. It is a class V, enveloped virus with a single stranded negative sense RNA genome. The Influenza A virus is an extremely common infection, which infects an estimated 5-10% of the global adult population and 20-30% of children annually.[24] The disease is endemic in all populations, typically being most active during the winter months when closer living conditions aid its spread. Although the disease is usually mild, with symptoms including fever, sore throat and headaches, it is still a high risk disease among the very young, old and the immune compromised. There are an approximately 36,000 deaths each year attributed to influenza in the US alone each year, and a large economic cost associated with treatment and lost work hours. While the influenza

viruses are a family of their own, they share many similarities with other RNA viruses.[51] Along with their wide variety of hosts, this makes them a prime candidate for research.

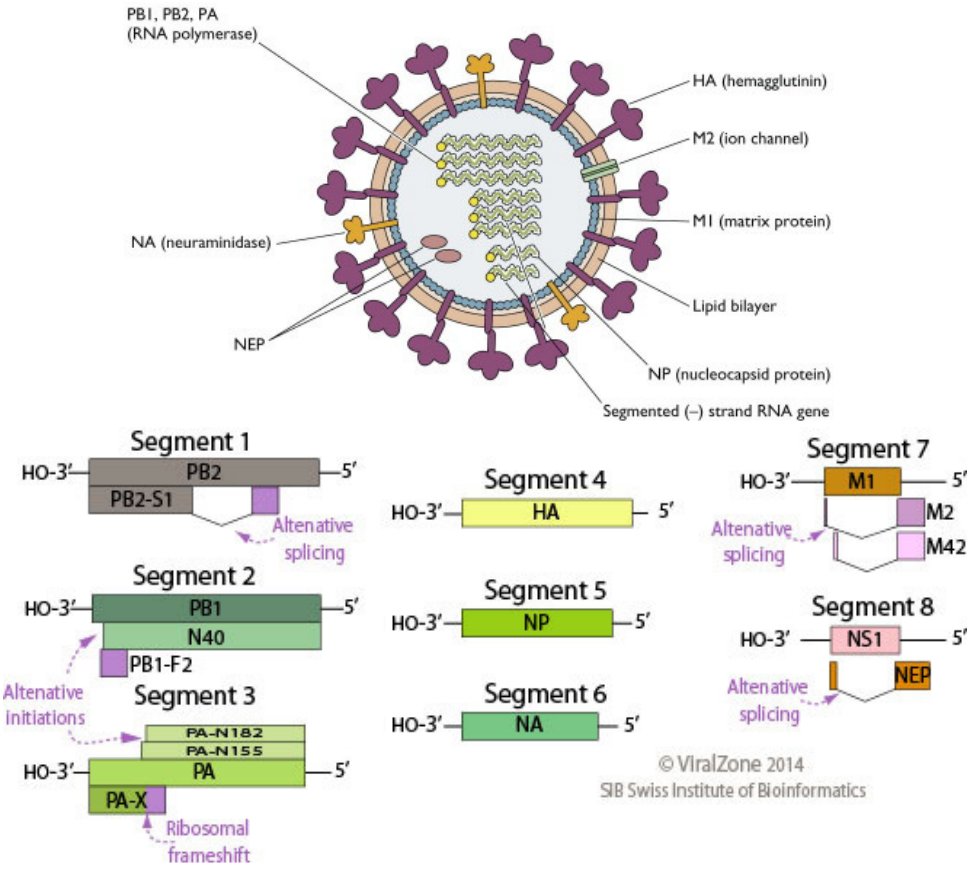

Figure 12 – Top: Structure of the Influenza virus A (© Dr Vincent Racaniello, http://www.virology.ws, under Creative Commons Attribution 3.0 License). Bottom the segmented genome of Influenza A. (©Swiss Institute of Bioinformatics, with permission)

The segmented genome of Influenza A encodes eleven different proteins. These make up the viral nucleocapsid and surrounding viral envelope. The nucleocapsid consists of the RNA polymerase enzymes PA, PB1, PB1-F2 and PB2. These are involved in the replication of the virus genome in the host cell.[52] The viral RNA is then packaged up with the NP (Nucleoprotein) protein in the nucleocapsid. These are supplemented in the nucleocapsid by the NS1 protein, which prevents the host cell's anti-viral response[53], and by the Nuclear Export protein (NEP), which exports the nucleocapsid complex from the nucleus once it is assembled.[54] The envelope of the virus consists of the phospholipid bilayer derived from the host cell membrane, which is then studded with viral proteins. The transmembrane proteins involved are arguably the most important ones in the virus attacking a cell and in its

recognition by the immune system. The ion channel M2 is involved in the equilibration of pH between the virus and host cell during viral maturation, and later in the acidification of the virus upon entry into a cell to release the nucleocapsid from the envelope.[55] The neuramidase (NA) and hemagglutinin (HA) proteins have large domains facing outward from the virus. These proteins assemble in lipid raft domains during viral maturation,[56] and on the luminal side interact with the matrix protein to attach the holonucleocapsid to the membrane.[57] The NA protein is involved in the maturation of the virus, by cleaving sialic acid residues from the surface of the assembled virus to aid its release from lung cells, while the HA protein binds to target cells during viral infection, leading to the entry of the virus. They are also currently the most important antigenic proteins of Influenza A, with Influenza infections being characterised by the subtypes of these proteins (N1-9, H1-17) and are how the body recognises the infection.[58] Due to this they form major targets for drug discovery. The final Influenza A protein is the matrix protein.

The Influenza A virion may form in two different shapes. Some strains, such as A/*Puerto Rico/8*/1934 H1N1, bud as spherical virions, while others, such as A/*Udorn*/1972 H3N2, bud into a filamentous form.[59] While this difference has been hypothesised to be due to difference in the structural proteins, it is also observed that most virions in a clinical setting are observed to be filamentous, and that differences may be less pronounced.[60, 61]

1.5.2 The Matrix Protein (M1)

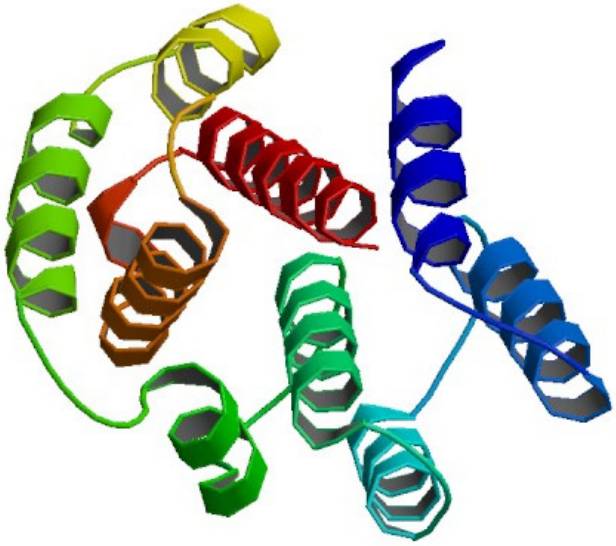

Figure 13 - 3D Structure of Influenza A Matrix Protein N-terminus[62]

The Matrix protein of Influenza A (M1) is a 28 KDa, 252 amino acid protein, and is the main structural protein in the virion. The protein has many similarities with other matrix proteins, and is believed to share a common ancestor with HIV MA and other negative sense RNA virus matrix proteins.[51] The protein is commonly divided into 2 domains, the N domain and C domain which are joined by a linking region, sometimes referred to as the M domain. The crystal structure for a N fragment of this protein has been solved (residues 2-158) which showed that it is mostly alpha helical in secondary structure.[63] The C terminal domain is believed to be weakly structured, and studies looking at which amino acid residues are solvent exposed show the linker region and most of the C domain to be exposed.[64] M1 also contains a zinc finer domain, and 15% of the M1 in purified viruses has zinc bound at this location.[65] While the direct action of this site is unknown, it has been mapped as important to vRNA binding.[66, 67]

M1 has been shown to have multiple functions in the life cycle of the virus. Interactions with components of the classical complement pathway have been shown, suggesting M1 has a role in protecting the virus from the host cell immune response.[68] M1 has also been found to contain a nuclear localisation sequence which allows it to be imported into the nucleus. There its first role in the assembly of the virus is the inhibition of transcription of viral RNA (vRNA). M1 is able to directly bind vRNA

and thus halt transcription, but it is also able to bind the viral ribonucelocapsid (vRNP) and halt transcription in favour of NP-RNA formation and formation of further vRNP.[69-71] Following this, M1 is involved in the export of vRNP from the nucleus. It achieves through binding of the vRNP and NEP to create a daisy-chain structure of Crm1/RanGTP-NEP-M1-vRNP, which is then targeted to the nucleopore complex for export.[54, 72-74] Once exported, M1 prevents the import of vRNPs back into the nucleus.[75] M1 will also interact with the actin cytoskeleton, possibly to aid transport away from the nucleus and towards the membrane.[76, 77]

As the major structural protein, M1 is heavily involved in assembly and budding of the virion. M1 has been shown to assemble at the plasma membrane by two distinct processes. The transmembrane proteins HA and NA interact with M1 through their cytoplasmic tails and have been shown to stimulate its recruitment to the membrane during the late stages of infection, resulting in co-localisation in vivo and co-purification with detergent resistant membranes.[78, 79] M1 also interacts with the cytoplasmic tail of M2, which has been shown to be required for virus formation.[80, 81] However M1 also binds to membranes without the presence of these proteins.[79, 82] In vivo M1 was found to associate stably with membranes, with both high salt conditions high pH and the mutation of surface hydrophobic residues unable to remove the association with membranes.[82] Electron microscopy has shown M1 bound to the periphery of the lipid envelope in mature viruses.[83] Studies on the N- and C- terminus of the protein have shown that only the N-terminus is in involved in membrane binding, and that it binds to negatively charged membranes.[70] The oligomerisation of M1 on the face of the plasma membrane also works to exclude host cell membrane proteins from the site and recruit other viral components for maturation.[52]

M1 bound to membranes is the major cause of viral budding for Influenza A. When M1 is limited viral particles are unable to bud from the membrane surface.[84] When M1 is expressed in cells it is able to bud from the membrane to form virus-like particles (VLPs), either with or without the presence of other viral particles, although the efficiency is reduced.[85, 86] Furthermore, M1 from different strains of Influenza A has the ability to dictate the form the virion takes during budding, with either filamentous or spherical forms of the virus depending wholly on the presence of M1, possibly through its interaction with the ribonucleoproteins.[60, 87, 88]

1.6 Other examples of viral matrix / core proteins

1.6.1 Ebola VP40

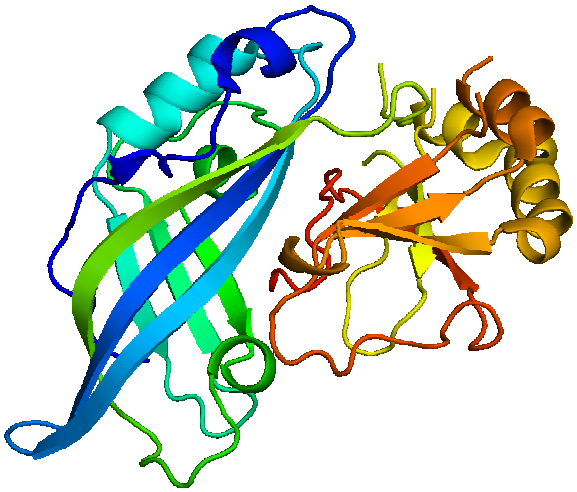

Figure 14 - X-ray crystal structure of Ebola VP40 (residues 44-326). PDB ID = 1ES6 [89]

Ebola VP40 is a matrix protein which has been shown to be involved in viral budding and morphogenesis. It consists of an N- and C- terminal domains, of which the C-terminal has been identified as required for membrane binding. Experiments have shown a preference for VP40 binding negatively charged lipid membranes, however only when in the monomeric state.[90] VP40 exists in different oligomeric states at different parts of its life cycle. The presence of octomers of VP40 has been shown to be required for viral replication and the regulation of transcription.[91, 92] It is still unclear how the virus coordinates the formation of these multimers throughout the lifecycle.[93]

1.6.2 Newcastle Disease Virus Matrix

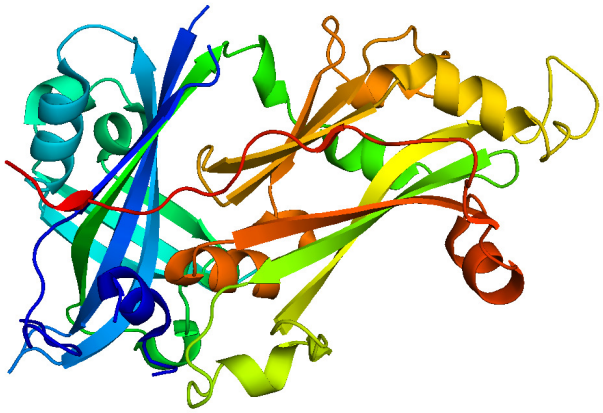

Figure 15 - X-ray crystal structure of NDV M. PDB ID = 4G1G

Newcastle disease virus (NDV) matrix protein (M) has been shown to have membrane binding, nucleocapsid binding and regulatory function during infection. Binding to membranes has been observed to occur with neutral, negative charged and positively charged lipids, suggesting a strong hydrophobic interaction is driving adsorption.[94] In vivo NDV-M protein alone is able to form VLPs, although this requires the integrity of lipid rafts in the cell to be possible.[95, 96] Interestingly, when NDV-M is able to spontaneously bud from a membrane in vitro to form coated liposomes, indicating that it can induce curvature on a membrane.[97] NDV-M also has a nuclear localisation sequence and interacts with the RNP, possibly to regulate transcription.[98, 99]

1.6.3 Hepatitis C Virus Core protein

HCV core protein is synthesised as a 22 kDa polypeptide that is inactive.[100] This polypeptide has been shown to need processing by the host enzymes signal peptidase (SP) and signal peptide peptidase (SPP) before mature virus can form.[101-103] This appears to allow the protein to fold correctly. Unlike matrix proteins, core protein itself forms the capsid, and is able to bind to RNA directly.[104] The lipid binding of the protein has been shown to be slightly different from matrix proteins as well. Core protein is mainly found localised to lipid droplets in hepatocyte cells, a property not seen in other *Flaviviridae*.[105, 106] The presence of core protein has a dramatic change on these lipid droplets, leading to an increase in amount, size and a change in cellular

localisation.[107-109] The loss of lipid droplets actually stops the production of the virus, suggesting that assembly occurs at this point.[110, 111] Detailed examination of these lipid droplets shows that virus budding and assembly actually occurs at ER membranes closely associated with the lipid droplet, however why lipid droplets must then be present is unknown.[112] The domains found to be essential for binding lipid droplets are believed to be unique among viruses, however may show some similarity with plant oleosin proteins.[113, 114] While the domains that may be involved in lipid binding have been identified, domains 1 and 2 particularly, there has been little work on the specifics of this interaction.[115, 116] Furthermore, recently it has been shown that core protein is palmitoylated, and is required for core to associate with the ER surrounding lipid droplets.[117] Expressed alone, the core protein has been shown to form VLPs, suggesting it is the major contributor to viral assembly and budding.[118] Other roles of the core protein have also been identified, such as up regulating genes involved in lipid accumulation and in downregulation of DNA repair.[118]

1.7 The scope of this research

The aim of this project is to study the structure and properties of hRSV-M and Inf-M1. With respect to hRSV-M, much of this work is a continuation of that done by Helen McPhee in previous years and published by our group, which although it has shed much light on the matrix protein has also left many more questions to be answered.[47] The interactions of M with artificial membranes have been probed, but there are still many combinations of lipids that have not been examined yet. Direct imaging of hRSV-M localising to these membrane systems has also not been achieved and the partitioning of M into different lipid domains has not yet been confirmed. There are also questions about possible changes in hRSV-M conformation upon membrane binding, and why mass spectrometry experiments have previously found an aberrant mass at +80 Da.

We also wish to carry this work on to the related matrix protein (M1) from Influenza A, to answer many of the same questions. The behaviour of this protein with membranes has been very poorly studied; with little know beyond an association with negatively charged lipids.

This project will utilise many different techniques in order to probe protein interactions with membranes, including thin film (Langmuir-Blodgett) techniques, Brewster angle microscopy and confocal microscopy. The structures of the proteins will also be investigated by circular-dichroism measurements, differential scanning fluorimetry, thermophoresis and dynamic light scattering.

2 Results - hRSV Matrix protein

2.1 Purification and Stability issues

1	*MGHHHHHHHHHHSSGHIEG(HMLE)*	METYVNKLHE	GSTYTAAVQY	NVLEKDDDPA	
31	SLTIWVPMFQ	SSMPADLLIK	ELANVNILVK	QISTPKGPSL	RVMINSRSAV
81	LAQMPSKFTI	CANVSLDDRS	KLAYDVTTPC	EIKACSLTCL	KSKNMLTTVK
131	DLTMKTLNPT	HDIIALCEFE	NIVTSKKVII	PTYLRSISVR	NKDLNTLENI
181	TTTEFKNAIT	NAKIIPYSGL	LLVITVTDNK	GAFKYIKPQS	QFIVDLGAYL
231	EKESIYYVTT	NWKHTATRFA	IKPRED		

Table 3 - The amino acid sequence for hRSV-M, including histidine tag. residues in brackets are retained after tag removal

hRSV Matrix protein was expressed as a recombinant protein from the plasmid vector pET16b-hRSV-M. This vector is designed to express the protein with an attached Hisidine tag and Factor Xa cleavage site at the N-terminus for purification. Expression and purification were carried out following previously established protocols[47]. In brief, the vector was transformed into the *E.Coli* strain BL21(DE3)pLysS and expressed after induction by the addition of IPTG to a final concentration of 1mM. The cells were harvested and the protein purified by a one step Immobilised Metal Affinity Chromatography purification. Fractions from the purification were analysed by SDS-PAGE and clean fractions were pooled (Figure 16) and the Histidine tag removed by Factor Xa cleavage. The protein finally dialysed into a PBS buffer.

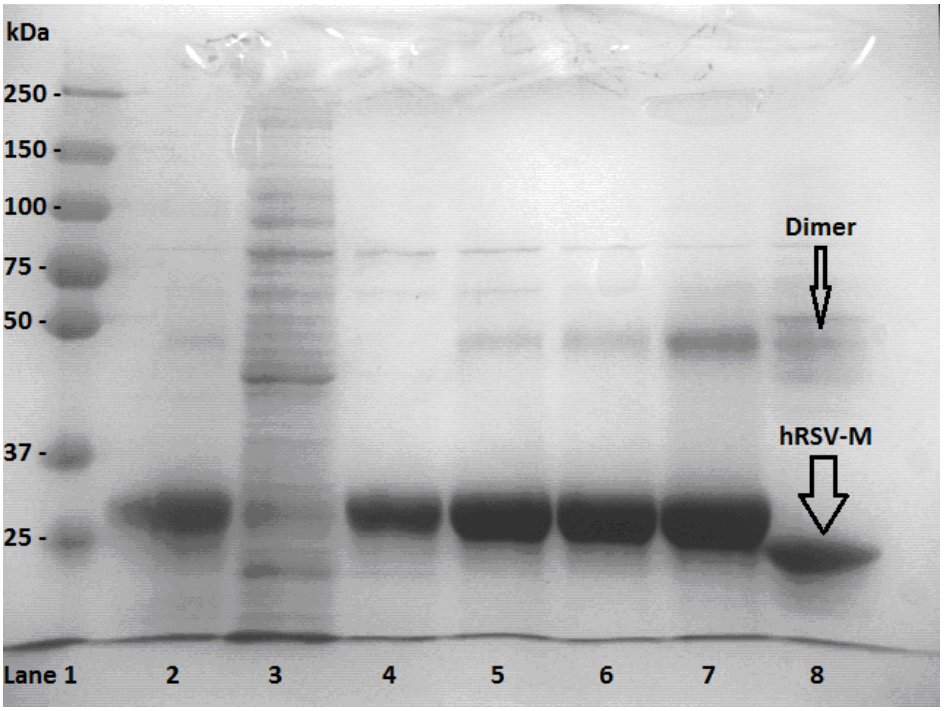

Figure 16 - Purification of hRSV-M. Lane 1- Protein ladder, lane 2- unpurified hRSV-M, lane 3- flow through from IMAC, lanes 4-7 Elutions from Ni-IMAC at 50-500 mM Imidazole, Lane 8- hRSV-M with 6xHis tag removed

While this protocol had been used in previous work to produce the protein, during this work the protein often presented stability problems. Following purification the protein would precipitate out of solution overnight, leaving very little material behind for performing experiments. This precipitation was observed occurring independent of storage conditions, although increasing temperatures made this worse as expected for many proteins.

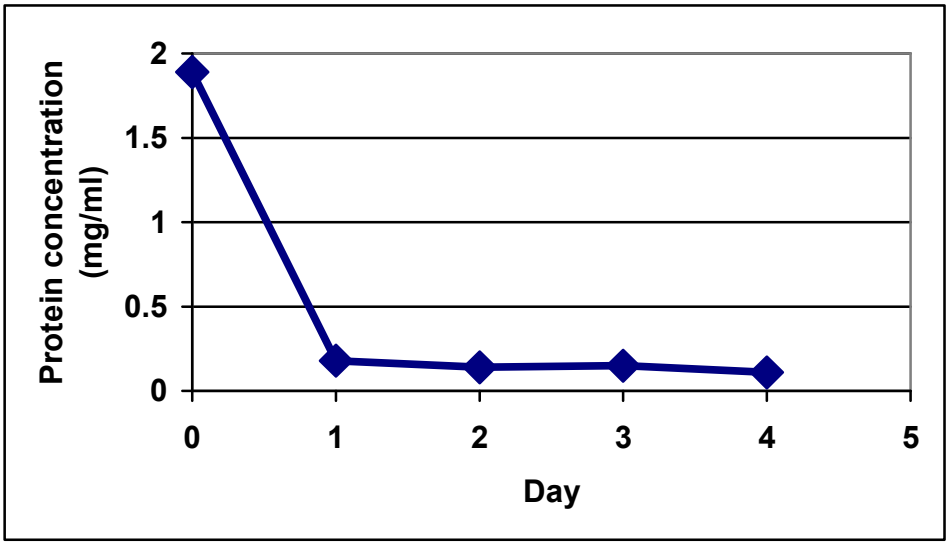

Figure 17 - Graph showing change in protein concentration of a purified sample of hRSV-M from day of purification (Day 0) to day 4

This change in behaviour of the protein was attributed to a change in the laboratory in which it was purified, and hence a change in some condition. When initial attempt to improve the stability failed, an approach was taken to identify and stabilising or destabilising elements involved in the purification.

2.2 Differential Scanning Fluorimetry

One method for exploring protein stability is to look for changes in the denaturation temperature of the protein, T_m. By looking at changes in the T_m of the protein upon exposure to different chemicals or ligands, we an determine those that have a positive or negative influence on stability and possibly also identify new specific ligands for the protein[119]. The method adopted for studying hRSV-M was differential scanning fluorimetry. Briefly, the protein is mixed with the ligand or chemical to be tested and the fluorescent dye Sypro Orange. The sample is then loaded into a qPCR machine and change in fluorescence is monitored as the temperature is slowly increased.

Sypro Orange fluoresces at 570nm on excitation however it is strongly quenched by surrounding water. It also shows strong nonspecific binding to hydrophobic surfaces[120]. This makes it an ideal indicator for exposed hydrophobic surfaces on a

protein. One characteristic of the majority of soluble proteins is that they present hydrophilic surfaces on their exterior and hydrophobic surfaces are buried on the interior, hence increasing the entropy of the system. This is one of the major driving forces behind protein folding.[121] However when a protein is denatured, by heating or chemicals means such as urea, these hydrophobic surfaces and amino acids become exposed as the protein's tertiary structure unfolds. Thus using the fluorescence of Sypro Orange as an indicator, we can follow the denaturation of a protein as it proceeds from folded to an unfolded state.

hRSV-M was first tested with the protein in its initial purification buffer, PBS, against a screen of 96 different chemicals from Hampton Research (Solubility & Stability Screen, HR2-072). This screen contains a range of conditions, focusing on different pH and buffer conditions (pH 3.5-9.6) and numerous small additives that have previously been identified as stabilising some proteins in experiments. While all these conditions were tested, only those showing significance are shown below. All T_m's were calculated by fitting the appropriate section of each data to a sigmoidal Boltzmann distribution and the point of inflection calculated.

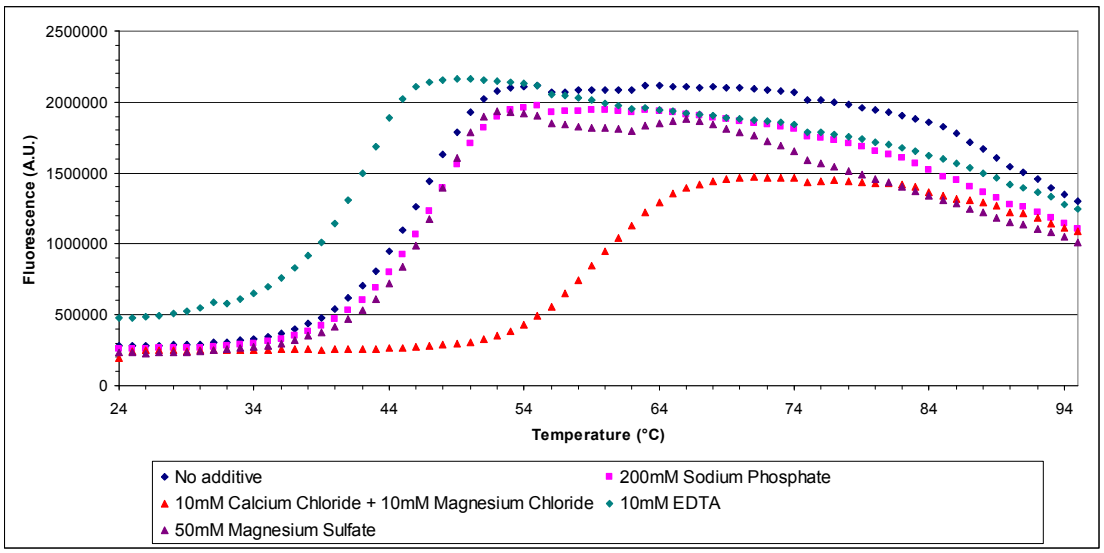

Figure 18 - DSF data for hRSV-M in PBS buffer with addition of chemicals

Additive	T_m (°C)	ΔT_m (°C)
None (PBS buffer)	47.0	-
200mM Phosphate buffer pH 7.4	47.5	0.5
10mM $CaCl_2$ and $MgCl_2$	58.8	11.8
10mM EDTA	43.0	-4.0
50mM $MgSO_4$	48.0	1.0

Table 4 - T_m values for hRSV-M with additives used in DSF experiments in phosphate based buffer

As can be seen in figure 18, the additives that showed the greatest change were all involved in metal binding. The addition of EDTA was shown to decrease the T_m of hRSV-M by 4°C, along with many denaturing chemicals such as urea (data not shown). EDTA is a strong chelator of many metals, and so it is reasonable to assume this reduction in stability is due to metals being removed from coordination with the protein. The strongest additive which showed an increase in protein stability was a mixture of calcium ions and magnesium ions, which together gave an increase in T_m of 11.8°C. Comparing this with the comparatively small change when only magnesium ions were added in higher concentration, this suggests that calcium is having a stabilising role.

However, this experiment was performed with the protein in a PBS buffer, as has been used previously for experiments on this protein in our group. The sample with 200mM phosphate ions added shows that while additional phosphate itself has no effect directly on the protein, it is well known that both magnesium and calcium form insoluble precipitates with phosphate ions. It is therefore possible that phosphate ions are having a negative effect on stability through the removal of these ions from solution. To test this, the experiment was repeated except the hRSV-M being purified in a Tris based buffer (50mM Tris, 200mM NaCl), and tested separately against the adding of phosphate ions, calcium ions and magnesium ions.

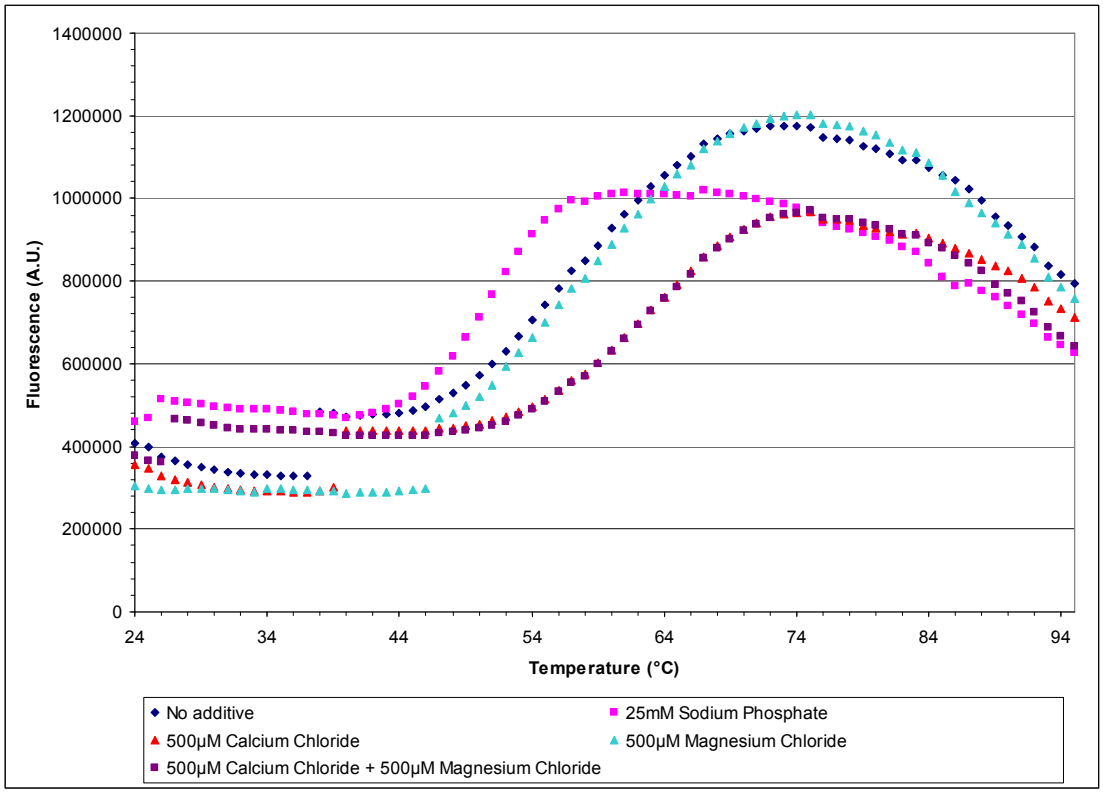

Figure 19 - DSF data for hRSV-M in Tris-based buffer

It should be noted that the discontinuity in the data for some of the additives was due to a mechanical error, and data points below 47°c were not used in their fittings

Additive	**T_m (°C)**	**ΔT_m (°C)**
None (PBS buffer)	57.2	-
25mM Sodium Phosphate	50.4	-6.8
500µM $CaCl_2$	62.5	5.3
500µM $MgCl_2$	57.6	0.4
500µM $CaCl_2$ and 500µM $MgCl_2$	62.6	5.4

Table 5 - T_m values for hRSV-M with additives used in DSF experiments in Tris-Hcl based buffer

As can be seen in figure 19, with phosphate removed from the buffering conditions, the stability of the protein is immediately improved, increasing the T_m by 6.8°C. Furthermore, by studying the addition of calcium and magnesium ions separately it can be seen that only calcium ions have an effect on the stability of hRSV-M. The addition of magnesium ions has no further effect than the addition of calcium ions alone. This gives the possibility that when added to hRSV-M in a PBS buffer, the magnesium ions were acting to remove some of the phosphate from the solution by precipitation, and so was having a synergistic effect with the calcium ions. While the calcium ions are now shown to have a smaller effect on the T_m of 5.4°C, the effect is

still significant and so onwards from this experiment hRSV-M was always purified in buffers without phosphate and containing 10mM $CaCl_2$, before dialysis into appropriate buffers for experiments.

However, this result was entirely unexpected and so further experiments were planned to see what the nature of this interaction with calcium is.

2.3 Inductively coupled plasma mass spectrometry

The technique of inductively coupled plasma mass spectrometry (ICPMS) is used to detect the presence of metal ions in a solution. For proteins, this allows for the protein directly examined to see what metals ions are found associated with it. This technique is sensitive enough to accurately determine the number of metal atoms in the sample and hence work out the stoichiometry of the metal binding to the protein.

For this experiment, hRSV-M was first incubated with 100mM $CaCl_2$ and 100mM $MgCl_2$, and then buffered exchanged into a metal free buffer (10mM MOPS PH 7.4) using a PD-10 desalting column (GE Healthcare). The protein concentration was measured in each 0.5ml fraction from the column, and then 300 µl of each sample added to 2.4 ml 100% Nitric Acid and 300µl water. The samples were then analysed by ICPMS along with references solutions containing calcium and magnesium ions of known concentration. The results shown below are an average of 3 separate readings.

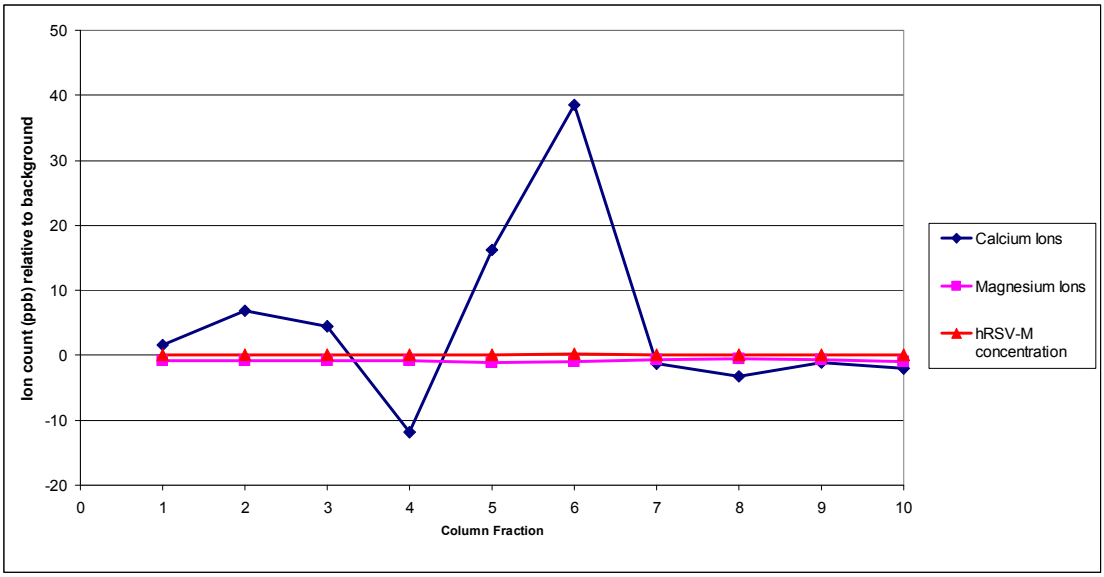

Figure 20- ICPMS data for calcium ions detected in fractions from PD-10 column after applying hRSV-M, and protein concentration for those fractions

Fraction No.	Protein concentration mg/ml	Protein Concentration µM	Calcium concentration (ppm)	Calcium concentration µM	Occupancy of calcium : hRSV-M
5	0.097	3.39	0.161	2.958	0.87
6	0.192	6.65	0.385	7.558	1.14
			Average occupancy		1.00

Table 6 - Results from ICPMS experiments on hRSV-M

The data shows that the stoichiometry of hRSV-M binding to calcium is 1:1 under these conditions, and that magnesium does not bind in any measurable amount. This result does not match x-ray crystallography data which showed no metals bound to hRSV-M.[39] However, this may indicate that binding is quite weak. In this experiment the protein was incubated with a high concentration of calcium just prior to the measurements, while the previous x-ray crystallography experiments were carried out with protein that had been purified in a way to that would have removed any calcium present.

2.4 Microscale Thermophoresis

Experiments in this section were carried out with the kind expertise of Dr Stefan Duhr from NanoTemper Technologies, and with the temporary loan of their equipment.

In order to examine the nature of calcium ions binding to hRSV-M, microscale thermophoresis was utilised. Thermophoresis is the effect seen when a temperature gradient is applied to particles in a gas or liquid mixture. Since the properties of the particle change how it behaves in response to the temperature gradient, whether they move towards the heated area or away from it, this method can be used to probe the association or dissociation of particles. [122]

The motility of any biomolecule in a temperature gradient in aqueous medium is governed by its hydration shell. In the case of proteins many factors can change the hydration shell, including protein structure, amino acid modification and small molecule binding. Since changes in motility are measured across a sampling of molecules, by measuring the changes over sequential conditions the effect of the changes can be quantified. In the case of molecules binding to the protein, this means that the K_D can be calculated from a serial dilution of the molecule applied to the protein.[123, 124]

To perform Microscale Thermophoresis, the protein is first labelled with a fluorescent marker, to allow its movement to be tracked. hRSV-M was labelled with the dye NT-647, a red fluorescent dye that modifies primary amines via a NHS-ester group. The sample is then mixed with a serial dilution of the additive molecule, in this case a range of calcium chloride solutions from 10 μM to 0.1 nM, and taken up into 4 μl capillary tubes to be loaded into the microscale thermophoresis apparatus (NanoTemper Monolith NT.115 Series). The process of taking a measurement for thermophoresis is detailed in figure 21. In brief, an infrared laser is directed at the capillary tube and after base-line fluorescence measurement is taken, the laser is switched on. This creates a localised heat spot generating the temperature gradient. The sample undergoes an initial temperature jump during which molecules rapidly move while the gradient is set up over the small area, resulting in a large drop in the fluorescence. This is then followed by the thermophoresis stage, which occurs over a 10-30 second time period and is the state in which the molecules are diffusing along the temperature gradient. Once the molecules have reached a steady state, the fluorescence difference between this state and the state before the infrared laser was switched on can be used to calculate the change in molecule concentration in the

heated spot. By taking these readings over a range of binding partner concentrations, the K_D can be determined by fitting to the equations detailed below.

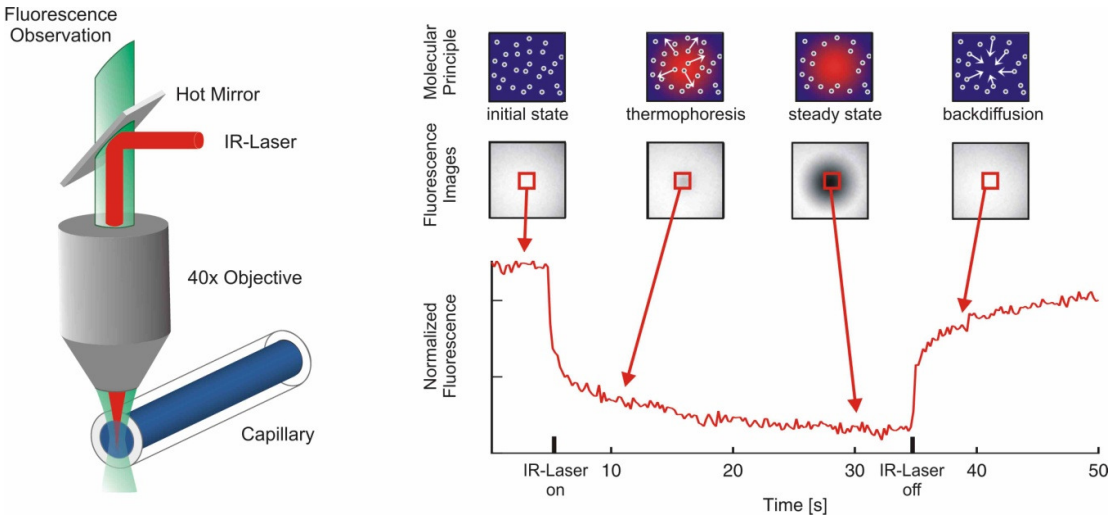

Figure 21 - A typical microscale thermophoresis measurement, showing the different stages and molecular movements. ©NanoTemper Technologies GmbH

Thermophoresis can be described by the difference between the concentration of molecules in the heated area and the concentration in the cold area, and how this change is brought about by a change in the diffusion coefficient as described by the following equation.[124]

$$\frac{c_{hot}}{c_{cold}} = \exp(-S_T \Delta T)$$

Equation 1

Where C_{hot} is the concentration in the hot area, C_{cold} is the concentration in the cold area, ΔT is the change in temperature between the two areas and S_T is the Soret coefficient, which is defined in equation 2 as the ratio of the diffusion coefficient (D) and the thermal diffusion coefficient (D_T).

$$S_T = \frac{D}{D_T}$$

Equation 2

Since the temperature and concentration changes involved in microscale thermophoresis experiments are small, equation 1 can be approximated to equation 3.

$$\frac{c_{hot}}{c_{cold}} = 1 - S_T \Delta T$$

Equation 3

The thermophoresis experiments are used to yield a normalised fluorescence value F_{norm}, as the ratio of the fluorescence change between the cold and hot states, and so can be fitted into equation 3 to give equation 4, where δF/δT is the change in fluorescence of the fluorophore with temperature.

$$F_{norm} = 1 + (\frac{\delta F}{\delta T} - S_T)\Delta T$$

Equation 4

Since F_{norm} is in linear relationship with the fraction of binding partner bound to the protein, the fraction bound (FB) is described by equation 5.

$$F_{norm} = (1 - FB)F_{norm \cdot unbound} + (FB)F_{norm \cdot bound}$$

Equation 5

If it is assumed that the law of mass binding action applies to this situation, with simple binding partners A and B, then the K_D can be expressed as equation 6.

$$K_D = \frac{[A]_{free}[B]_{free}}{[AB]} = \frac{([A]-[AB])([B]-[AB])}{[AB]}$$

Equation 6

By taking the fraction bound FB from equation 5 as the fraction of B in equation 6; and solving the combined equation for B, equation 7 is derived.

$$FB = \frac{[AB]}{[B]}$$
$$= \frac{[A]+[B]+K_D - \sqrt{([A]+[B]+K_D)^2 - 4[AB]}}{2[B]}$$

Equation 7

Using the relationships in equations 5 and equation 7, it is hence possible to calculate the K_D for a small molecule binding a protein by measuring the change in fluorescence during thermophoresis. By plotting a graph of F_{norm} against binding partner concentration, the resulting data points can be fit to equation 7.[123] This process applied to the following data.

Samples of hRSV-M were tested with varying concentrations of calcium chloride and produced the following results.

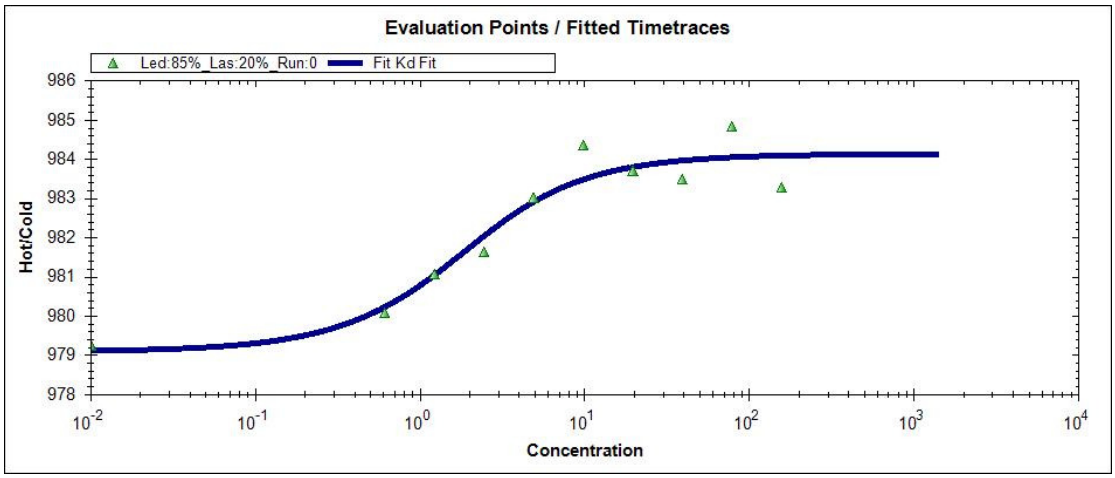

Figure 22 - Microscale Thermophoresis results for "higher" affinity binding. Y-axis shows fluorescence (A.U), X-axis shows concentration of Calcium Chloride (µM)

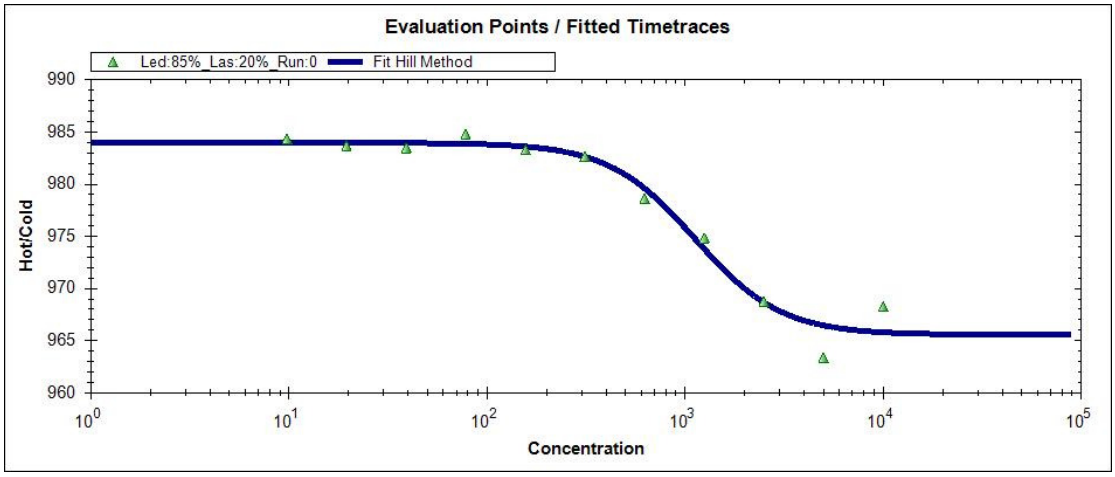

Figure 23 - Microscale Thermophoresis results for "lower" affinity binding. Y-axis shows fluorescence (A.U), X-axis shows concentration of Calcium Chloride (µM)

The microscale thermophoresis experiment showed two separate binding events for hRSV-M and calcium. The first was a "higher" affinity binding event, which resulted in a reduction in motility of HRSV-M with the addition of calcium, giving a calculated K_D of 1.95×10^{-6} M. The second was a significantly weaker binding event, giving an increased motility of HRSV-M down the temperature gradient formed, with a calculated K_D of 1mM. A typical concentration of free calcium within lung cells is 50-250 nM, while that in the extracellular fluid is much greater, approximately 1-2.5 mM.[125] While these values suggest that while inside a cell hRSV-M would not have calcium bound, the levels of calcium in a cell can vary greatly by compartment, with endoplasmic reticulum levels reaching several hundred µM. Furthermore, the infection of cells by a virus has been shown to increase the levels of calcium inside a cell further.[126, 127] In hRSV the SH protein has been found to act as a cation-selective channel, and would likely lead to a large increase in internal free calcium as it leaks in from the extracellular fluid.[128] This suggests that the two calcium binding sites correspond to different functions and will have different occupancies depending on the stage in the virus's lifecycle. The high affinity binding site would likely be filled first while inside the cell when the intracellular calcium concentration is raised by the virus. This may be a signal for virus maturation or budding. The lower affinity binding site would not be occupied at intracellular calcium concentrations, but may become filled once the virus has budded into the extracellular fluid, possibly to increase the stability of the virus as shown by the DSF data.[126]

2.5 Circular Dichroism Spectroscopy

In order to explore if the addition of calcium to hRSV-M has any significant change on the protein's structure, it was subjected to circular dichroism spectroscopy. CD spectroscopy is a variant of UV-Vis spectroscopy, which relies on the use of circularly polarised light and its differing interactions with certain molecules. In the case of proteins, circular dichroism spectroscopy in the far UV range can be used to probe the secondary structure of a protein, but not tertiary or quaternary structure.[129]

Light can be polarised into left-handed and right-handed polarised light. Each of these can interact with a medium in different ways. For circular dichroism spectroscopy, the change in absorbance of circularly polarised light per molecule is tested, giving equation 8 (where *c* is the concentration and *l* is the path length). For proteins, light is used in the far UV range (~180-260nm) since this covers the absorption band corresponding to amino acids. As a major constituent, it is mainly the n→π* (220nm) and π→π*(190nm) transitions of electrons in the amide bonds of the amino acids that absorb the circularly polarised light. As these bonds make up the backbone of the protein's structure, the energy of these transitions is influenced by the geometry of the backbone, and hence the secondary structure of the protein. Changes in the structure of the protein backbone can therefore be detected and interpreted.[130]

$$\Delta\varepsilon = \frac{(A_L - A_R)}{c \times l}$$

Equation 8

A circular dichroism measurement will report the different absorbance of polarised light in millidegrees, and this can be converted into mean residue ellipticity for analysis by equation 9. Mean residue ellipticity is used for proteins to give normalised values that can be compared between proteins of different sequences.

$$[\theta]_{mrw} = \frac{0.1 \times \theta_{obs}}{n \times c \times l}$$

Equation 9

Following a measurement, circular dichroism data can be analysed by comparing the obtained spectra with the spectra of other proteins of known 3D structure as determined by x-ray crystallography, and therefore making an estimate of secondary structural characteristics. For the following data, three different algorithms were used initially to analyse the data, Selcon3, Continll and CDSSTR. However, of these three only Continll provided a close fit to the data, and so is the only one shown here. The Continll algorithm relies on the assumption that different spectra assigned to different structural features can be linearly added together to calculate a fit for the experimental data. The algorithm takes a reference set of proteins with known secondary structure and spectra and compares them to the experimental data. If the match is considered good then that spectra is given a higher fraction of contribution to the final fit. Where Continll differs from other algorithms is that reference spectra with a poor fit are systematically deleted from the fitting as each iteration is carried out.

The following experiments were carried out on hRSV-M, either in a weak buffer alone (1mM Tris-HCl) or with the addition of 1mM $CaCl_2$. Spectra were recorded using a cuvette with pathlength 0.2cm and a range of collection of 180-240nm. The high tension voltage was monitored during the experiment, and any results obtained after the voltage went above 600V were disregarded as the noise in the data became too high.[129] For analysis the spectra had a background reading subtracted and the values converted into mean residue ellipticity. For the fitting algorithms, reference protein set 10 was used (SMP56). This set contains 56 proteins of which 13 are membrane proteins. The large number of reference proteins helped to find a good fitting compared with smaller sets, and the addition of membrane proteins was used previously to help fit hRSV-M, likely because as a membrane binding protein it behaves in much the same way.[39]

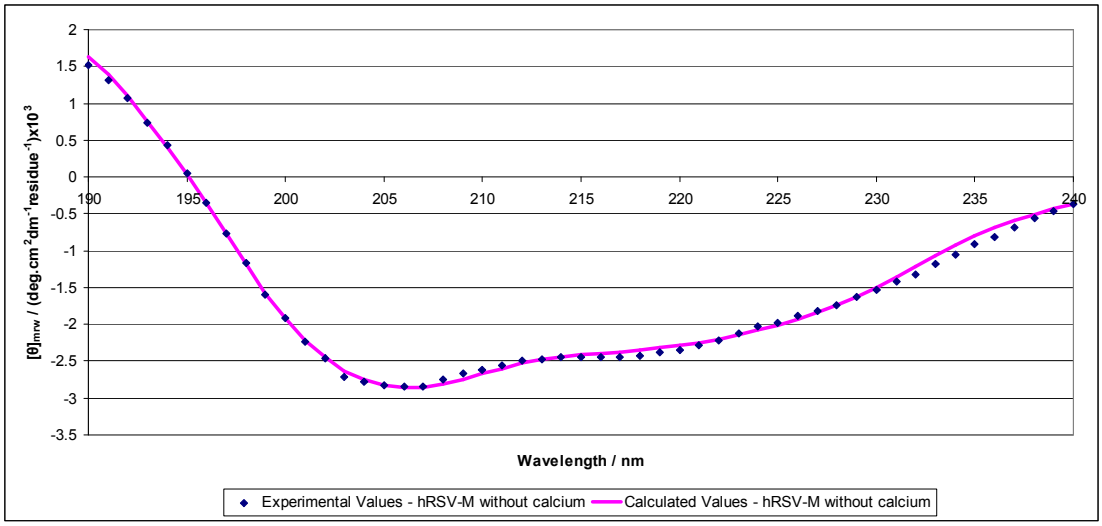

Figure 24 - Circular dichroism spectra of hRSV-M in 1mM Tris-HCl, showing experimental values and spectra calculated with Continll

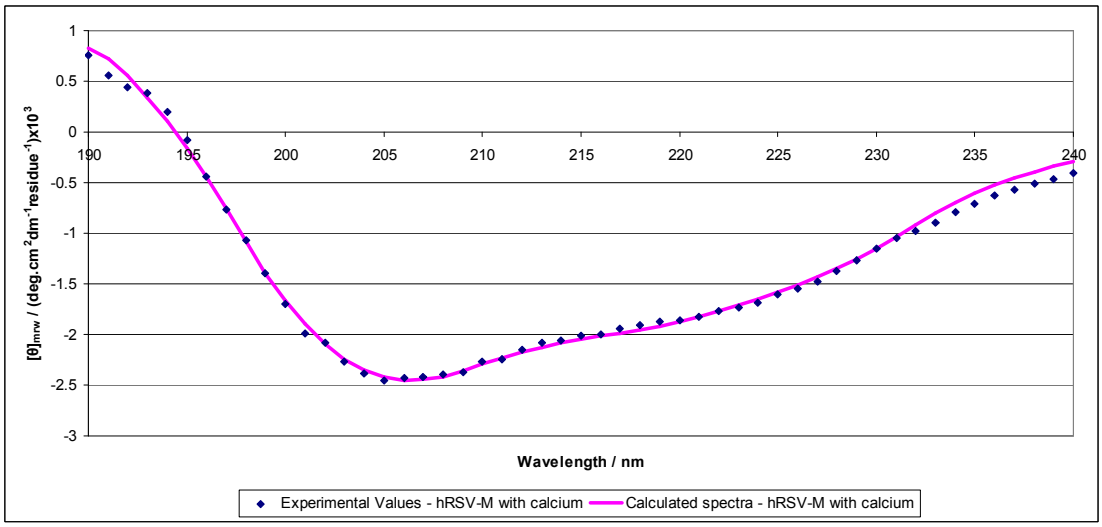

Figure 25 - Circular dichroism spectra of hRSV-M in 1mM Tris-HCl and 1mM $CaCl_2$, showing experimental values and spectra calculated with Continll

	Structural Feature (%)					
	α-Helix (regular)	**α-Helix (distorted)**	**β-Sheet (regular)**	**β-Sheet (distorted)**	**Turn**	**Irregular**
hRSV-M without calcium	8.3	10.1	15.0	10.0	23.4	33.2
hRSV-M with 1 mM calcium	7.5	9.8	15.8	10.5	22.9	33.4

Table 7 – Secondary structural features of hRSV-M with and without calcium, calculated by Contin ll algorithm.

The above results show that hRSV-M did not exhibit any significant change in secondary structure upon calcium binding. It can therefore be expected that calcium binding does not cause a great change in the protein's 3D structure. Furthermore, the spectra obtained here gave the same secondary structure prediction as previous identified for hRSV-M in a phosphate based buffer.[39] This indicates that the change in buffer conditions was also not changing the protein's structure.

2.6 Mass Spectrometry

During experiments, samples of hRSV-M were regularly subjected to mass spectrometry analysis to check the purity of the samples. Since hRSV-M was first purified in our group, all mass spectra have shown the expected 29351 Da mass peak for the native hRSV-M, however it has also always shown a peak at +80 Da at 29431 Da. While the identity of this extra mass has previously been theorised as either a bound metal or modification of an amino acid, it was never confirmed.

During the experiments details in section 2.10, attempts were made to label hRSV-M with a fluorescent molecule to aid visualisation under microscope. While the final decision was made to use FITC, due to a stronger fluorescence, initially experiments were taken to label hRSV-M using 4-chloro-7-nitrobenzofurazan (NBD-Cl). This is a

reactive species, known to react with amino and thiol groups.[131] On a protein this results in labelling on lysine and cysteine groups. When this procedure was carried out on hRSV-M, the results showed some interesting features, as detailed below.

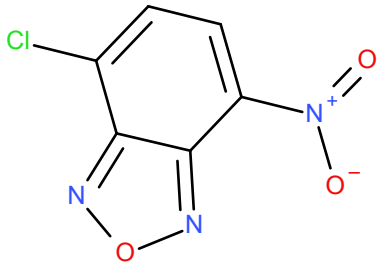

Figure 26 - Structure of 4-chloro-7-nitrobenzofurazan (NBD-Cl)

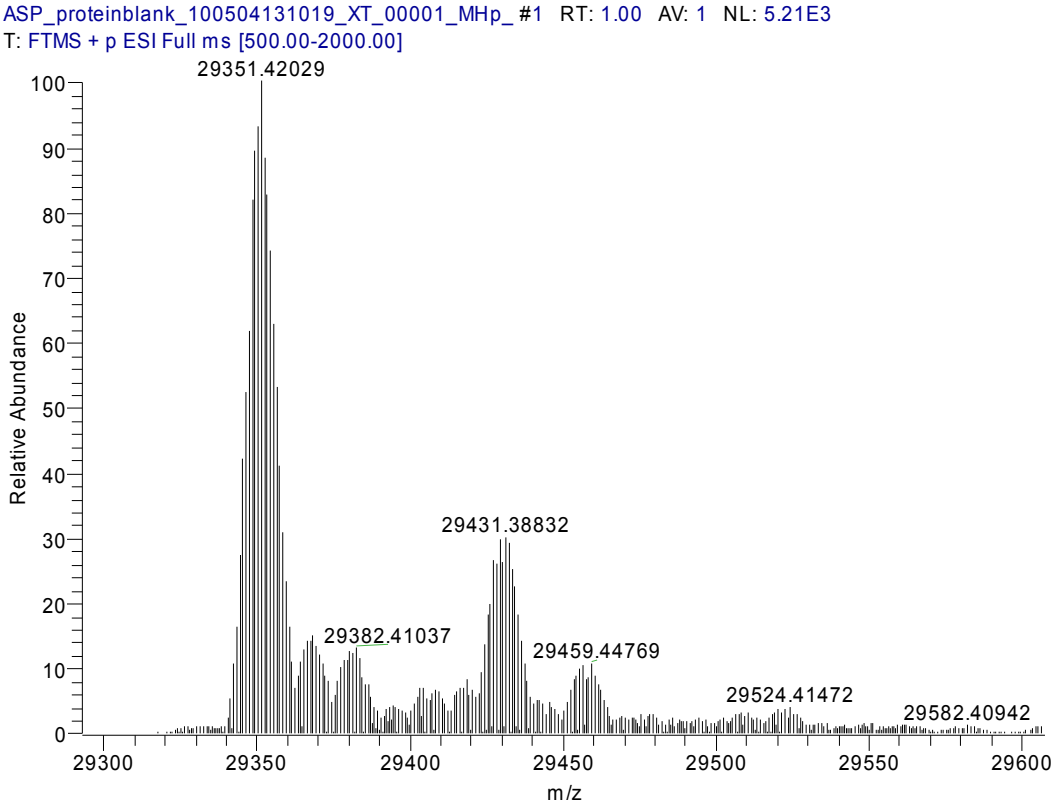

Figure 27 - Mass spectrum of native hRSV-M

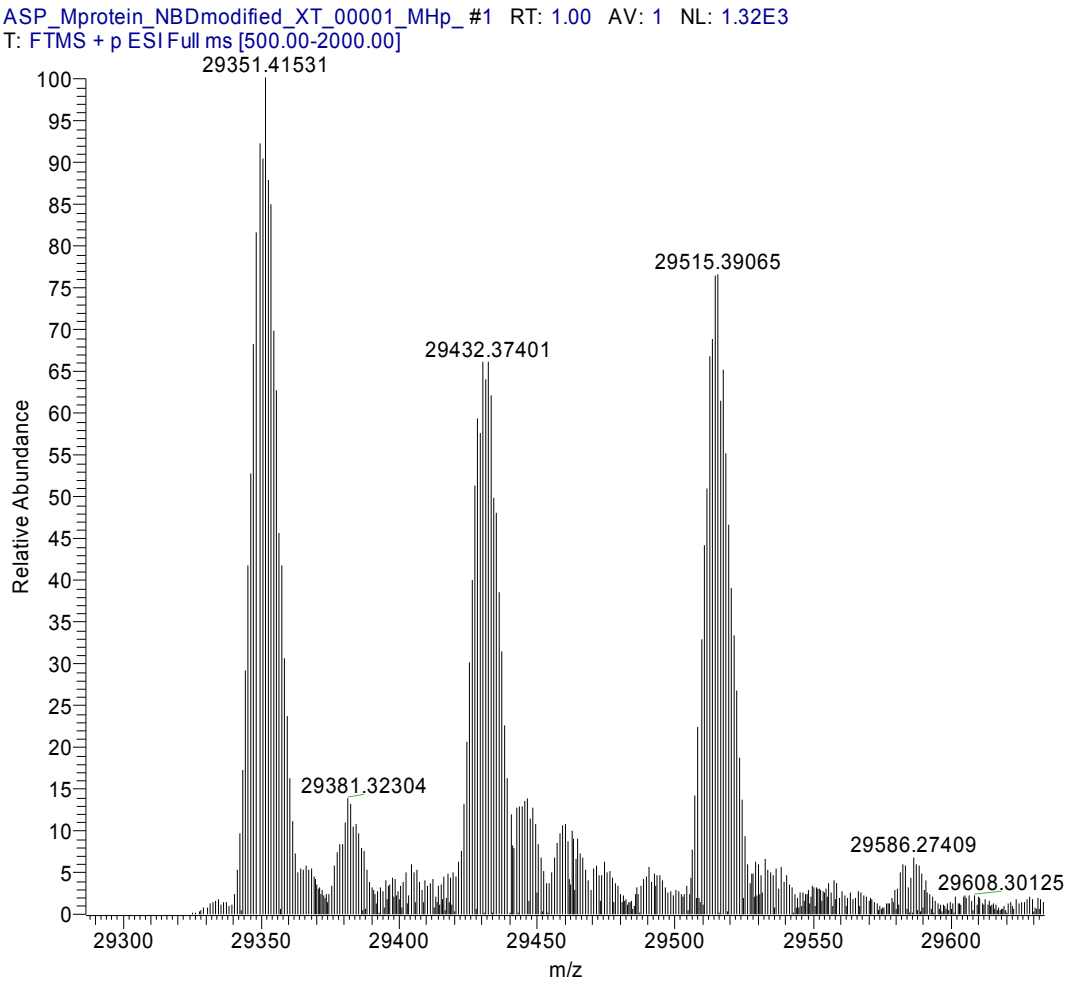

Figure 28 - Mass spectrum of modified hRSV-M-NBD

The mass spectrometry showed that NBD-Cl labelling had occurred on only one residue per protein molecule, with an additional peak at 29515 Da being present in figure 28 and absent in figure 27 corresponding to the addition of the NBD moeity, and so tryptic digest mass spectrometry was performed on the proteins by Dr Aruna Prakash of the mass spectrometry service at Durham. This involves the digestion of the protein into smaller peptides by using the peptidase trypsin, and then analysing the individual fragments to identify which have been modified. Only one fragment was identified as modified and is highlighted below, though the signals were weak so more may exist.

```
1   METYVNKLHE GSTYTAAVQY NVLEKDDDPA SLTIWVPMFQ SSMPADLLIK ELANVNILVK
61  QISTPKGPSL RVMINSRSAV LAQMPSKFTI CANVSLDDRS KLAYDVTTPC EIKACSLTCL
121 KSKNMLTTVK DLTMKTLNPT HDIIALCEFE NIVTSKKVII PTYLRSISVR NKDLNTLENI
181 TTTEFKNAIT NAKIIPYSGL LLVITVTDNK GAFKYIKPQS QFIVDLGAYL EKESIYYVTT
```

241 NWKHTATRFA IKPRED

Figure 29 - Amino acid sequence of hRSV-M, with NBD modified peptide highlighted

Since the modified fragment contains only one lysine and one cysteine, the modification must have occurred on Lys-66. NBD-Cl has been shown to react quicker with cysteine residues, however afterwards it may transfer to a spatially nearby lysine.[131, 132] UV spectrum data showed this may have occurred over time in this sample, with NBD-cysteine absorbing at 420 nm and NBD-lysine absorbing at 480 nm (figure 30). In either case, the surprising feature of the mass spectra is that the extra mass of the NBD moiety (+165 Da) could only be seen added to the first peak attributed to hRSV-M at 29351 Da and not to the latter peak with the extra +80 Da mass. This indicates that the change that gave the +80 Da found in a fraction of the native hRSV-M is blocking a change at Lys-66, and so they are likely the site of this modification. Unfortunately the tryptic digest was not able to identify directly a fragment with +80 Da, however the conflict with the additional NBD limits the possibilities for the modification.

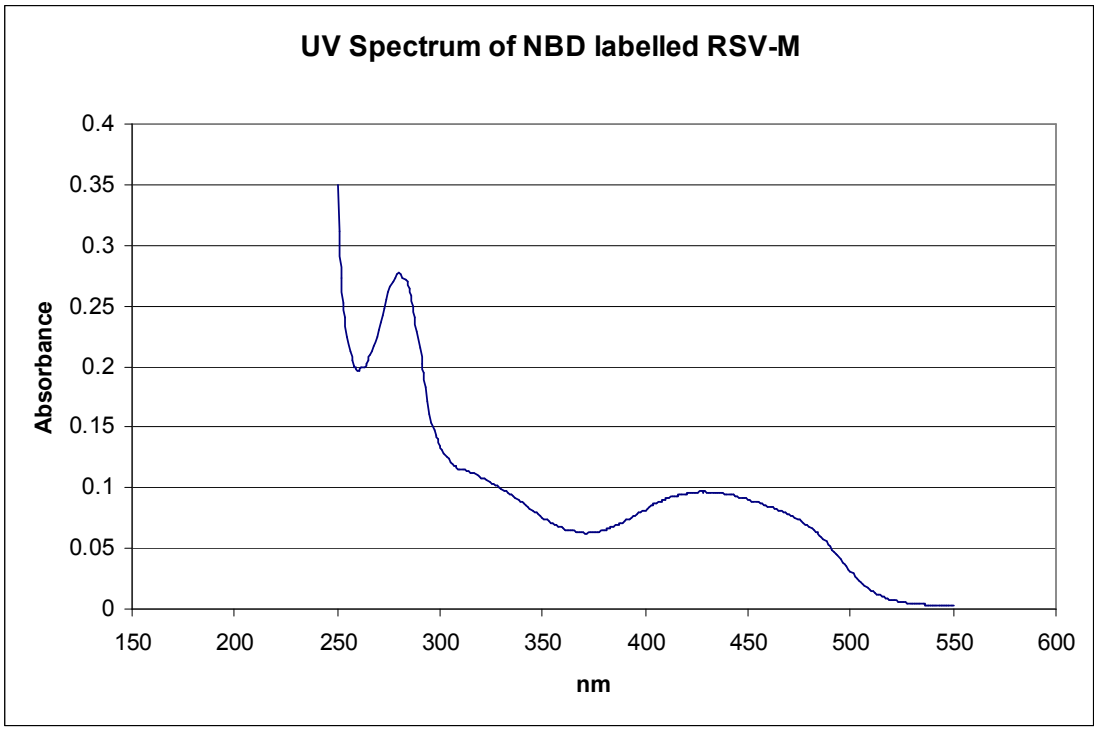

Figure 30 - U.V absorption spectra for hRSV-M-NBD

One theory was that the extra mass was due to bound metal ions, in particular an additional two calcium ions. While this does fit with the findings detailed previously for calcium bound to hRSV-M, this result makes it unlikely, since it would require

two tightly bound calcium ions while we now know one is weakly bound, and ICPMS data only showed one calcium bound per protein molecule after heavy loading of calcium. Furthermore, the NBD labelling experiments were conducted in the absence of calcium, and so it should not have interfered if this was the case. A more likely theory shown by this data is that the reactive cysteine residue has become modified and so is blocked from reacting with the NBD-Cl, and hence no transfer to lysine. A likely modification that may have occurred after purification is the oxidation of the thiol side group into either sulfenic acid (SOH) or sulfinic acid (SOOH) groups. This reaction occurs in the presence of hydrogen peroxide, and so can be seen when proteins are stored in water for a length of time[133]. Furthermore, in the mass spectra above several smaller peaks can be seen that correspond to the +16 Da or +32 Da that each of these oxidised species would add. The species present at 29381 Da corresponds to a single cysteine forming the sulfenic acid, while the main secondary peak at 29431 Da may result from all 5 cysteines present in hRSV-M being converted to the sulfenic form for a total of +80 Da.

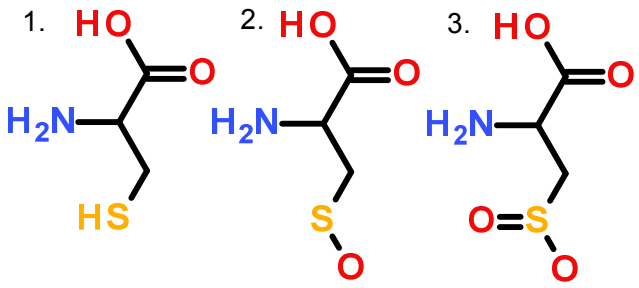

Figure 31 - 1. Cysteine, 2. Sulfenic acid derivative, 3. Sulfinic acid derivative

2.7 Interactions with lipids – Lipids of interest

This work is a continuation of previous work in the group by Helen McPhee. Special thanks should also be given to masters student Amy Fry for helping collect some of the isotherms involved.

A number of experiments were carried out in order to observe the behaviour of hRSV-M interacting with lipids, as detailed later in this chapter. The lipids used were chosen

based on previous experiments, and on literature suggesting they may be interesting targets for hRSV-M.

Typical eukaryotic cell membranes consist of glycerophospholipids, sphingolipids and sterols. Glycerophospholipids are the major species of lipid in cell membranes, although this can divided into many types. They consist of a glycerol backbone with two fatty acid tails and a polar head group. Sphingolipids are similar, except the backbone is consists of a sphingosine moiety and hence only have one additional fatty acid chain and are usually found in much smaller amounts. Sterols tend to be smaller planar structures that are found intercalating between the other lipids, and modulating the structure of the membrane.

Among lipids, the nature of fatty acid tails are considered to be most involved in changing the membrane's fluidity. The fatty acid tails resides within the hydrophobic core of the membrane bilayer and so changes in their length and degree of saturation have a large effect on membrane fluidity through changing the packing of the lipids. This makes the selection of fatty acid tail lengths for experiments crucial to determine the layer's properties. While tails lengths vary from C6 to C24, the most common chain lengths found in mammalian cell membranes are C14, C16 and C18. These all exist in the gel phase, and so can be used to study a fluid membrane, as is seen in living systems.[134] For these experiments, a range of C16, C18 and mixed lipids were used.

The head groups of phospholipids are very important for studying lipid interactions, since it is known hRSV-M interacts with the surface of a membrane.[47] Phosphatidylcholines were the most frequently used lipid, since they are the most common found in nature, both in lung cell membranes and in virus envelopes related to hRSV. These small neutral lipids form a useful scaffold for other lipid species to be embedded in. The other main focus of this project was phosphatidylserine based lipids. This lipid head group is highly negatively charged and has been included because it has been previously identified as involved in the binding of several other viral proteins to lipid membranes.[135] It is also a major component of cell membranes, as detailed below, and the presence of a large positively charged surface on hRSV-M may indicate an interaction with negatively charged patches on the membrane.

A combination of sphingomyelin and cholesterol were also studied, both in mixtures and separately. Mixture of sphingomyelin, cholesterol and a phosphatidylcholine based lipid are known to produce phase separation, creating liquid ordered domains of sphingomyelin and cholesterol separate from liquid disordered domains of phosphatidylcholine based lipids. These form the basis of lipid microdomains, often called lipid "rafts", found in cell membranes.[136] These microdomains have been identified as a location for viral assembly and budding for several different viruses, including hRSV.[19, 137, 138]

Lipid Component	% of total lipids
Phosphocholine	34
Phosphoethanolamine	32
Phosphoserine	13
Phosphoinositide	9
Sphingomyelin	11

Table 8 - Phospholipids found in the plasma membrane of human lung tissue[139]

Fatty Acid Chain	% total fatty acids
16:0 – palmitoyl	4
18:0 – stearoyl	20
18:1 – oleoyl	40
18:2 – linoleoyl	2
18:3 - linolenoyl	8

Table 9 - Fatty acid composition of lipids from A549 lung epithelial cell plasma membranes[140]

	% of phospholipids				
Virus family	**PC**	**PE**	**SM**	**PS**	**PI**
Paramyxoviridae	8-53	10-41	12-30	2-17	0-11
Rhabdoviridae	16-38	20-34	16-31	7-20	0-10
Orthomyxoviridae	10-39	12-45	16-23	7-22	0-8
Togaviridae	21-49	19-35	7-29	9-21	0-9
Retroviridae	16-30	26-42	22-33	12-17	0-4

Table 10 - Percentage of phospholids found the the envelope of several families of RNA viruses.[141] PC = Phosphocholine, PE = Phosphoethanolamine, SM = Sphingomyelin, PS = Phosphoserine, PI = Phosphoinositide

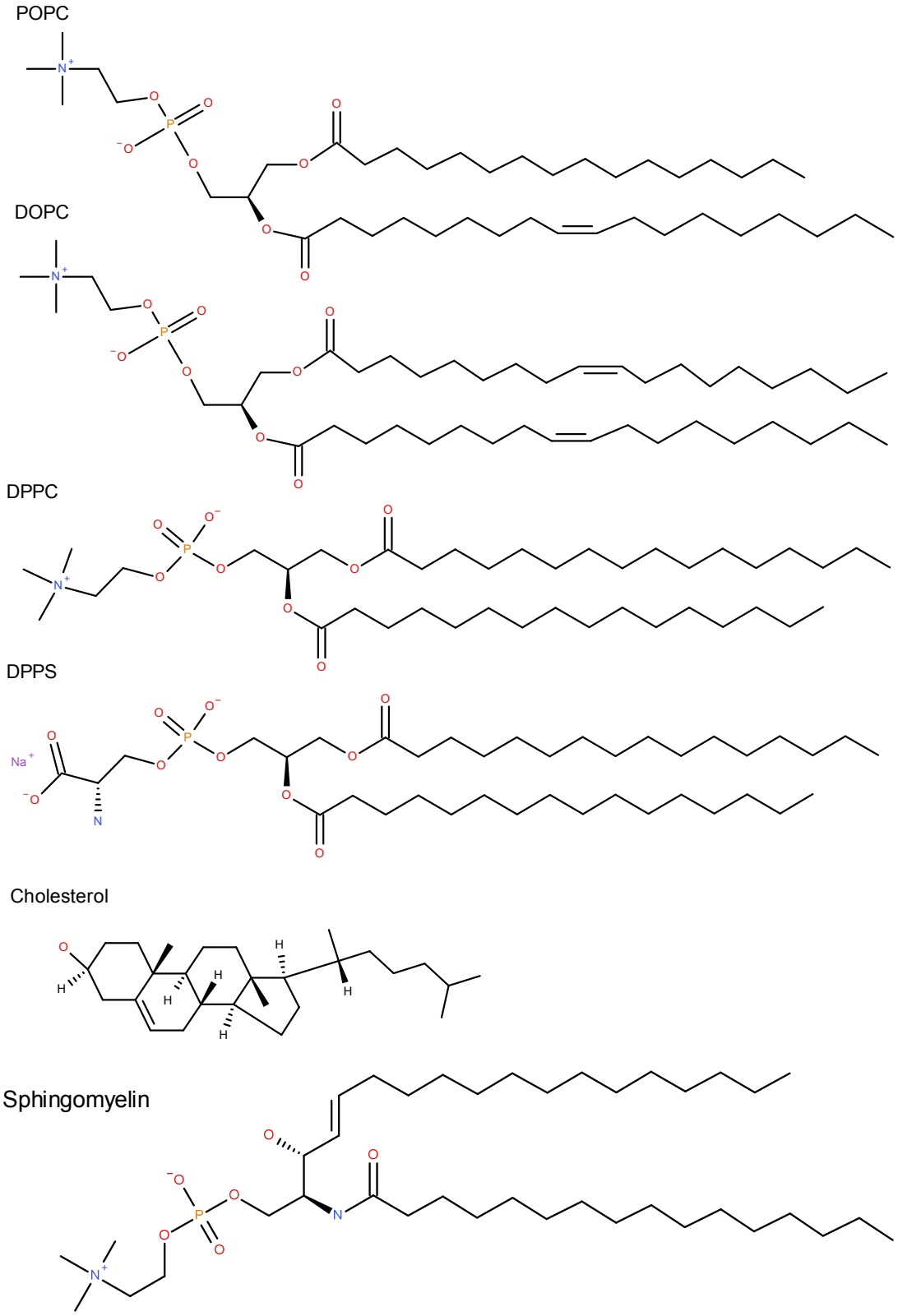

Figure 32 - Lipids used for experiments with hRSV-M. Top to bottom, 1-palmitoyl-2-oleoyl-sn-glycero-3-phosphocholine (POPC), 1,2-Dioleoyl-sn-glycero-3-Phosphatidylcholine (DOPC), 1,2-dipalmitoyl-sn-glycero-3-phosphocholine (DPPC), 1,2-Dipalmitoyl-sn-glycero-3-phosphoserine (DPPS), Cholesterol, Sphingomyelin C16.

2.8 Langmuir Adsorption Isotherms

2.8.1 Theory

When studying the effect of a protein on lipids, it would be advantageous to be able to conduct experiments on a bilayer system. However in practice these experiments are often difficult to perform, with problems in obtaining a stable bilayer in a manner that can be probed for quantifiable data. As such, it is often necessary to use a monolayer of lipids as a model system. A monolayer is a useful system since it can be formed easily at an air-water interface due to the amphiphilic properties of lipids, and a bilayer can be approximated to two coupled monolayers joined by their hydrophobic surfaces.[142] Lipids applied to the surface of water will spontaneously form a monolayer. This is because the polar head groups of lipids will orientate themselves towards the water layer, while the hydrophobic tails will be repulsed by the polar liquid surface. The properties of monolayers at the interface of air and water have been found to mimic the properties of a bilayer closely.[143]

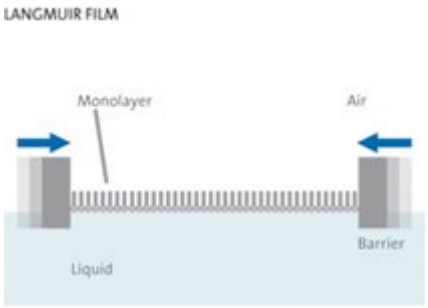

Figure 33 - A lipid monolayer on a Langmuir-Blodgett trough (©KSV Nima)

To study the effect of hRSV-M on a lipid monolayer, a Langmuir-Blodgett Trough was used. The trough is composed of a hydrophobic surface of Teflon, and is filled with a buffer solution to act as the subphase. Two moveable Delrin barriers sit at the surface level to vary the exposed area of the subphase surface. The monolayer is formed by the addition of the lipids dissolved in a volatile solvent to the surface. As the solvent evaporates the monolayer is formed. The surface pressure (Π) of the surface can be monitored using a Wilhelmy plate attached to a microbalance.

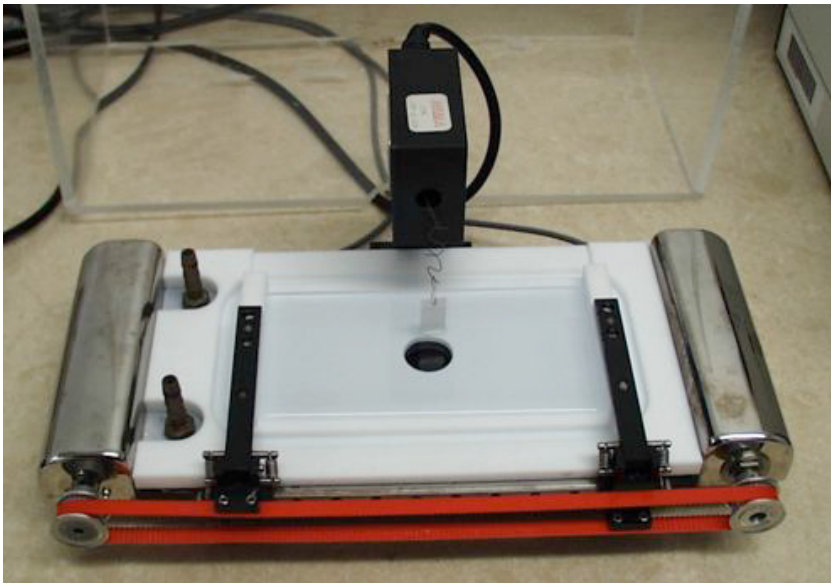

Figure 34 - The Langmuir trough (KSV Nima) used in these experiments

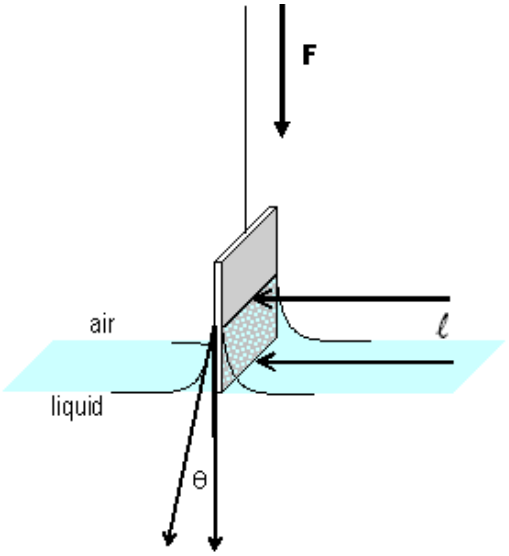

Figure 35 - A Wilhelmy plate, showing the contact angle (θ), contact surface (l) and downward force applied (F)

The surface pressure can be found by the forces acting upon the Wilhelmy plate. The forces acting on the plate are the surface tension (γ) downwards, the Archimedes buoyancy (A), and its weight (P). These combined with the width and thickness (w + t) of the Wilhelmy plate and contact angle (θ) give the following equation.[144]

$$f = P + 2\gamma(w + t)\cos\theta - A$$

Equation 10

When the Wilhelmy plate is completed hydrated, the contact angle, θ, is 0° and so cosθ=1. The thickness of the Wilhelmy plate can also be considered to be negligible compared with the width when calculating the perimeter. These give the equation:

$$f = P + 2\gamma w - A$$

Equation 11

The weight (P) and buoyancy (A) are constant during an experiment, the change in surface tension can be modelled as:

$$\Delta f = 2w(\gamma - \gamma_0) = -2w\Pi$$

Equation 12

Where Π is the change in surface pressure relative to the surface pressure of a clean subphase (γ_0), which is 71.97 mN/m. Once measurements have been made, a plot of surface area per molecule against surface pressure can be made to give the pressure/area isotherm. From this we can see how the monolayer properties change with a reduction in area per molecule.

When analysing the data obtained, we want to look at the surface excess of the components in the monolayer. This is a measure of how much greater the material has an affinity for the interface over the bulk subphase. For a two component system this is represented by the Gibbs absorption isotherm, and is given by the following equation:

$$d\gamma + \Gamma_1 d\mu_1 + \Gamma_2 d\mu_2 = 0$$

Equation 13

Where Γ is the surface excess (defined as n^s/s, the concentration at the surface over the area) and μ is the chemical potential. For a system in which the surface excess of one component, the solvent in this case, is reduced to zero the equation can be written as :

$$d\gamma = \Gamma_2 d\mu_2$$

Equation 14

By taking the relationship for μ:

$$\mu_2 = \mu_2^0 + RT \ln a_2$$

Equation 15

Where *a* is the activity and μ_2^0 is the standard chemical potential, then equation 14 can be rewritten as:

$$\Gamma_2 = -\frac{1}{RT}\left(\frac{d\gamma}{d \ln a_2}\right)$$

Equation 16

This is the Gibbs adsorption isotherm. This allows us to calculate the surface excess given the change in surface tension.[145]

However, when studying a protein binding or inserting into a monolayer at the interface, this equation is not detailed enough to give an adequate model. Other models have been derived from the Gibbs adsorption isotherm which can be used for more complex systems like protein-lipid interactions. The first is the ordinary Pethica equation, which extends the adsorption isotherm to a system with one soluble component (the protein) and one insoluble component (the lipid monolayer) and is defined as:

$$\left(\frac{\partial \Pi}{\partial \ln c_2}\right)_{\theta_1} = \frac{RT\Gamma_2}{(1-\Theta_1)}$$

Equation 17

Where Θ_i is the monolayer coverage ($\Gamma_i/\Gamma_{\infty i}$) and c_i is bulk concentration of the soluble component. If the monolayer can be described as an ideal mixture of the two components, then it can also be described by a generalised Szyszkowski-Langmuir equation:

$$\Pi = -\frac{RT}{\omega_\varepsilon}\ln(1-\Theta_1-\Theta_2)$$

Equation 18

With ω_ε, the mean molar area being:

$$\omega_\varepsilon = \frac{\Gamma_1\omega_1 + \Gamma_2\omega_2}{\Gamma_1+\Gamma_2}$$

Equation 19

Differentiating equation 18 with respect to Θ_2 (and assuming Θ_1 and ω_ε are constant) gives:

$$\left(\frac{\partial\Pi}{\partial\Theta_2}\right)_{\theta_1} = \frac{RT}{\omega_\varepsilon}\cdot\frac{1}{1-\Theta_1-\Theta_2}$$

Equation 20

Given this relationship between the Pethica equation (17) and equation 20, they can be combined to give:

$$d\ln c = \frac{1-\Theta_1}{\Theta_2(1-\Theta_1-\Theta_2)}d\Theta_2$$

Equation 21

That can be integrated to give a modified Langmuir binding isotherm:[145]

$$Kc_2 = \frac{\Theta_2}{(1-\Theta_1-\Theta_2)}$$

Equation 22

Where K is the absorption equilibrium constant for an soluble surfactant and an insoluble monolayer. This equation will be used in the fitting of experimental data later.

Langmuir isotherms were carried on using a subphase of PBS, the surface of which was thoroughly cleaned before each experiment. The surface pressure was first taken

and used as a base level for the experiments. Protein was then pipetted onto the subphase surface, followed by the lipids dissolved in chloroform. This was then allowed to equilibrate for 20 minutes before beginning compression of the monolayer.

2.8.2 hRSV-M only monolayer

hRSV-M was first applied to a clean subphase surface, in order to see how it behaves at the air-water interface. An individual aliquot of hRSV-M was added to the surface and left for 20 minutes to equilibrate. The surface pressure was then recorded and a further aliquot was added. This was repeated over a range of concentrations to determine how the pressure depends on protein concentration. The following equation can then be used to fit the data and calculate important parameters for the protein.[146]

$$\gamma_{lv} = \left(\frac{\gamma_{lv}^{o} - \gamma_{lv}'}{1 + (\ln C_B^{\Pi/2} / \ln C_B)^N}\right) + \gamma_{lv}'$$

Equation 23

Where γ_{lv}^{o} and γ_{lv}' are the lower and upper concentration asymptotes (giving the surface pressure for the clean subphase and protein saturated surface respectively), C_B is the protein concentration of the subphase, $C_B^{\Pi/2}$ is the protein concentration at half the maximum change in surface pressure, and N is a description of the gradient of this section.[147] Experimental results are displayed below:

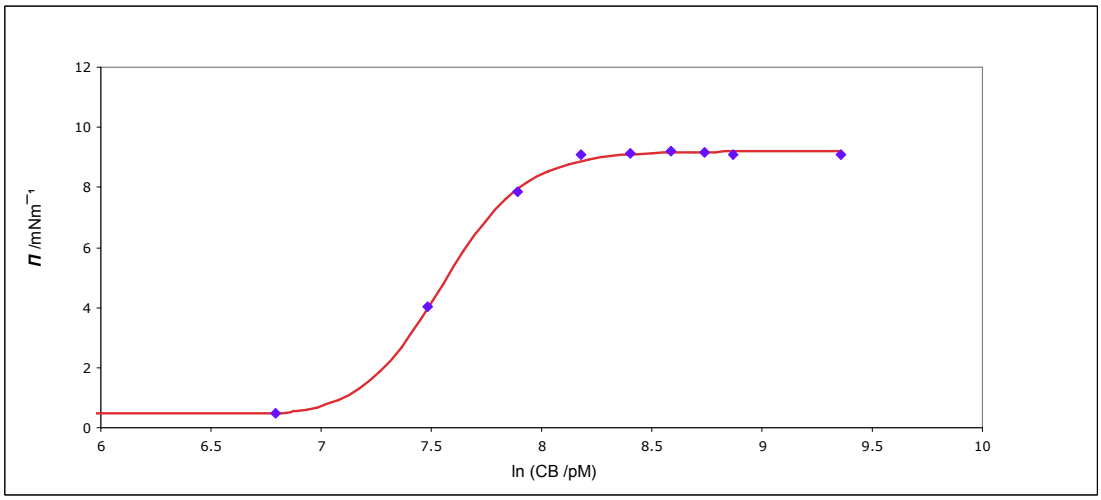

Figure 36 - Surface pressure as a function of protein concentration for hRSV-M additions to an air-water interface on a Langmuir trough. Data subsequently fit using equation 23.

$C_B^{\Pi/2}$	1902 pM
Π^{max}	8.85 dyn/cm
Γ	6.78 pmol/cm^2
Area per molecule	2447 Å^2

Table 11 - values for hRSV-M calculated from data fitting in figurer 36

This data concurs with that reported previously.[47] This shows that the change in purification method for hRSV-M has not altered the surface properties of the protein. A pressure/area isotherm was also ran on a saturated surface of hRSV-M. While most surface active species cannot go above the equilibrium spreading pressure without collapsing back into the subphase, the results here show that hRSV-M is able to attain a meta-stable state and reach much higher pressures. A collapse point for the layer was not reached even when compressed to the smallest area the trough could make. When the monolayer was allowed to relax the pressure dropped back to the spreading pressure. This suggests that hRSV-M is able to closely pack together and form a more condensed phase.[148]

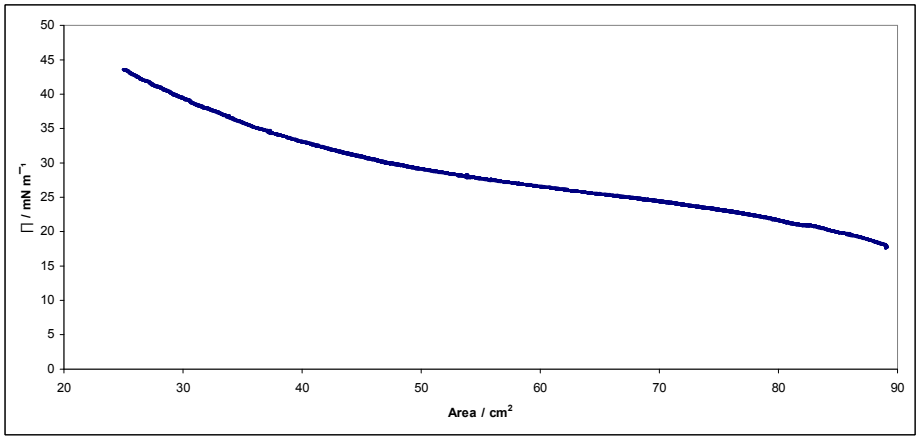

Figure 37 - Pressure/Area isotherm for a saturated surface of hRSV-M

2.8.3 hRSV-M on lipid monolayers

The data was obtained as the effect of monolayer compressions using different lipid compositions and for a range of different hRSV-M subphase concentrations. This work is a continuation of earlier isotherms published in Ref.1 (McPhee *et. al*.)

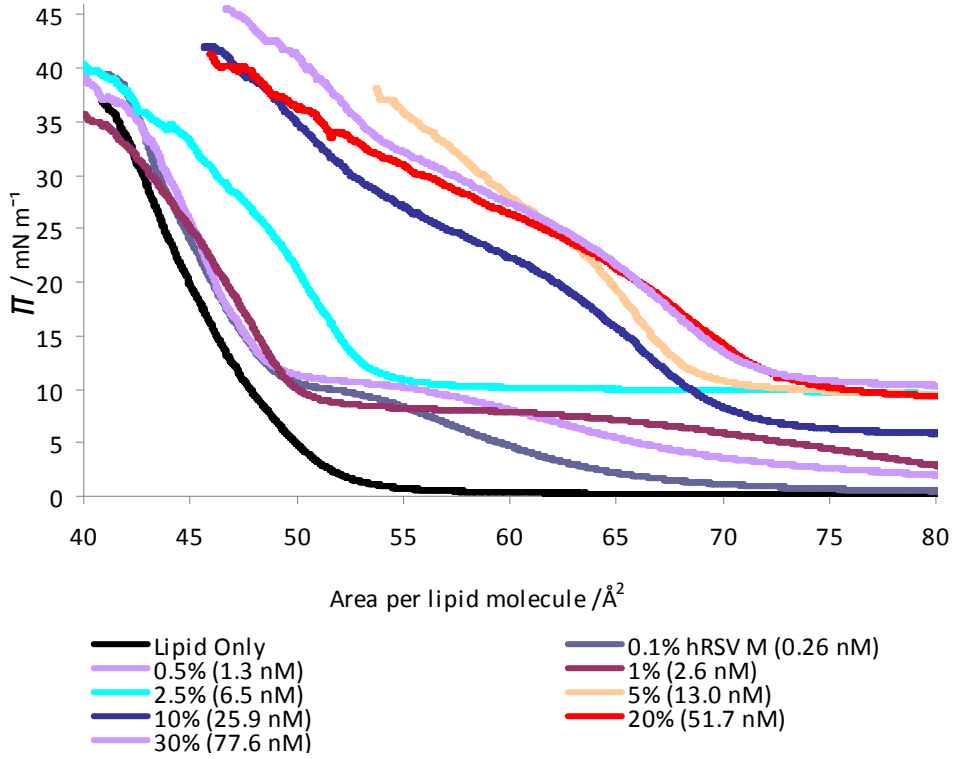

Figure 38 - Pressure/Area isotherm for 7ug Cholesterol with hRSV-M additions (% by mass, molarity in brackets)

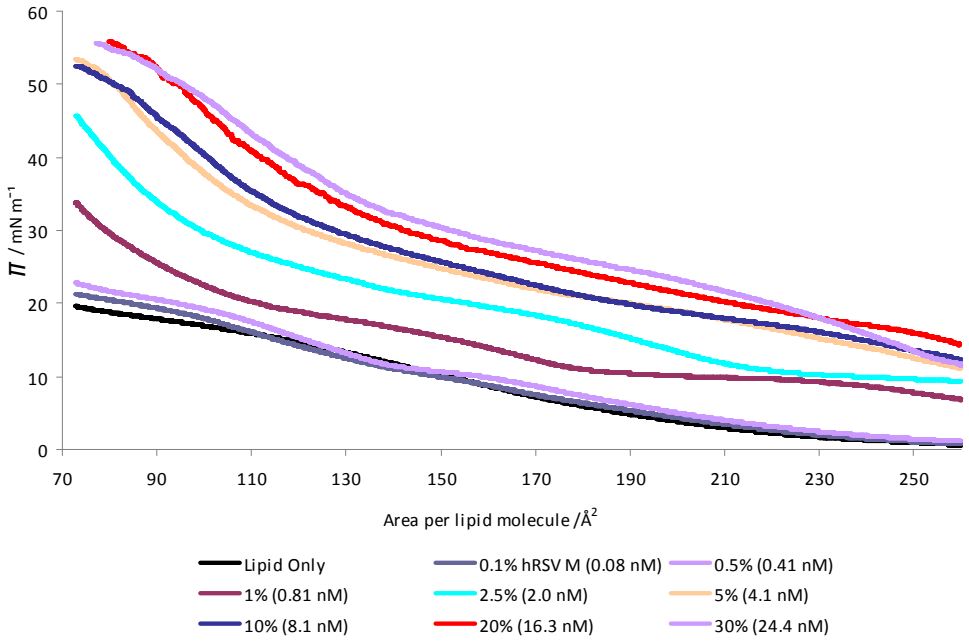

Figure 39 - Pressure/Area isotherm for 4ug Sphingomyelin with hRSV-M additions (% by mass, molarity in brackets)

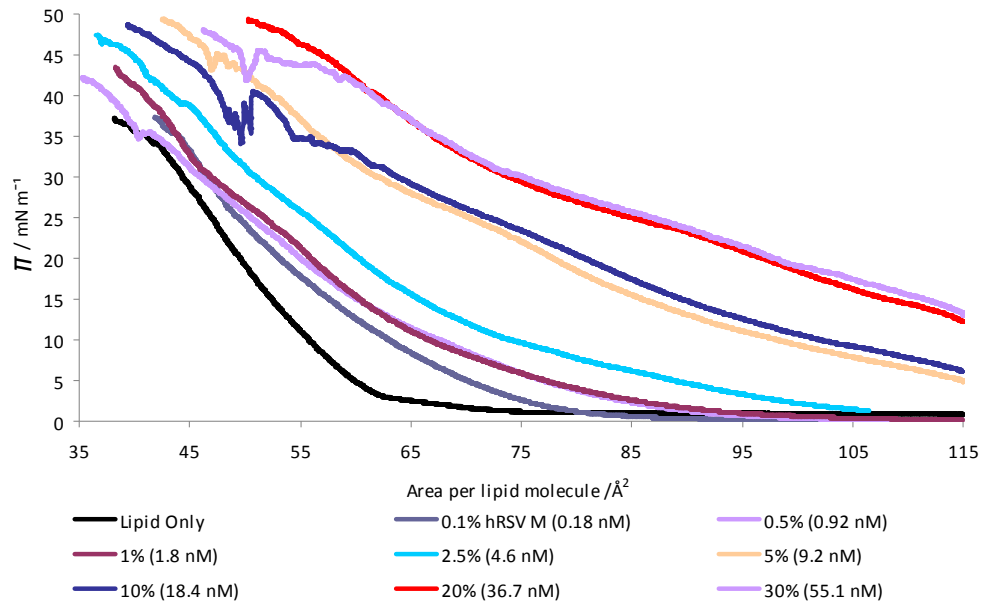

Figure 40 - Pressure/Area isotherm for 7ug Cholesterol / Sphingomyelin (1:1 w/w) with hRSV-M additions (% by mass, molarity in brackets)

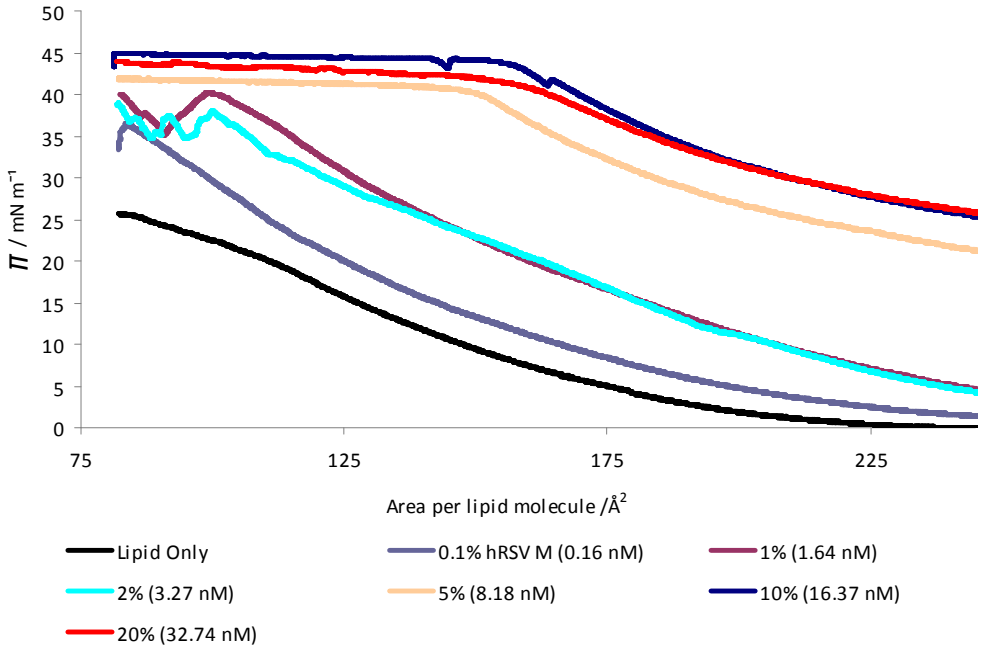

Figure 41 - Pressure/Area isotherm for 4ug DOPC + DPPS (4:1 w/w) with hRSV-M additions (% by mass, molarity in brackets)

All of the above isotherms show that for an increase in the subphase concentration of hRSV-M, there is an increase in the initial surface tension of the monolayer. They also all show that for a given subphase concentration of hRSV-M, the monolayer becomes saturated and no change is seen for further amounts of protein added.

The isotherm with cholesterol alone shows that for the low protein amounts (0.1-1%) the protein is partitioning into the monolayer. As the area is decreased, hRSV-M is then forced out of the monolayer, giving the plateau seen at approx 8.85 mN m^{-1}. This is the same as the equilibrium spreading pressure for hRSV-M alone. Once the protein has all been forced out at around 50Å area per lipid, the isotherm reverts to its lipid-only state. For higher amounts of protein, (>2.5%), it is likely that the protein has formed the majority of the monolayer, and so the cholesterol has not been able to fit into the monolayer and has been removed into the subphase. This results in the isotherms appearing to be similar to that for a saturated protein layer alone.[47]

The isotherm with sphingomyelin alone shows much of the same features, with a plateau at 8.85 mN m^{-1} for low protein concentrations. However, it appears that to all the protein has been forced out, since the isotherm shifts towards a higher area per lipid molecule, indicating that HRSV-M has intercalated with the lipid. This trend can be seen across all protein concentrations, with the plateau only disappearing when the starting pressure is higher than it. This indicates that an interaction is occurring between hRSV-M and sphingomyelin. The increase in the surface area per lipid molecule relative to the surface pressure indicates that a more diffuse monolayer is being formed, one comprising both sphingomyelin and hRSV-M.

Figure 40 showing the isotherm involving a lipid mix of cholesterol and sphingomyelin does not have the same plateau shown in the others. This indicates that when a mixture of these lipids are used hRSV-M is not forced out of the monolayer as it is compressed, and stays as a part of it after insertion. Increased protein concentration gives a much higher surface pressure at larger areas per lipid molecule, showing that the hRSV-M and lipids are interacting with each other. Furthermore, the collapse pressure of the monolayer (Π^{max}) increases steadily from 38.14 mN m^{-1} for the lipid mixture alone to 50.22 mN m^{-1} at 5% hRSV-M and above. This shows that the monolayer comprising lipid and protein is more stable than the monolayer of lipid alone, resisting collapse until a higher pressure is applied.

These three isotherms were carried out to compare with an earlier isotherm for a ternary mixture of DOPC/Sphingomyelin/Cholesterol, a mixture that creates domains of L_o and L_d phases..[47] This showed a plateau at the same pressure (8.85 mN m^{-1})

indicating that protein was forced out of the monolayer, but then showed a decrease in pressure for a given area, showing the addition of protein causing the monolayer to condense. This was interpreted as the protein being forced out of the liquid disordered areas of the monolayer comprised mainly of DOPC, while causing a condensation of the ordered domains of the monolayer. The results here appear to show that this behaviour is unique to this ternary mixture, since combinations of the individual components failed to replicate this behaviour.

The isotherm for the DOPC/DPPS (4:1) mixture shows a large increase in the pressure relative to area per molecule, with the Π^{max} being reached at between 2-5%. This indicates insertion of the protein into the monolayer, and a more stable monolayer being formed, with hRSV-M having a high affinity for this partitioning. This may be indicative of a specific interaction between hRSV-M and phosphatidylserines.

Cross sections at a constant area per lipid molecule through these isotherms were taken and fit to the modified Langmuir binding isotherm (equation 22). The area per lipid molecule for each was chosen to be above any phase transition pressures. The isotherm for a cholesterol monolayer could not be fit by this method, since its behaviour was significantly different at higher and lower protein concentrations.

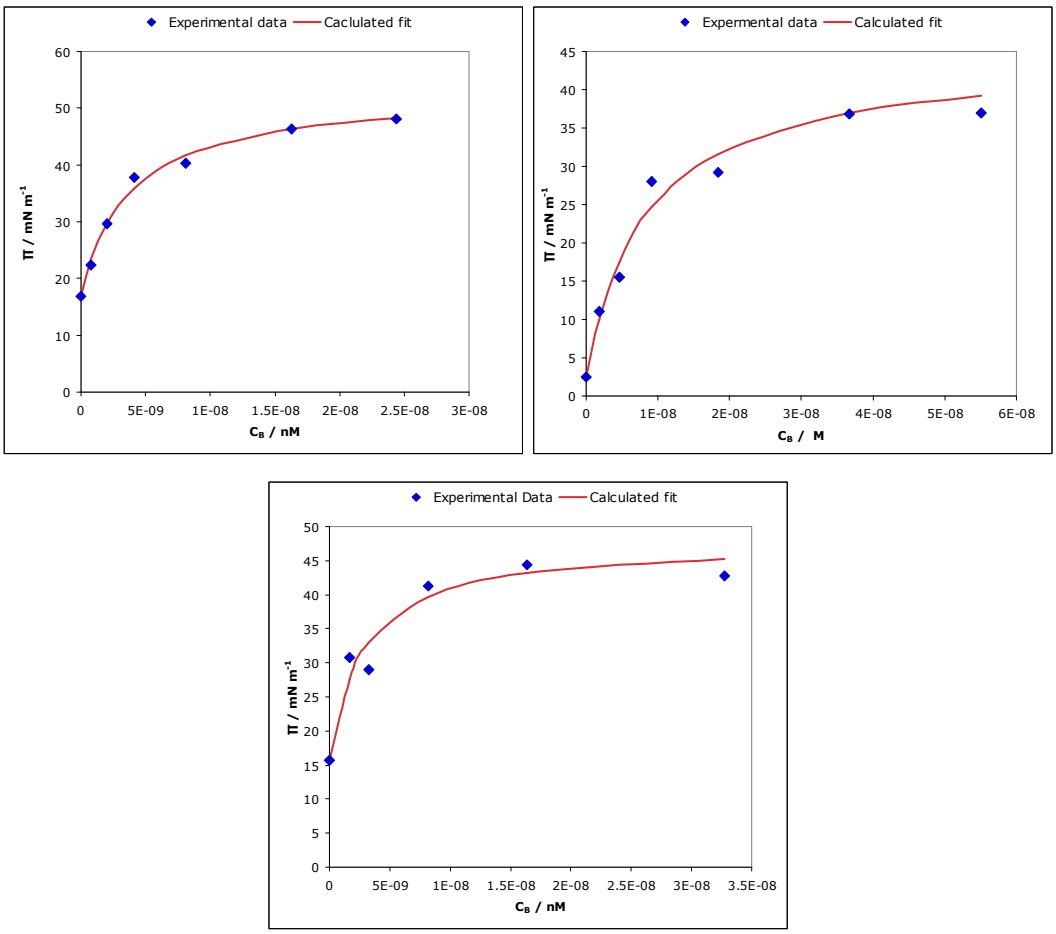

Figure 42 – Adsorption isotherms corresponding to cross sections of pressure / area isotherms at a fixed area per lipid molecule as a function of C_B. Top left, Sphingomyelin A = 100 Å^2 per lipid molecule, ω_Σ = 24 Å^2. Top right, SM/Chol A = 65 Å^2 per lipid molecule, ω_Σ = 31 Å^2. Bottom, DOPC/DPPS A = 125 Å^2 per lipid molecule, ω_Σ = 45 Å^2

Lipid	C_B at surface saturation / nM	Adsorption Equilibrium Constant K / M^{-1}
Sphingomyelin	≥ 2	2.72 x 10^{-8}
Sphingomyelin/Cholesterol 1:1	≥ 4.5	1.20 x 10^{-8}
DOPC/DPPS 4:1	≥1.5	3.56 x10^{-8}

Table 12 - Summary of parameters for hRSV-M adsorbing to lipid monolayers

The data collected show that a monolayer containing DOPC/DPPS has a greater adsorption equilibrium constant and a low surface saturation, and therefore an increased affinity of hRSV-M for this monolayer. The SM/Chol monolayer appears to result in a lower affinity than a monolayer of SM alone, with a lower CB of 4.5 nM versus 2 nM, however this may be the result of different modes of interaction, with

hRSV-M intercalating into the sphingomyelin monolayer as opposed to it interacting with the surface of a SM/Chol monolayer.

2.9 Brewster Angle Microscopy

It is possible to directly visualise the surface of a Langmuir film using a technique called Brewster angle microscopy (BAM). When polarised light is directed onto a liquid surface, the light can be refracted into the liquid or reflected away. The amount of light that goes in each direction depends on the incident angle, due to the change in refractive index of the air to water transition. At a unique angle, called Brewster's angle, the reflected component is zero and so a camera pointed at the surface (also at Brewster's angle) will detect no signal off the subphase surface. This angle is determined by Snell's law, and for water is approximately 53°.[149]

$$\tan \alpha = n_2 / n_1$$

Equation 24 - Snell's law. α is Brewster's angle, n_2 and n_1 are the refractive index of the subphase and air respectively

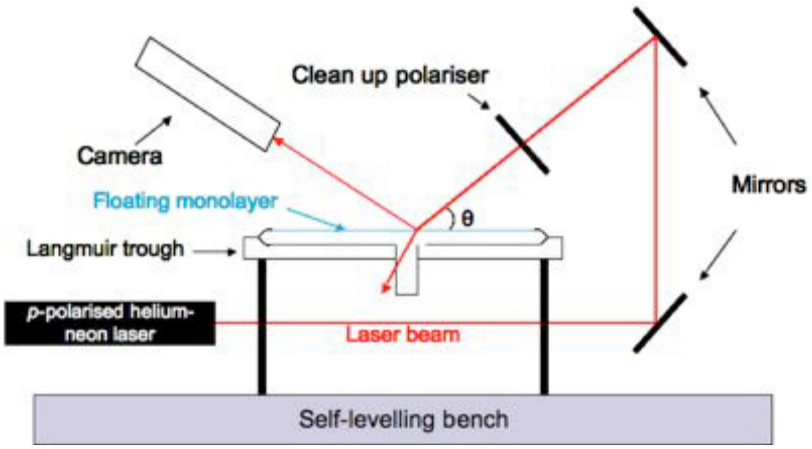

Figure 43 - Schematic for the Brewster angle microscope setup used

When the surface of the subphase is changed, for example by the addition of a monolayer, the refractive index for this boundary now changes as well. This leads to light now being reflected off the monolayer, while any exposed subphase remains dark. Since the refractive index of the surface monolayer is dependant on its structure, the images produced can reveal structural features of the monolayer. In the following

experiments it can also reveal any changes in structure caused by additions of hRSV-M.

Brewster angle microscopy has several advantages over other techniques for visualising protein-lipid interactions, such as fluorescent microscopy and atomic force microscopy. The technique can be carried out by on unmodified proteins and lipids, unlike traditional fluorescent microscopy which require additional fluorescent tags to be added. It also allows the whole layer to be viewed simultaneously, while fluorescent markers may partition differently between different phases that are formed. It is also a much more time sensitive experiment than atomic force microscopy, which requires the sample to stay stable for a while for each image to be acquired, while BAM is acquires images in real time.[150]

All experiments were carried out on the same trough as the previous isotherm experiments. Once the subphase was added to the trough, the clean up polariser and mirror angles were adjusted till zero reflection was detected by the camera. These settings were not changed for the remainder of the experiment. Protein and lipids were then applied in the same manner as for Langmuir isotherms. These experiments were only carried on using DOPC/DPPS (4:1 w/w) as a lipid mixture.

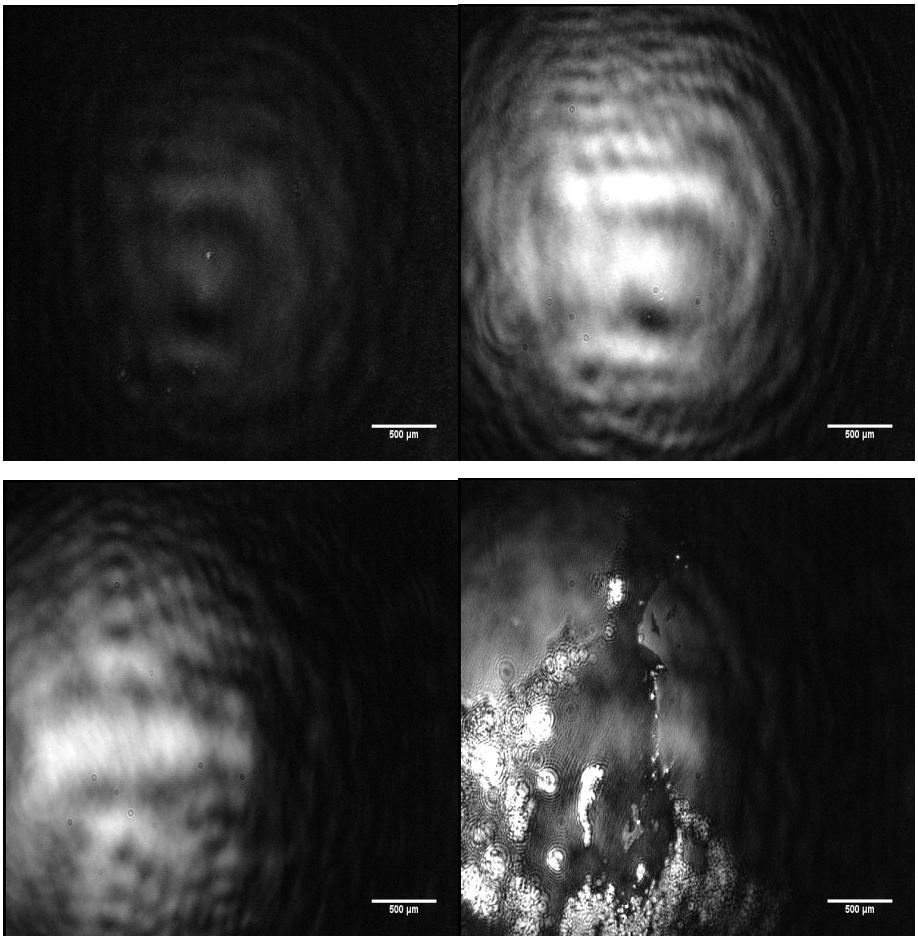

Figure 44 - BAM images from isotherm of hRSV-M compression. top left = clean subphase, top right = hRSV-M at Π^{max} (8.9 mN m^{-1}), bottom left = hRSV-M at metastable 26.3 mN m^{-1}, bottom right = hRSV-M layer after disruption with pipette tip

The images of hRSV-M alone show that it readily forms a homogenous monolayer on the subphase surface, as seen by the change in contrast of the images. When the monolayer was disrupted with a pipette tip (figure 44 - bottom right), distinct edges could be seen where the monolayer was damaged. These tears would slowly close and return to the previous state, over a period of 20-30 minutes. This suggests that hRSV-M forms a fairly condensed layer at the surface that only equilibrates slowly with the subphase.

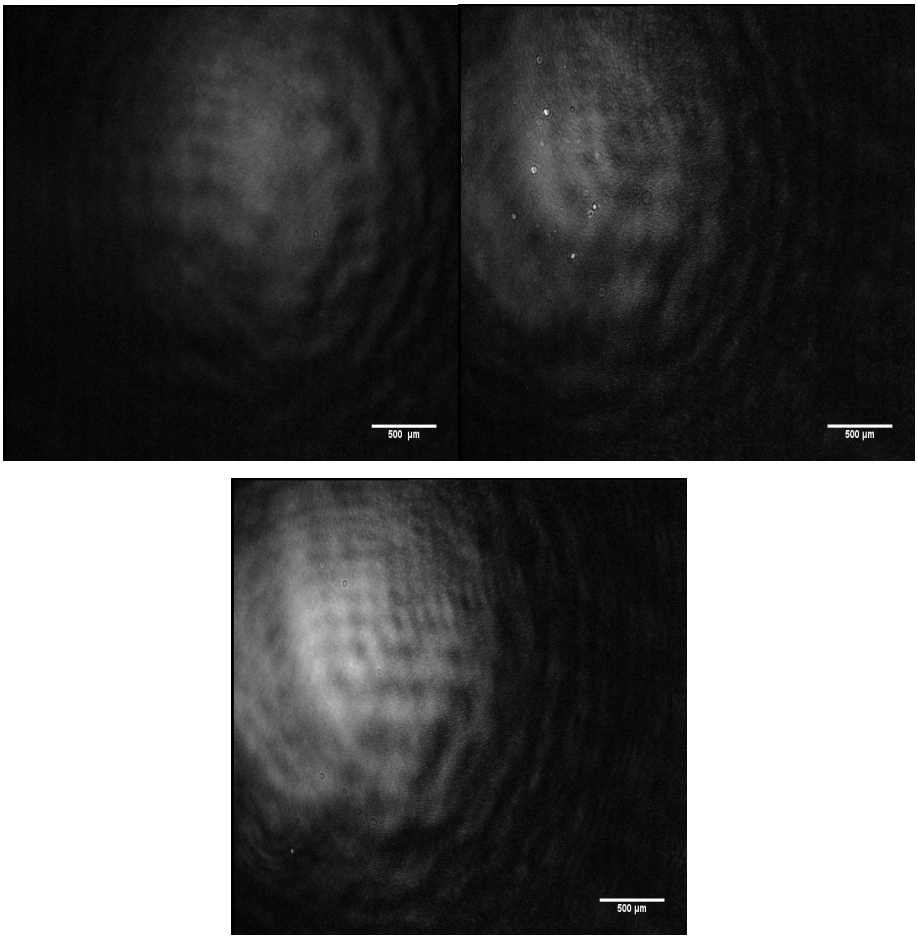

Figure 45 - BAM images from isotherm of 7µg DOPC/DPPS (4:1 w/w). Top left = clean subphse, top right = monolayer at Π=7.1 mN m^{-1}, bottom = monolayer at Π=37.2 mN m^{-1}

These images from lipid only isotherms show that while a condensation of the lipids can be seen as they change phase at higher pressures, they are still featureless homogenous surfaces.

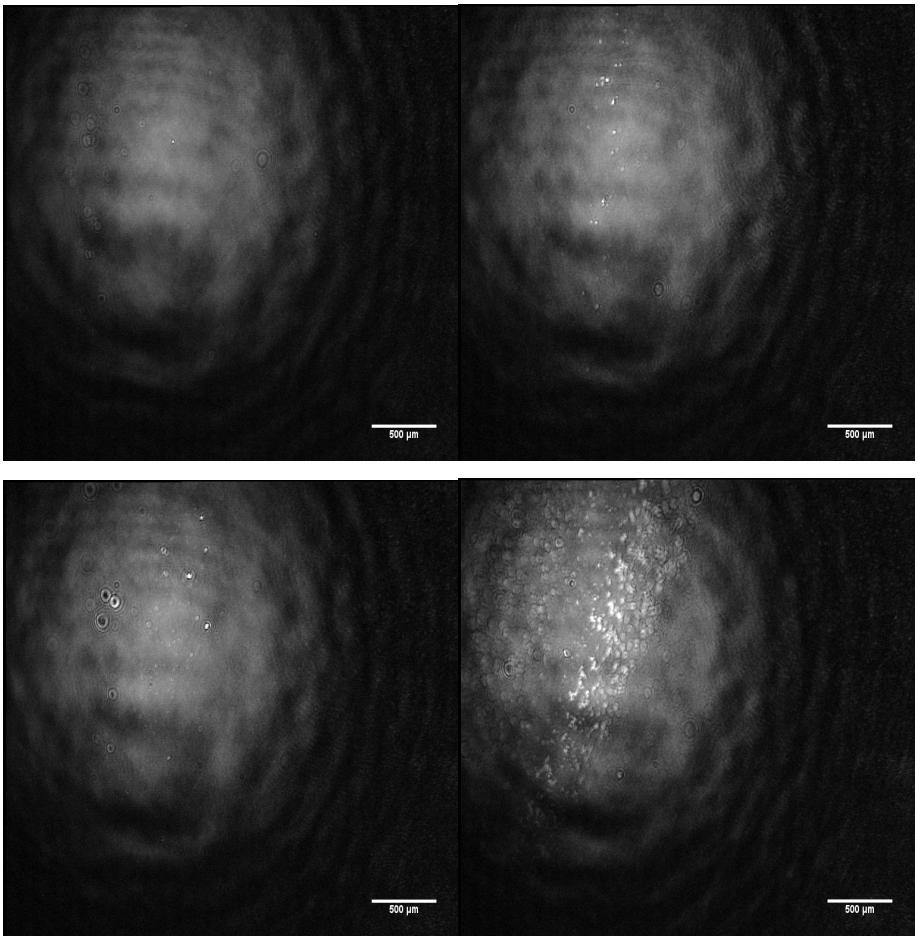

Figure 46 - BAM images from isotherm of 7µg DOPC/DPPS (4:1 w/w) with addition of 10% (w/w) hRSV-M (28.7 nM). Top left = monolayer at Π=21.4 mN m^{-1}, top right = monolayer at Π=30.6 mN m^{-1}, bottom left = monolayer at Π=37.1 mN m^{-1}, bottom right = monolayer at Π=40.1 mN m^{-1}

The addition of hRSV-M to the monolayer before compression dramatically changes the look of the monolayer. As the pressure is increased small (<50 µm) domains are seen to be formed, with them being most apparent close to the collapse pressure. Given the contrast for these domains is much greater than seen in the lipid only BAM images, it is likely that hRSV-M is involved in these domains. This may be the protein intercalating between the lipids, or binding to the head-group surface of the monolayer. To distinguish between these two possibilities, a DOPC/DPPS monolayer was formed at a fixed pressure above the equilibrium spreading pressure of hRSV-M (8.85 mN m^{-1}). At a higher pressure we would not expect to see the protein penetrating into the monolayer, however it would still be able to interact with its surface. All additions of protein were given 30 minutes to equilibrate. The pressure of the surface did not change significantly during the experiment.

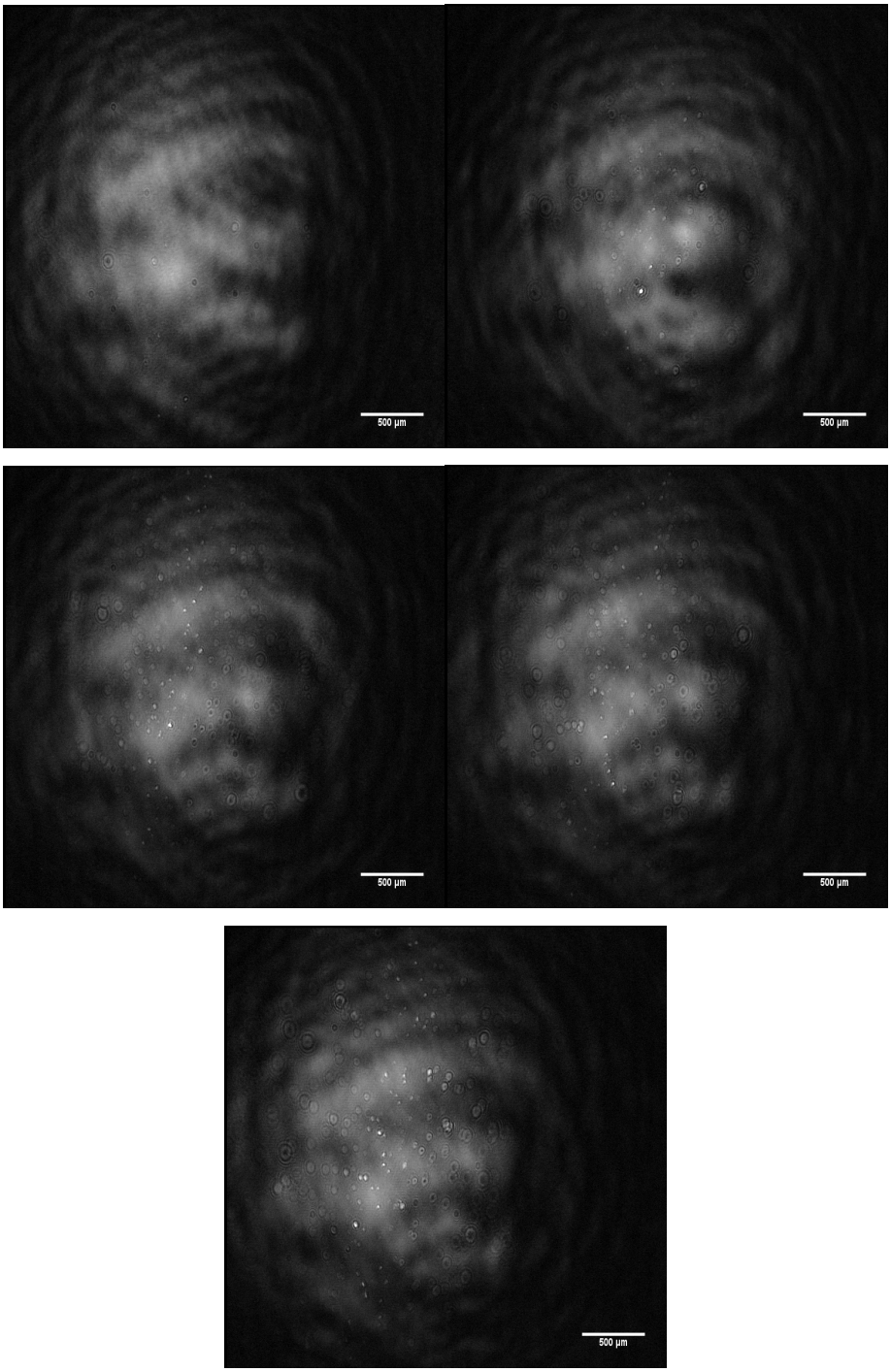

Figure 47 - BAM images of a 7µg DOPC/DPPS (4:1 w/w) monolayer at a fixed surface pressure of 23.2 mN m^{-1}, followed by additions of hRSV-M to the subphase. Top left = lipid only, top right = with 2% hRSV-M (3.28 nM), middle left = 5% hRSV-M (8.2 nM), middle right = 10% hRSV-M (16.4 nM), bottom = 25% hRSV-M (41 nM)

These images show the same small domain patterning as for the isotherm runs. This suggests that hRSV-M is interacting with the polar head groups of the lipids and

clustering them into small patches. These patches may indicate a clustering of proteins at each spot, possibly through protein oligomerisation.

2.10 Fluorescent tagging of hRSV-M

For a following experiment, it was necessary to attach a fluorescent moiety to hRSV-M so it could be visualised by microscopy. Initially an NBD moiety was used, however the fluorescent signal from the tagged protein proved to be too weak, and so this was replaced with a fluorescein isothiocyanate (FITC) tag. FITC is a commonly used fluorescent dye, due to its ready reactivity with nucleophiles such as amines, and its high quantum yield in solution. It is excited at 495 nm and emits at 519 nm, giving it a green colour.[151]

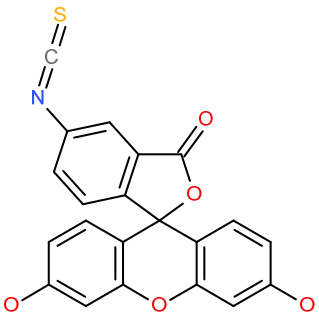

Figure 48 - Structure of fluorescein isothiocyanate

hRSV-M was reacted with FITC in a 1:1 manner, though the final labelling amount was calculated at between 25-40% by U.V spectroscopy (data not shown). Labelling was confirmed by SDS-Page gel electrophoresis, with the resulting gel being imaged in a fluorescent scanner set for green emissions.

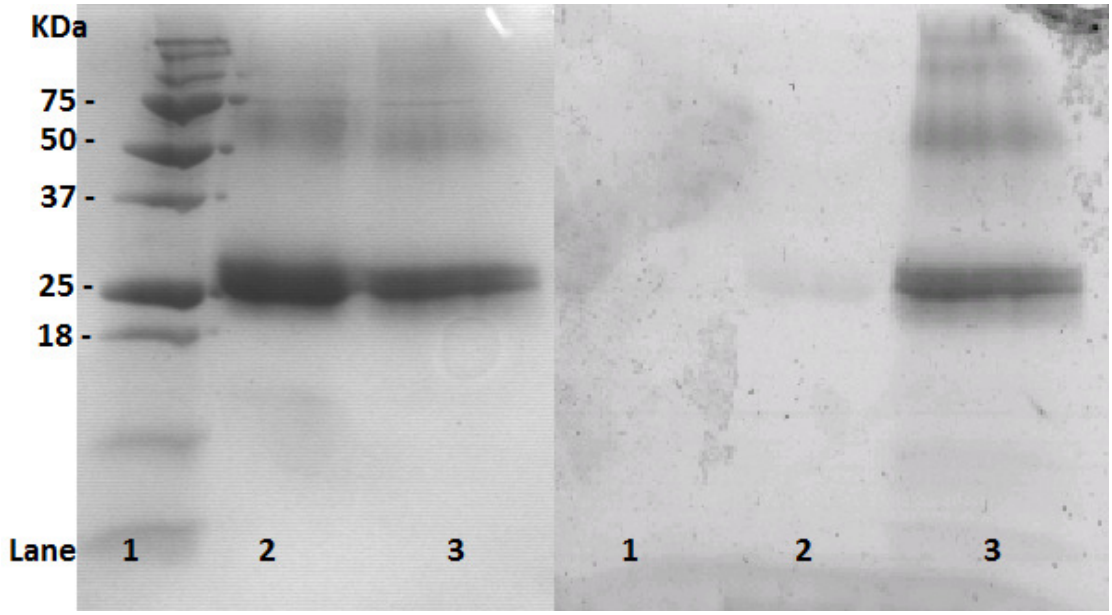

Figure 49 - SDS Page gel of FITC labelled hRSV-M. Left image = Coomassie stained gel with normal photograph. Right = Fluorescent scanned image at 520 nm. Lane 1 contains size markers, lane 2 is native hRSV-M, lane 3 is hRSV-M-FITC

As a check that the addition of FITC to hRSV-M had not dramatically changed its properties, it was subjected to the same Langmuir isotherm experiment as hRSV-M alone (see section 2.8.2) to determine if its surface active properties had changed significantly. The results are detailed below.

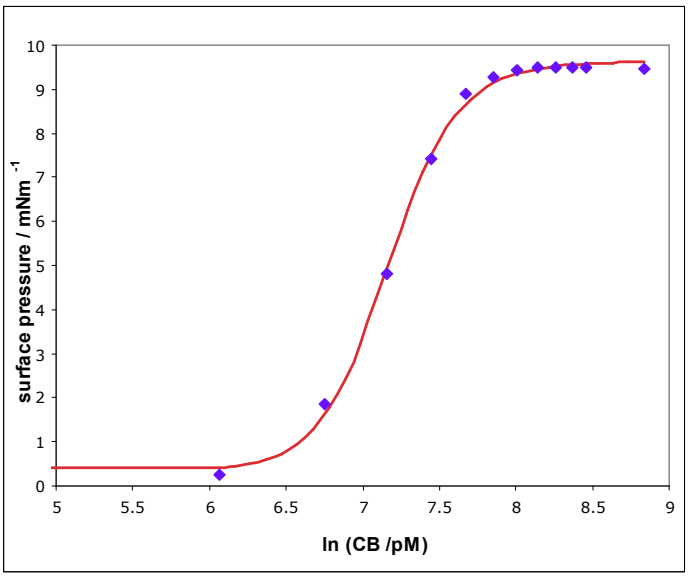

Figure 50 - Surface pressure as a function of protein concentration for hRSV-M-FITC additions, data was fit to equation 23

Parameter	hRSV-M	hRSV-M-FITC
$C_B^{\Pi/2}$	1902 pM	1292 pM
Π^{max}	8.85 dyn/cm	9.27 dyn/cm
Γ	6.78 pmol/cm^2	4.20 pmol/cm^2
Area per molecule	2447 Å^2	3956 Å^2

Table 13 - values for hRSV-M calculated from fitting in figure 50

While there have been some changes in the properties of hRSV-M-FITC, overall they are very small. A slight increase for affinity for the air-water interface is a surprising result though, since FITC is water soluble and would not have been expected to have this effect.

2.11 Giant Unilamellar Vesicles and confocal microscopy

Liposomes are often used as model systems for membrane binding. This is because they form bilayer systems with the same lipid structure as cell membranes and we can control their size and hence membrane curvature. However, these liposomes are can only be made to diameters ≤ 5 μm in size, while the average humans cell is between 10-100 μm. This leads to liposomes having a far greater membrane curvature than real cell membranes and makes them too small to view by microscopy methods. Especially when using membranes that exhibit multiple phase behaviours, it is important to be able to visualise different domains so if there are any specific interactions or localisation of proteins to the membrane we can see which domains were involved. To achieve this, we designed a method modified from Angelova *et. al.* to generate Giant Unilamellar Vesicles (GUVs).[152] GUVs are much like liposomes, but show a diameter distribution of 1-300 μm, and are therefore a much better mimic of a cell's plasma membrane due to similar curvature. Along with this, the increased size means that it is now possible to visualise the vesicles using phase contrast microscopy and, if appropriately labelled, by fluorescent microscopy.

GUVs can be formed through several different methods. While a quick method is to form them out of a surfactant / water mixture, this leaves the surfactant contaminating your experiments, and is prone to producing multi lamellar structures. [153, 154] An alternative electroformation method was chosen since it has been shown to generate

very uniform GUVs and reduce the number of Multi Lamellar Vesicles (MLVs), while still being relatively easy to carry out.[153] This is modification of a simple hydration method, where a dried lipid film is slowly hydrated causing the lipids to slowly bud off the surface and form liposomes. This is modified by the application of an alternating electric current, which is believed to help overcome the van der Waals forces that otherwise hold the lipids as a layer on the glass.

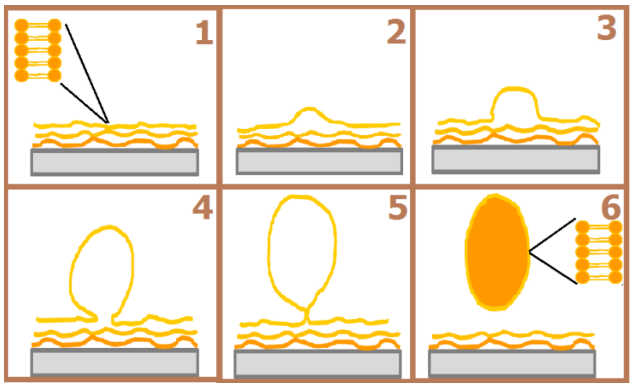

Figure 51 - Schematic of lipid hydration / electroformation of GUVs. ©Creative Commons

This method does have some drawbacks, for example it is unable to form GUVs with a high content of charged lipids, but was suitable for these experiments. For the formation of GUVs by this method, 1-10 µg of lipids are first dried onto conductive indium tin oxide (ITO) coated slides. A well is created between two slides using a nitrile O-ring, and is filled with a weakly buffered sucrose solution (5 mM sodium phosphate, 300 mM sucrose, pH 7.4). A weak buffer must be used since it has been found that high salt conditions inhibit GUV formation.[152, 155] An electric current is then applied across the well. The voltage is increased from 0.1V to 1.2V at 10 Hz in a sine waveform over ten minutes, and then maintained at 1.2V for 3 additional hours. This results in GUV formation; however most will still be attached to the glass surface. A final step of 1.2V at 5 Hz in a square waveform for 20 minutes is used to detach the GUVs. This creates GUVs with an internal solution of sucrose. While this process is suitable for single component lipids with a T_m below room temperature, lipids with a higher T_m and mixed systems that phase separate require that the sample is heated during the procedure. For this, an oven was constructed, and the GUV apparatus was heated to 70°C for the duration of the electroformation, followed by slowly cooling to room temperature. This slow cooling process is required so that any phase separation may develop correctly, cooling too quickly has been shown to stop phase development.[156]

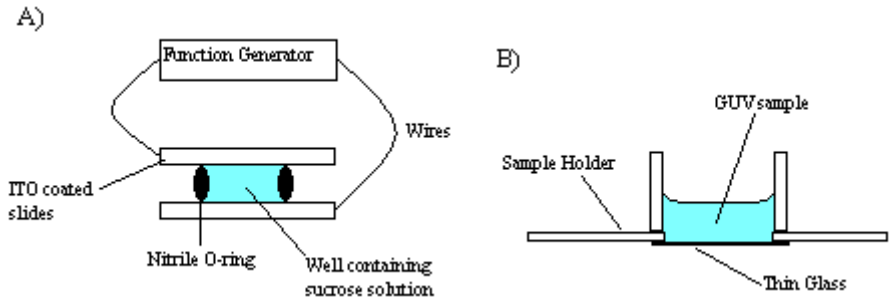

Figure 52 - A = schematic of GUV formation chamber, B = Sample holder for GUV viewing by microscopy.

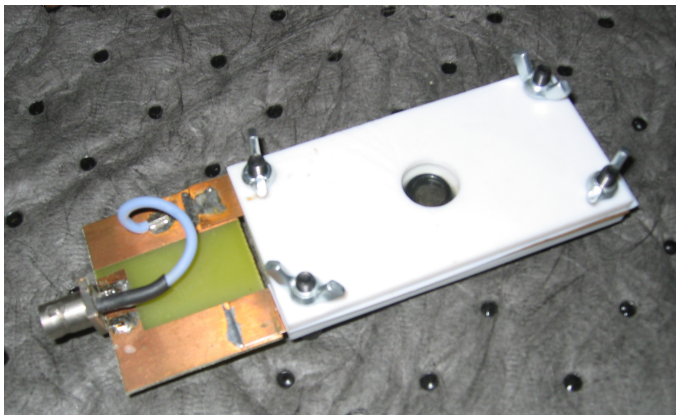

Figure 53 - Photograph of assembled GUV electroformation apparatus

Once the GUVs have been formed, the sample has to be prepared for observation by microscopy. The sample holder consists of a glass cover slip (passivated with bovine serum albumin) attached to a small Teflon lined well, so the sample can be loaded into the well and observed from underneath by the microscope. The well is first filled with a buffered glucose solution that is matched in osmotic strength by the sucrose solution used for forming the GUVs (5 mM Sodium Phosphate, ~280 mM Glucose, pH 7.4). 5µl of the GUVs can then be added to this solution to be viewed. The difference in density of glucose and sucrose solutions means that the GUVs will sink to the bottom of the well, resting on the glass surface. Experiments with hRSV-M instead had the osmotic strength of the glucose and sucrose solutions matched with a 5 µM hRSV-M solution in 5 mM Sodium phosphate (pH 7.4). This was then added to the sample well as required.

Confocal fluorescent microscopy was used to visualise the GUVs. This form of microscopy uses a pinhole in the apparatus in order to block any light from outside the focal point. This means that thin sections (< 5 um) through the sample can be viewed. This is very useful for viewing GUVs since they are spherical, and so this

technique allows us to view a cross section through the vesicle. In order to visualise the GUVs and hRSV-M under the microscope they had to be fluorescently tagged. hRSV-M-FITC was used for protein additions, produced as detailed in section 2.10. For labelling the GUVs a rhodamine B labelled lipid, 1,2-dipalmitoyl-sn-glycero-3-phosphoethanolamine-N-(lissamine rhodamine B sulfonyl) ammonium salt, was used (henceforth called Rh-PE). This fluoresces in the red region and so is a good counterpart to using a green labelled protein. It has also been shown to partition to different phases of lipid bilayers with different affinities. It shows a preference for L_d phases, and so we can use this lipid to distinguish different phases in a phase separated GUV, such as those produced from DOPC/Sphingomyelin/Cholesterol (1:1:1 molar). For experiments without protein, a green labelled lipid 1,2-diphytanoyl-sn-glycero-3-phosphoethanolamine-N-(7-nitro-2-1,3-benzoxadiazol-4-yl) ammonium salt, (henceforth called NBD-PE) was also used to visualise the whole GUV. This lipid does not show any preference for phase partitioning.[157] Fluorescently labelled lipids were used in such low concentrations (0.1 mol%), that their effect on membrane properties would be negligible.

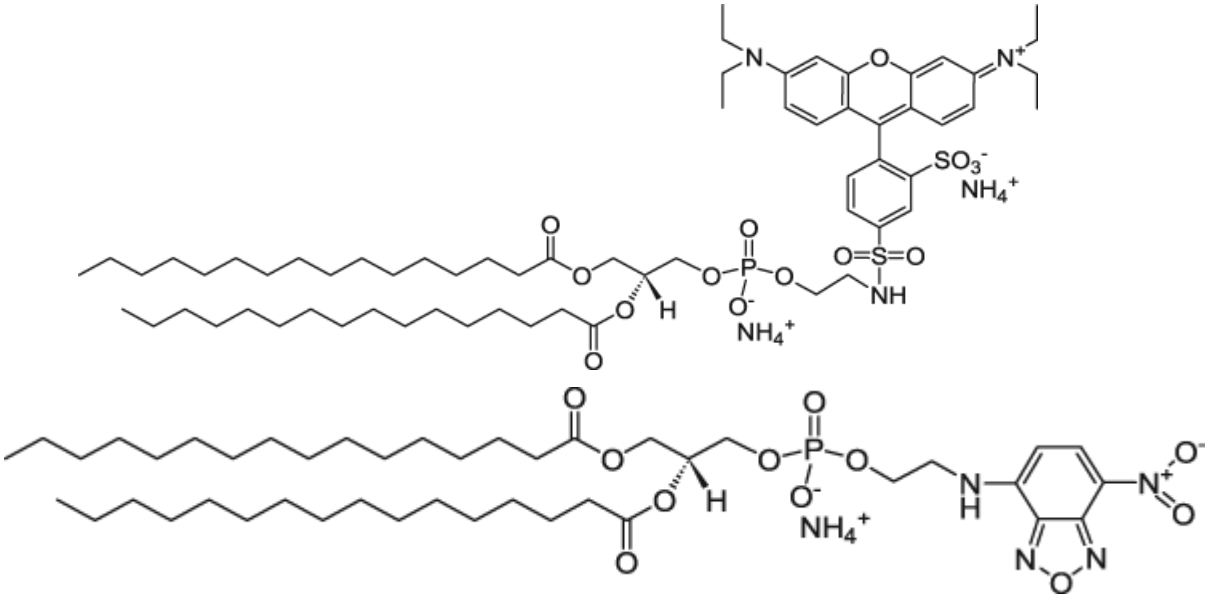

Figure 54 – Top: Structure of 1,2-dipalmitoyl-sn-glycero-3-phosphoethanolamine-N-(lissamine rhodamine B sulfonyl) ammonium salt. Bottom Structure of 1,2-diphytanoyl-sn-glycero-3-phosphoethanolamine-N-(7-nitro-2-1,3-benzoxadiazol-4-yl) ammonium salt.

The confocal microscope used for image collection was either a Biorad Microradience 2000 or a Zeiss 510 Meta. Rh-PE was excited using a 543.365 nm GreenNe Laser and fluorescence detected with a photomultiplier tube with an E570nm Longpass filter. NBD-PE and hRSV-M-FITC were excited using a 488.0 nm Argon Laser and

fluorescence detected with a photomultiplier tube with a HQ530/60 nm Bandpass filter. Images presented here are a representative selection from many taken in each sample, and have been given false colour relative to their channel.

2.11.1 Lipid only GUVs

GUVs consisting of DOPC only and DOPC/Sphingomyelin/Cholesterol (1:1:1 molar) were first produced to check the quality of produced GUVs and if phase separation was being achieved.

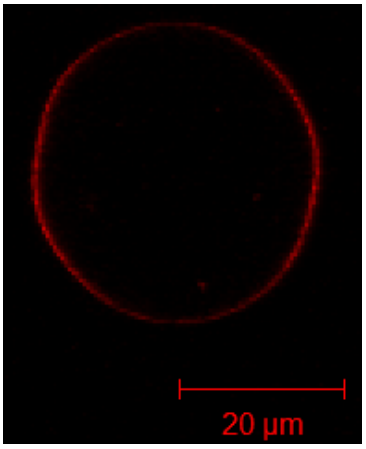

Figure 55 - Confocal image of a DOPC GUV with Rh-PE, red channel

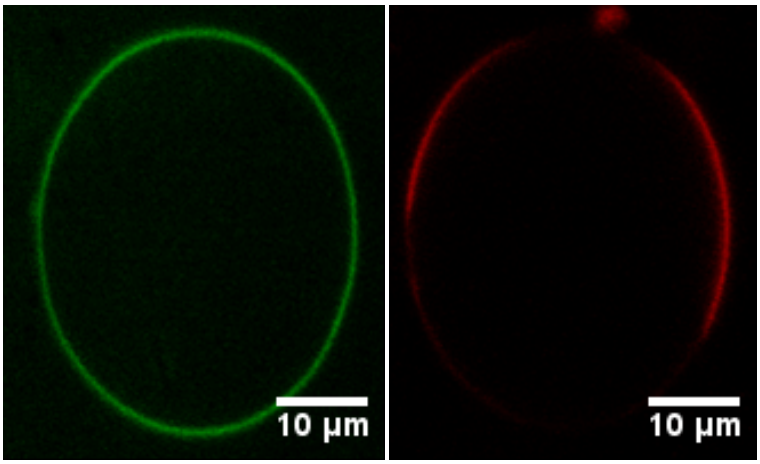

Figure 56 - Confocal image of DOPC/SM/Chol (1:1:1) GUV with NBD-PE and Rh-PE. Left = Green channel, Right = Red channel

These images show that the GUVs produced were unilamellar and of a suitably large size. In particular, the DOPC/SM/Chol mixture is shown to phase separate well, with the Rh-PE lipid partitioning into the disordered phase.

2.11.2 GUVs with hRSV-M-FITC added

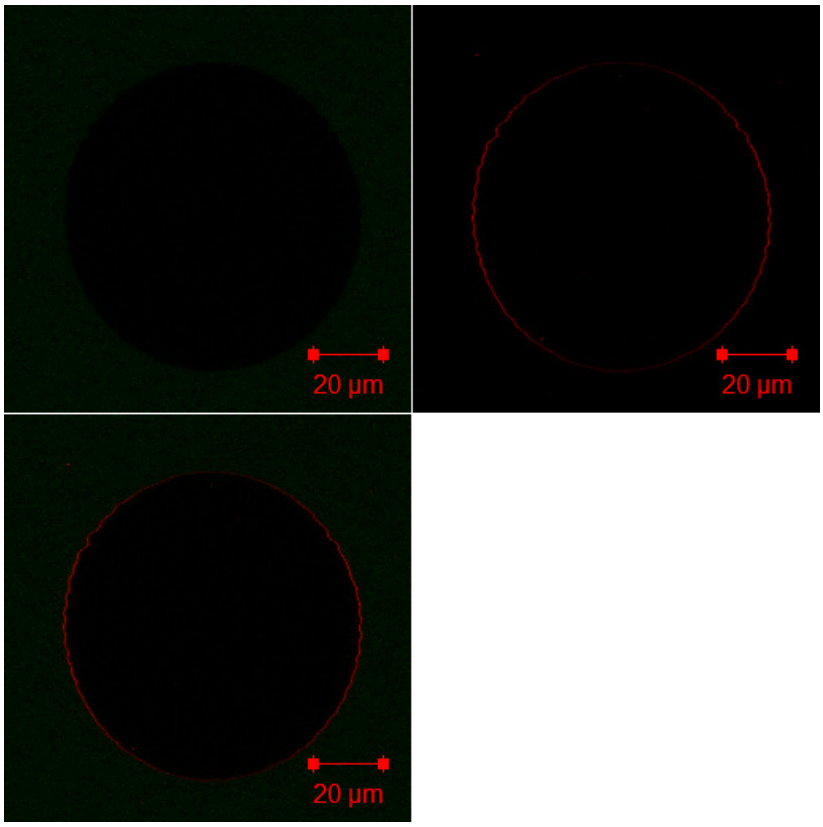

Figure 57 - Confocal image of DOPC GUV with 5µM hRSV-M-FITC. Top left = Green channel (M-FITC), Top right = Red channel (Rh-PE), Bottom Left = Merged

For GUVs of DOPC, no interaction of HRSV-M with the GUV could be observed. It can also be seen that hRSV-M-FITC is staying outside the GUV and is unable to cross the bilayer, as seen by the lack of green fluorescence inside the GUV.

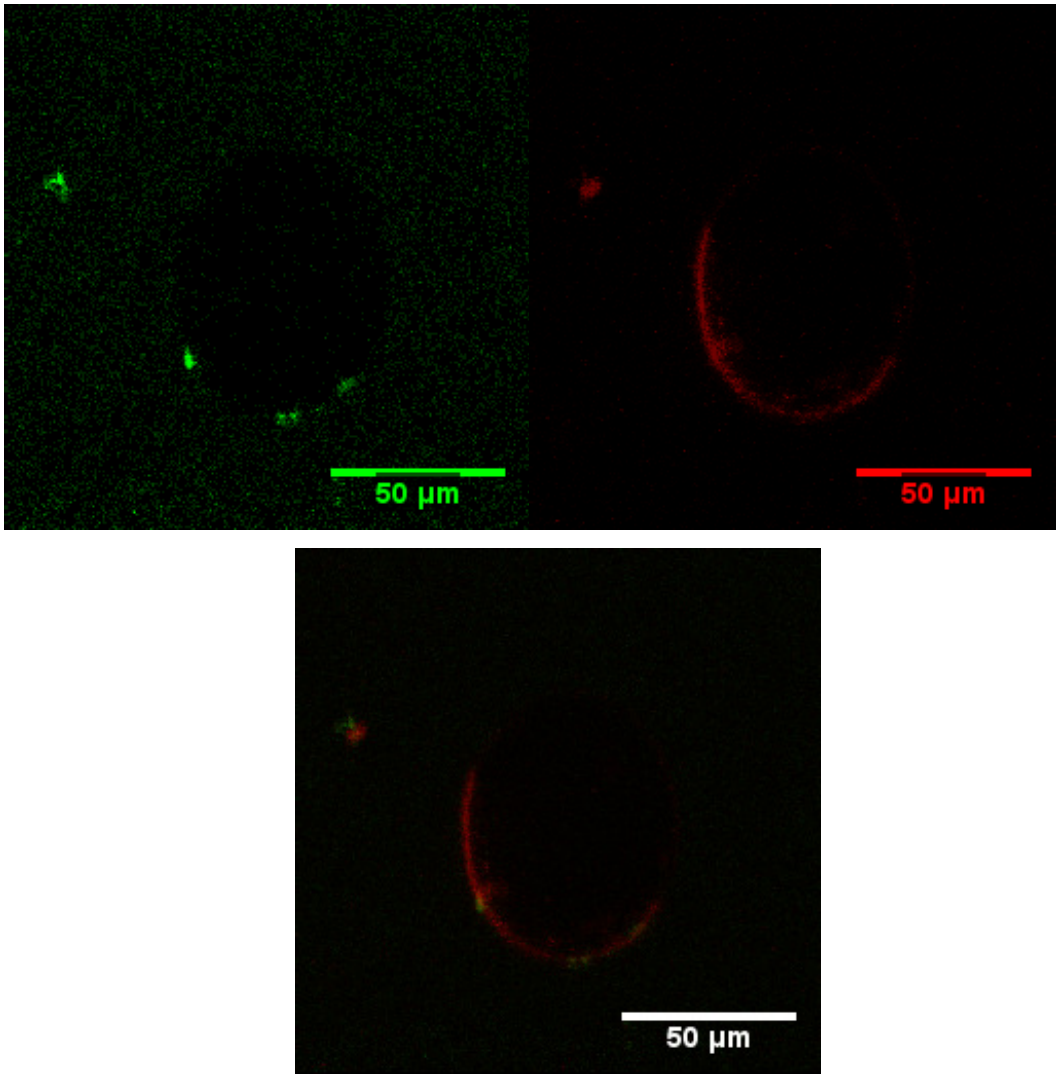

Figure 58 - Confocal image of DOPC/SM/CHOL (1:1:1) GUV with 5 µM hRSV-M-FITC. Top left = Green channel (M-FITC), Top right = Red channel (Rh-PE), Bottom = Merged

GUVs consisting of DOPC/SM/Chol (1:1:1 molar) in figure 59 showed some interaction with hRSV-M. Small spots of hRSV-M-FITC could be seen on the surface of the GUVs, but only on the rhodamine labelled L_d phase. The spots are slightly larger than would be expected for a single layer of hRSV-M-FITC, suggesting that these may be small aggregates that are interacting with the DOPC/Chol phase. However overall little interaction was seen.

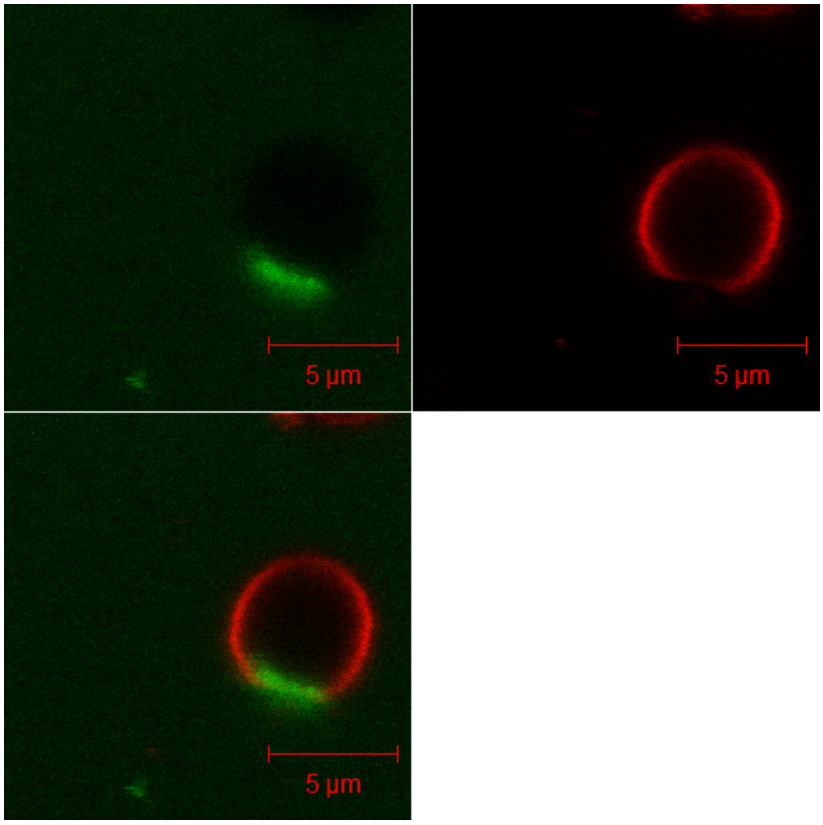

Figure 59 - Confocal image of DOPC/DPPS (4:1) GUV with 5µM hRSV-M-FITC. Top left = Green channel (M-FITC), Top right = Red channel (Rh-PE), Bottom Left = Merged

GUVs of DOPC/DPPS (4:1 w/w) showed a strong interaction with hRSV-M-FITC as seen in figure 59. The GUVs were not phase separated in the absence of protein, however upon addition of hRSV-M patches could be seen on the surface where hRSV-M had bound and the Rh-PE dye had been mostly excluded. This suggests that these areas have changed phase from a disordered to a more ordered phase due to hRSV-M binding the lipids. It is possible that hRSV-M is clustering the DPPS component of the membrane together, creating a raft rich in DPPS.

In order to investigate this behaviour, two further mixtures of lipids were used. The first was DOPC/DPPC/Chol/DPPS (1:1:1:1 molar). This mixture might be expected to phase separate naturally, into a DOPC L_d phase and a DPPC/Chol/DPPS L_o phase.[158]

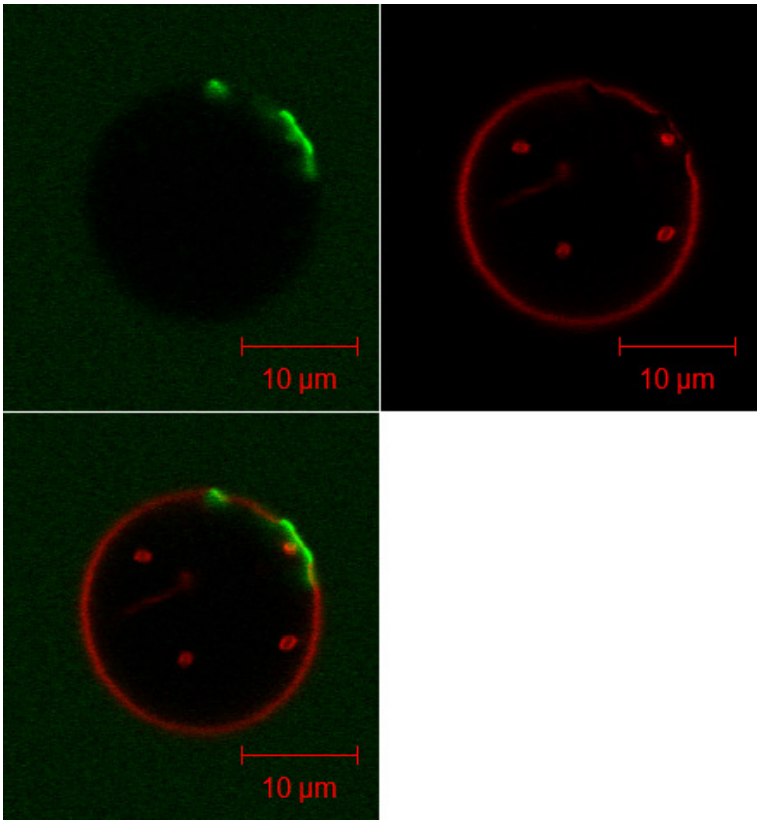

Figure 60 - Confocal image of DOPC/DPPC/Chol/DPPS (1:1:1:1) GUV with 5µM hRSV-M-FITC. Top left = Green channel (M-FITC), Top right = Red channel (Rh-PE), Bottom Left = Merged

Unfortunately the GUVs were not seen to naturally phase separate. This may be due to the relatively decreased amount of cholesterol compared with a DOPC/DPPC/Chol (1:1:1 molar) mixture. However the GUVs did still show the same behaviour with hRSV-M as the DOPC/DPPS (4:1) GUVs, with the binding of hRSV-M resulting in an exclusion of the Rh-PE dye seen in figure 60.

The final mixture tested was for GUVs consisting of POPS/SM/Chol (1:1:1 molar). This was devised to see what effect having the phosphatidylserine component in a largely L_o phase would be.[159] Due to changes observed over time, two figures are provided below showing changes.

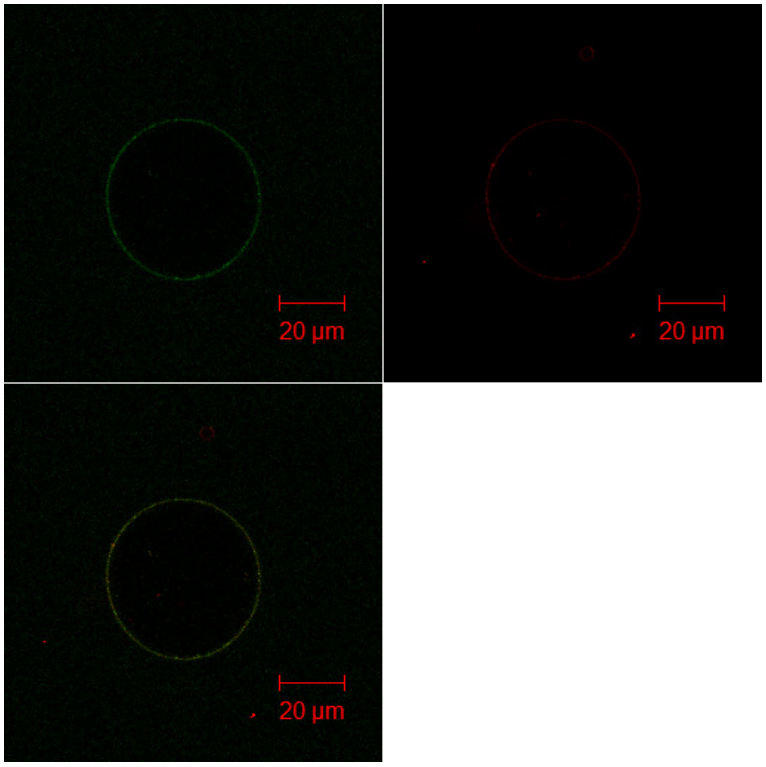

Figure 61 - Confocal image of POPS/SM/Chol (1:1:1) GUV with 5µM hRSV-M-FITC, at Time = 2 minutes. Top left = Green channel (M-FITC), Top right = Red channel (Rh-PE), Bottom Left = Merged

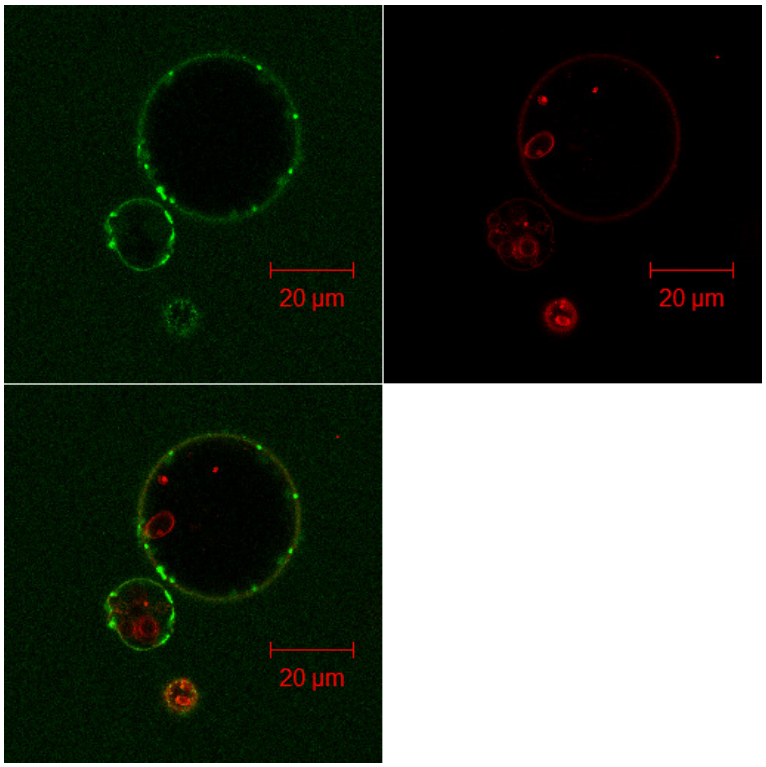

Figure 62 - Confocal image of POPS/SM/Chol (1:1:1) GUV with 5µM hRSV-M-FITC, at Time = 10 minutes. Top left = Green channel (M-FITC), Top right = Red channel (Rh-PE), Bottom Left = Merged

Within the first few minutes of the experiment, hRSV-M-FITC can be seen binding over the whole surface of the GUV. This strong interaction may be due to the increased ratio of phosphatidylserine present in this lipid mixture (33%). However, after a period of ten minutes, its was observed that small concentrated spots of hRSV-M-FITC were appearing over the surface, as seen in figure 62. These were typically <1 μm in size, and appeared to be randomly distributed. These may possibly be the formation of oligomers of hRSV-M at the surface following lipid binding.

2.12 Lipid Nanodiscs

While the previously used methods for studying protein-lipid interactions give a great deal of information, they all have several drawbacks in common. They all involved a large lipid surface, and studying the bulk interactions between this and the protein of interest. In order to study the protein-lipid interaction at a smaller scale, lipid nanodiscs were used.

A class of proteins, the plasma lipoproteins, were found to bind small liposomes in the blood as a method of lipid transport. When extracted it was found that with synthetic lipids they would form small disc structures, consisting of a ring of protein surrounding a central lipid bilayer.[160] These proteins were thus used as a basis for creating synthetic proteins with similar properties. The predominately α-helical C-domain of apolipoprotein A-1 was used to create these new proteins, called membrane scaffold proteins (MSP). These consist of repeating units of α-helices, the number of which can be tailored in order to create different nanodiscs of differing sizes, approximately 9-13 nm in diameter.[161] The two units of MSP wrap themselves around the hydrophobic core of the bilayer, protecting it from the bulk water and thus keeping a stable bilayer.[162]

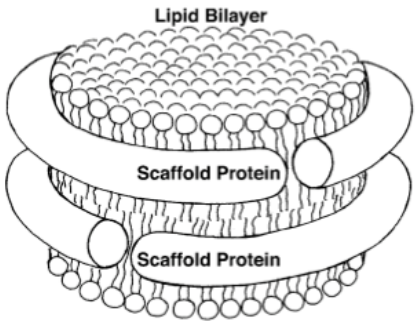

Figure 63 - Structure of a Lipid Nanodisc formed by MSP. ©University of Illinois

Nanodiscs are bilayer systems with no membrane curvature, and so can be a better model of membranes than experiments on monolayers and liposomes. These nanodiscs are most often used to study transmembrane proteins, which are imbedded in the nanodisc for individual study.[163] However they are also useful for studying peripheral membrane binding proteins. Given their small size, we can expect only a few proteins to be able to bind to each face of the nanodisc, and thus it is possible to study individual molecules of hRSV-M binding. This was primarily attempted via dynamic light scanning and electron microscopy.

The MSP protein used was MSP1E3D1, which is expected to generate approximately 12.1 nm diameter bilayer discs and an approximately 9 nm thick lipid bilayer. To produce the nanodiscs, MSP1E3D1 was first produced by recombinant means. Briefly, a plasmid containing a His-tagged MSP1E3D1 construct was transformed into *E.Coli* BL21 and expression induced with IPTG. After 3 hours growth the cells were harvested and lysed to release the protein. The resulting supernatant was then purified by immobilised metal affinity chromatography (IMAC) using Ni-NTA, and stored in a buffer of 20 mM Tris pH 7.4, 0.1 M NaCl, 0.5 mM EDTA.

For nanodisc formation, the lipids to be used (POPC/POPS 1:1 and POPS alone in the following experiments) are dried onto glass, and then rehydrated and solubilised using a solution of Sodium Cholate at twice the final lipid concentration (e.g. 50 mM Lipid : 100 mM Sodium Cholate), with vigorous mixing, hating and sonication. The suspended lipids are then mixed with MSPE3D1 in a specific ratio, some examples of which are given below. It is crucial this stoichiometry is used, since even small

changes will result in aggregates and other sized entities. The mixture was then incubated for one hour at the specified temperature.[162]

Lipid	Optimal Ratio for MSP1E3D1	Incubation temperature
DPPC	170:1	37 °C
DMPC	150:1	25 °C
POPC / POPS	130:1	4 °C

Table 14 - Incubation conditions to form lipid Nanodiscs

The resulting solution was then dialysed against a clean buffer in order to remove the Sodium Cholate. Doing so changes the lipid micelles into their final bilayer configuration surrounded by the matrix scaffold protein. The crude mixture of nanodiscs was finally purified by size exclusion chromatography on a HiLoad 16/600 Superdex 200 PG column (GE Healthcare), coupled to an inline Dynamic light scattering (DLS) machine (Zetasizer μV, Malvern). The DLS was attached to identify nanodiscs of the correct diameter as they came off the column.

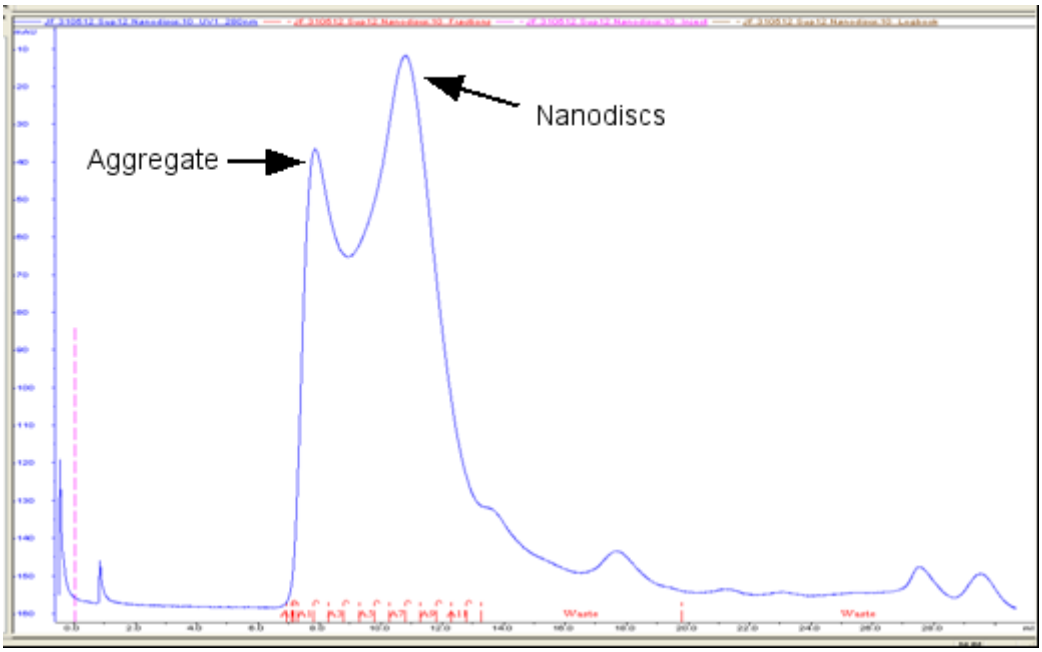

Figure 64 - FPLC UV 280 nm trace for POPS MSP1E3D1 nanodiscs eluting from a Superose 12 10/300 size exclusion column

2.13 Dynamic Light Scattering

In order to observe the nanodiscs and any binding of hRSV-M to their surface, Dynamic Light Scattering (DLS) measurements were used. When light hits particles that are smaller than its wavelength, it can undergo Rayleigh scattering, and a DLS machine is designed to detect this scattered light. When carried out on particles in solution, the signal returned will not be constant, since the particles moving due to Brownian motion. This motion is dependent on the size of the particle, and this can be quantified by the Stokes-Einstein equation:

$$D_h = \frac{k_B T}{3\pi\eta D_t}$$

Equation 25

Where D_h is the hydrodynamic radius of the particle, k_B is the Boltzmann constant, T is the temperature, η is the dynamic viscosity of the solution and D_t is the translational diffusion coefficient. In order to find D_t experimentally, the change in scattered light is measured over time, and an autocorrelation function is applied to it. This correlates the change in time between detected movements. This data can then be fit to an exponential decay of the form:

$$C = \exp(-2\Gamma\tau)$$

Equation 26

Where C is the autocorrelation function, τ is the decay time and Γ is defined by the equations:

$$\Gamma = D_t q^2$$

Equation 27

And:

$$q = (4\pi n/\lambda)\sin(\theta/2)$$

Equation 28

Where q is the scattering vector, n is the refractive index of the liquid, λ is the wavelength of the light, and θ is the scattering angle. This allows us to calculate D_t, and hence calculate the hydrodynamic radius from equation 25.

The aim of these experiments was to see if the size of the nanodiscs is seen to change when hRSV-M is added, indicating that it has bound to the surface creating a larger particle. The following experiments were carried out in 10µl cuvettes, with an IR laser at 830 nm wavelength, and the scattering detector at 90° to the sample, and the sample in a 20 mM Tris-HCl, 200mM NaCl buffer. Fitting data is shown for hRSV-M as an example.

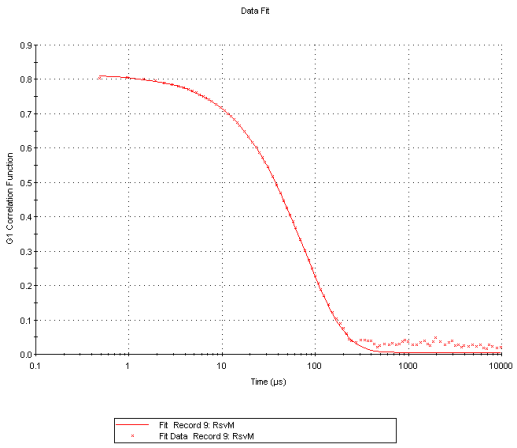

Figure 65 - Fitting of the DLS autocorrelation function for hRSV-M

		Size (d.nm):	% Intensity	Width (d.nm):
Z-Average (d.nm): 7.598	Peak 1:	7.843	100.0	1.347
PdI: 0.060	Peak 2:	0.000	0.0	0.000
Intercept: 0.815	Peak 3:	0.000	0.0	0.000
Result quality : Good				

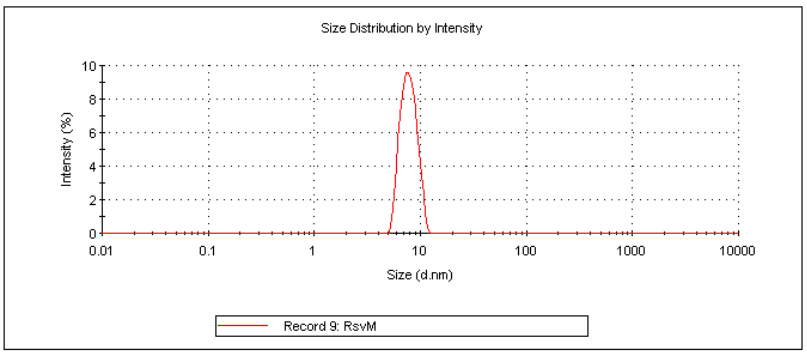

Figure 66 - DLS data for hRSV-M, showing particle size distribution and calculated values

Sample	Hydrodynamic particle size (diameter. nm)	Peak width (diameter. nm)
hRSV-M	7.84	1.34

Table 15 - calculated parameters for hRSV-M from DLS

The hydrodynamic diameter of hRSV-M appears to be quite large compared with the expected size from the protein crystal structure.[39] This coupled with the quite wide peak width suggest that hRSV-M is conformationally flexible in solution, likely due to mobility of the C-terminus relative to the N-terminus.

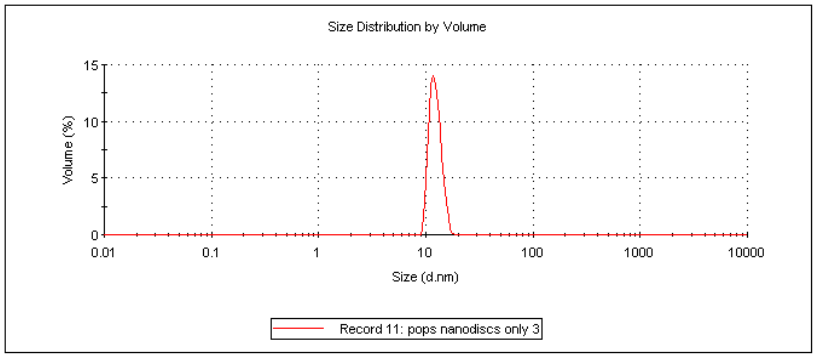

Figure 67 - Figure 51 - DLS data for POPS Nanodiscs, showing particle size distribution

Sample	Hydrodynamic particle size (diameter. nm)	Peak width (diameter. nm)
POPS Nanodiscs	12.29	1.55

Table 16 - calculated parameters for POPS MSPE3D1 nanodiscs from DLS

The nanodiscs correspond to the expected size of 12.1 nm.[162] The peak diameter of 1.5 nm may suggest that the nanodiscs vary in size slightly, however this likely caused by their disc-shape (approx 9nm thick, 12.1nm wide).

hRSV-M was then mixed with POPS nanodiscs in increasing ratios and the particle size recorded by DLS. The concentration of nanodiscs was 14 µM, and hRSV-M was added in increments of 2 molar equivalents, due to the assumption that it will bind on both faces of the nanodisc. An example of the size determination is shown for a hRSV-M to Nanodisc ratio of 10:1, and other ratios are summarised below.

		Size (d.nm):	% Volume	Width (d.nm):
Z-Average (d.nm): 27.44	Peak 1:	15.32	99.9	2.530
PdI: 0.470	Peak 2:	126.0	0.1	36.27
Intercept: 0.945	Peak 3:	0.000	0.0	0.000
Result quality : Good				

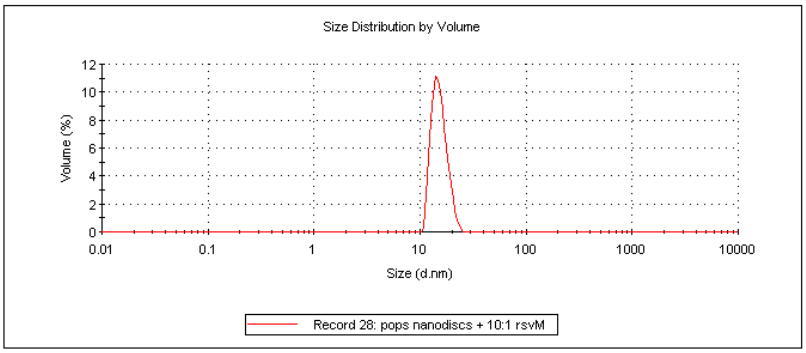

Figure 68 - DLS data for hRSV-M added to POPC annodiscs at a 10:1 ratio.

Ratio hRSV-M to nanodiscs	Hydrodynamic particle size (diameter. nm)	Peak width (diameter. nm)
POPS Nanodiscs only	12.29	1.55
2 : 1	13.01	1.87
4 : 1	13.51	2.02
6 : 1	14.93	2.43
8 : 1	14.92	2.23
10 : 1	15.32	2.53
12 : 1	15.40	1.91

Table 17 - Particle size from DLS for varying rations of hRSV-M added to POPC nanodiscs

The data shows that as increasing amounts of hRSV-M are added to the nanodiscs the hydrodynamic radius of the detected particles increases, with a maximum being reached of 15.4 nm at ration of 12 to 1. This suggests that hRSV-M is binding the nanodiscs. Although the change in hydrodynamic diameter is not very great, 3.03 nm at maximum, this can be interpreted as hRSV-M forming a more condensed structure at the bilayer interface instead of the loose conformation seen in solution. This combined with the nanodisc's natural disc shape mean that any change in the hydrodynamic distance perpendicular to the bilayer will be less visible by this

method. It is also possible that unbound hRSV-M and nanodiscs are bringing the average particle size down.

2.14 Cryo-electron Microscopy

Thanks are given to Dr David Bhella and group at the University of Glasgow Centre for Virus Research for carrying out the microscopy.

While nanodiscs are too small to be seen by conventional light microscopy, they can be viewed by electron microscopy. Transmission electron microscopy is used since the wavelength of electrons is much smaller than visible light. This allows images of individual protein to be taken, or in this case of single nanodiscs. Usually, the samples are stained with heavy atoms in order to increase the contrast on a fixed substrate grid, however in this experiment Cryo-EM was used. This freezes the sample in liquid ethane and takes a thin section through the sample before being mounted in the electron beam. By keeping the temperature low, the sample can then survive inside the beam, and so the need for a mounting substrate or contrast agent is removed. Flash freezing the sample also means it is viewed in its native state, unlike techniques such as x-ray crystallography. The end goal of this experiment was to collect many images of nanodiscs with hRSV-M in order to build up an electron density map. This can then be fitted with the x-ray structure of hRSV-M to see how it has bound to the lipid bilayer.[164]

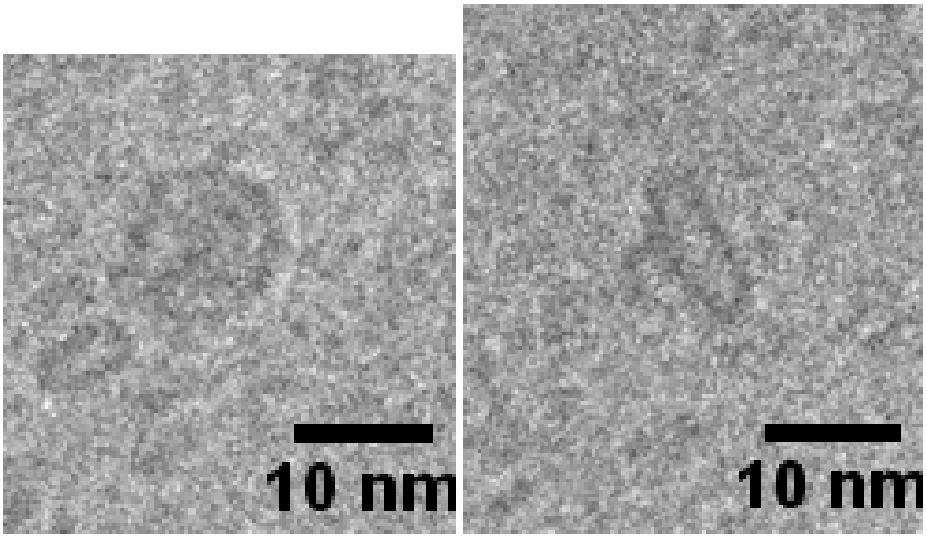

Figure 69 - Cryo EM images of POPC/POPS nanodiscs with hRSV-M (1:1 molar ratio). Left = Nanodisc from top, Right = Nanodisc on its side.

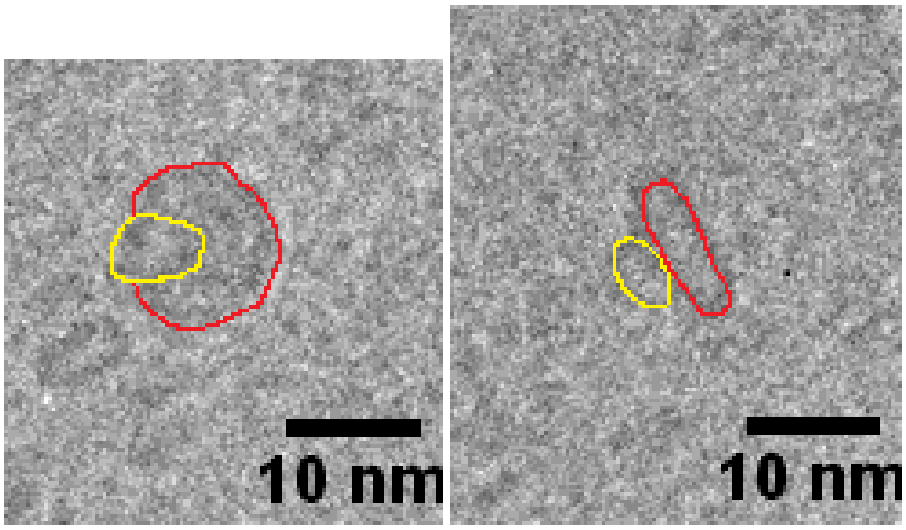

Figure 70 - Cryo EM images of POPC/POPS nanodiscs highlighted in Red with possible hRSV-M highlighted in Yellow. Left = Nanodisc from top, Right = Nanodisc on its side.

While nanodiscs could be easily seen in the images, the presence of hRSV-M was much more difficult to ascertain. Small particles could be seen attached to the lipid surface of some nanodiscs, however they were ill defined and many nanodiscs showed no features. They are approximately the size that would be expected for hRSV-M, being 6 nm in diameter when hRSV-M is expected to have a hydrodynamic diameter of 7.84 nm from DLS measurements and X-ray structure.[39] The presence of these particles does fit quite well with DLS data previously shown for hRSV-M binding nanodiscs (section 2.13), with only a small overall increase in size observed. Unfortunately, it was determined that the nanodisc sample was too polydisperse for an

electron map to be created (possibly due to sample degradation in transport). This experiment therefore remains unresolved.

3 Results - Influenza A M1

3.1 Purification and Protein Stability

The Matrix protein (Inf-M1) from Influenza A was the other target of this project. The full length (252 a.a.) M1 gene was cloned using PCR of genomic DNA from Influenza A (Strain A/PR/8/34) with the following primers:

Forward Primer: CACCCCGAATTCACCATGAGTCTTCTAACCGAGGT

Reverse Primer: CGACGGCCGCTCGAGACTTGAACCGTTGCATC

The forward and reverse primers contained restriction sites for EcoRI and XhoI respectively and these were used to clone the gene into the multiple cloning site of the vector pGEX-6P-1 (GE Healthcare). This vector was used because it provides a method of expressing the protein with a Glutathione-S-Transferase tag attached, which can then be used to purify the protein by its affinity to glutathione (Inf-M1-GST). This vector also allows proteolytic cleavage of the GST tag, so allowing the native, un-tagged protein to be retrieved after purification. Cloning success was screened using colony PCR and DNA sequencing.

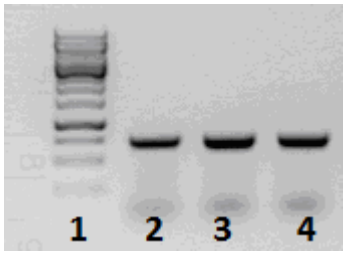

Figure 71 - Colony PCR of pGEX-6P-1-M1 containing *E.Coli* colonies. Lane 1 = Generuler 1Kb ladder, Lanes 2-3 = Colonies of Transformed *E.Coli*

Sequencing of the cloned plasmid showed that while the N-terminus was correct, attached to the GST fusion protein, at the C terminus there were 6 additional amino acids added to the sequence due to the cloning process used. However it was decided to continue with this clone.

GPLGSPEFTMSLLTEVETYVLSIIPSGPLKAEIAQRLEDVFAGKNTDLEVLM
EWLKTRPILSPLTKGILGFVFTLTVPSERGLQRRRFVQNALNGNGDPNNMDKAVKLY
RKLKREITFHGAKEISLSYSAGALASCMGLIYNRMGAVTTEVAFGLVCATCEQIADS
QHRSHRQMVTTTNPLIRHENRMVLASTTAKAMEQMAGSSEQAAEAMEVASQARQMVQ
AMRTIGTHPSSSAGLKNDLLENLQAYQKRMGVQMQRFKSRAAAS

Molecular weight: 29322.8

Theoretical pI: 9.43

Table 18 - Sequencing results of Inf-M1 expressed from pGEX-6P-1-InfM1. Underlined residues are not natural for Inf-M1, sequence only shown from after GST clevage site

For expression of Inf-M1-GST, the plasmid was transformed into *E.Coli* Bl21 De3. Initial expressions using 1L culture flasks in LB media showed little expression, possibly due to a toxic effect of Inf-M1 on *E.Coli*. A scaled up protocol using a 2L bioreactor was therefore used to increase cell density.[165] The transformed *E.Coli* were grown in 2L ZYM-5052 auto induction media[166] at 37°C with a constant air supply for 5 hours, and then the temperature reduced to 20°C for a further 20 hours. The cells were then harvested, resuspended in a buffer of 50 mM sodium phosphate, 200 mM sodium chloride, pH7.4, and lysed by sonication. The resulting supernatant was purified by incubation with glutathione-sepharose beads (GE Healthcare), which were then washed thoroughly in clean buffer and one wash containing an additional 1M sodium chloride. Inf-M1-GST was then eluted from the resin using reduced glutathione. The reduced glutathione was removed by dialysis into clean buffer. The GST tag was then removed by treatment with PreScission® Protease overnight. The protease and the now free GST were removed by further incubation with Glutathione-Sepharose beads, and the supernatant containing Inf-M1 removed.

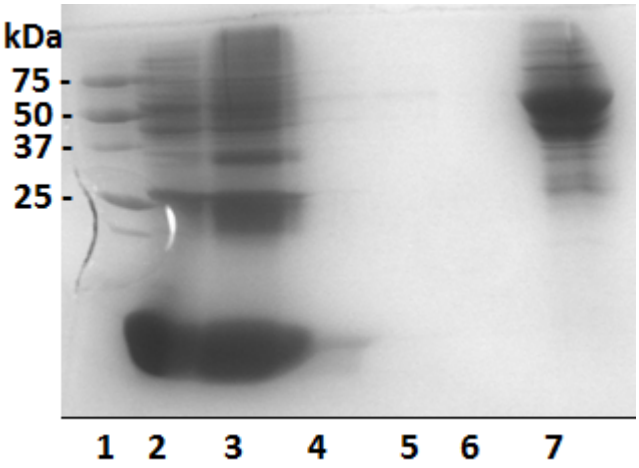

Figure 72 - SDS-Page gel of first step in Inf-M1 purification. Lane 1 = Protein markers, Lane 2 = Supernatant from lysed E.Coli, Lanes 3-6, Washes of Glutathione-Sepharose 4B beads, Lane 7 = Elution of Inf-M1-GST from Glutathione Beads

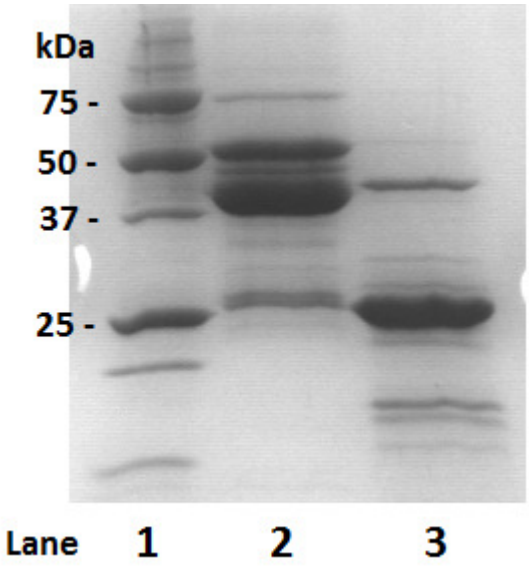

Figure 73 - SDS-Page gel of the cleavage of GST tag from Inf-M1. Lane 1= Protein markers, Lane 2 = Crude Inf-M1-GST, Lane 3 = Inf-M1 after cleavage and removal of GST

Following this first step of purification, the samples were still determined to contain too many contaminants for use in experiments. Several different methods for a second step purification were tested; however the one that produced the best results was size-exclusion chromatography. The protein was applied to a Superose 12 HR 10/30 (GE Healthcare) column and eluted into 50 mM sodium phosphate, 200 mM sodium chloride buffer. 0.5 ml fractions were collected, and screened by SDS-Page gel for the presence of Inf-M1.

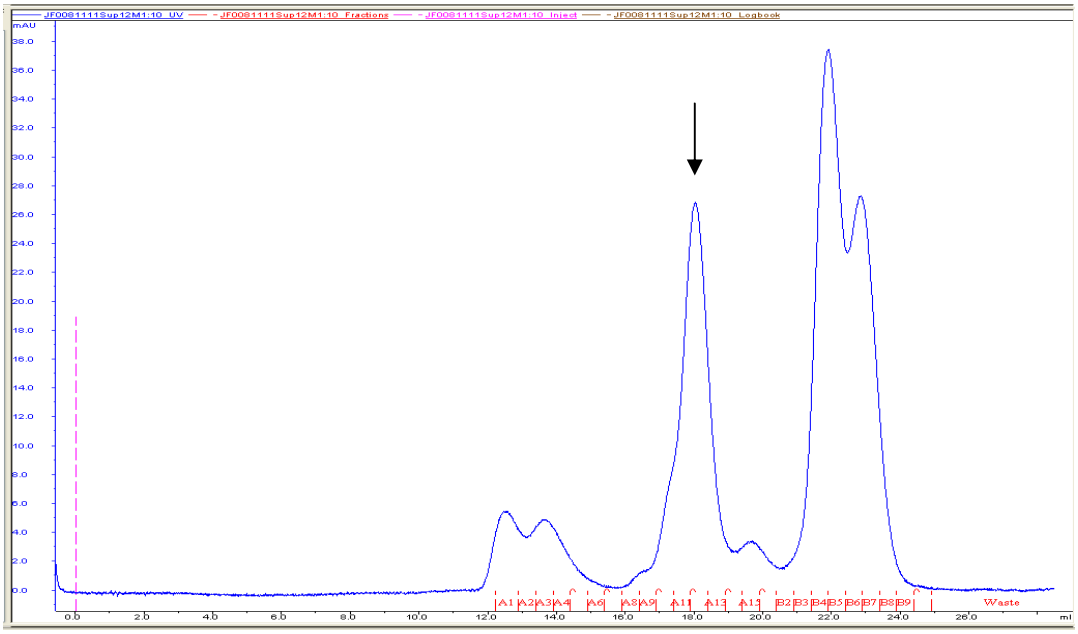

Figure 74 - FPLC UV absorbance (280 nm)trace of crude Inf-M1 on Superose 12 HR 10/30 column. Indicated peak = Inf-M1

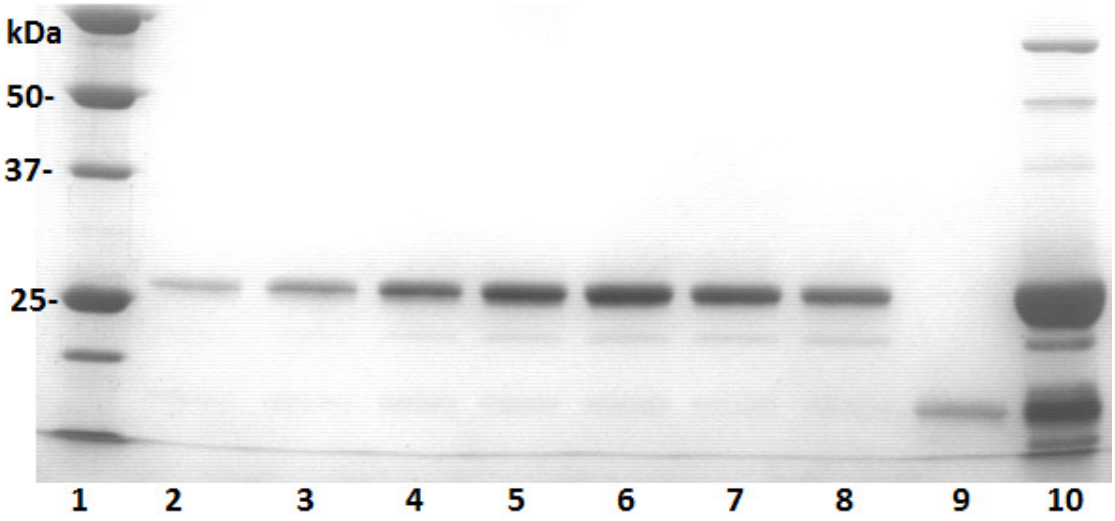

Figure 75 - SDS-Page gel showing fractions taken from size exclusion chromatography of Inf-M1. Lane = Protein Marker, Lanes 2-8 = FPLC fractions A8-A14, Lane 9 = fraction B5, Lane 10 = Inf-M1 before purification

The identity of the purified protein was confirmed by mass spectrometry, giving exactly the expected mass of 29322 Da.

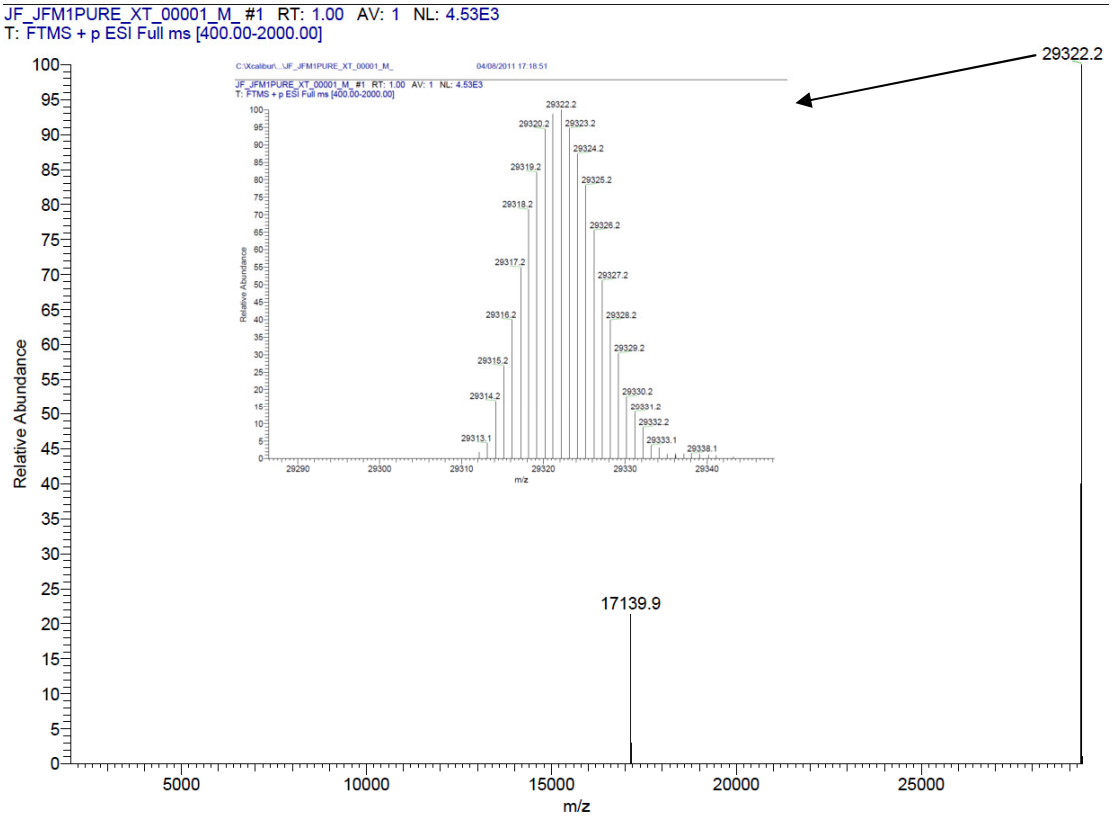

Figure 76 - Fourier Transform Mass Spectroscopy converted to neutral mass for a sample of Inf-M1. Insert = Expansion of the peak at 29322 Da

While the purification process gave a mostly pure protein (>98%), it can be seen in both the size exclusion chromatography and the mass spectrometry that smaller proteins can be seen at 17 kDa and smaller. It was further observed that these fragments became more prevalent over time as the protein was stored. The most likely reason for this is that the protein is degrading. While this behaviour had been observed with hRSV-M previously it occurred over a long time scale (>1 week), however with Inf-M1 this degradation can be observed very shortly after purification, as seen in figure 77. This fragmentation has been described previously, with the crystal structure for the N-terminus being produced after the fragmentation of the full length protein at amino acid residue 152.[66] While this fragmentation was undesirable, it was decided that samples were still suitable if used on the day of purification, and re-purified for use on following days.

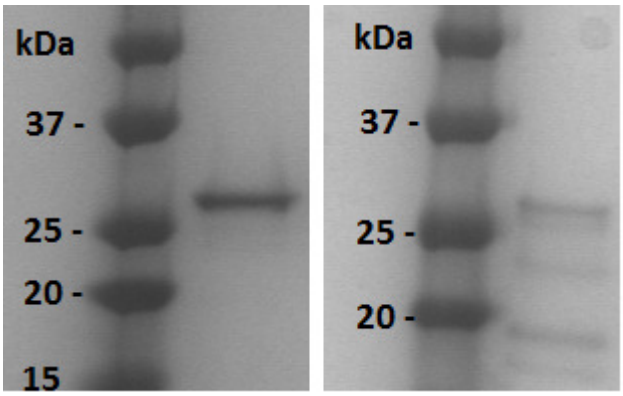

Figure 77 - SDS-Page gels of Inf-M1. Left, Immediately after purification. Right, After 5 days storage at 4°C.

3.2 Circular Dichroism and DLS

Following purification, the structure of the protein was checked by circular dichroism measurements, using the same method as described in section 2.5. This was done to ensure the protein was correctly folded, and for comparison with literature data. The Continll algorithm again gave the best fit to the data.

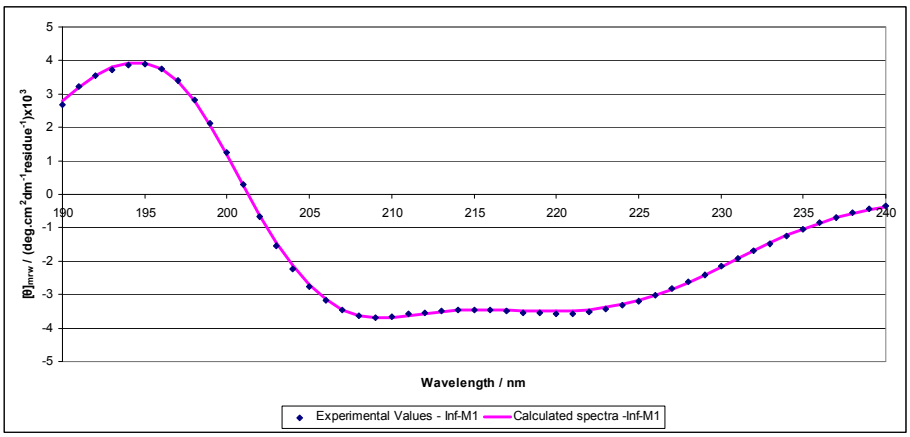

Figure 78 - Circular Dichroism spectra for Inf-M1

	Structural Feature (%)					
	α-Helix (regular)	α-Helix (distorted)	β-Sheet (regular)	β-Sheet (distorted)	Turn	Irregular
Inf-M1	20.0	17.7	8.3	6.3	20.9	26.8

Table 19 - Secondary structural characteristics of Inf-M1 calculated Continll algorithm

The data collected shows M1 to be mainly alpha helix or disordered. This corresponds to data in the literature which suggest that the N-terminus is main alpha helical (46%)[62] and the C-terminus is mainly disordered.[167]

Dynamic light scattering data was also collected for Inf-M1. The data given below show that M1 has a slightly larger diameter than would be expected for a purely spherical protein of the same mass (approx 3.1 nm).[168] This suggest that M1 is an elongated molecule, likely due to the mobility between the C and N-terminus. Alternatively it may indicate the Inf-M1 is forming a dimer in solution

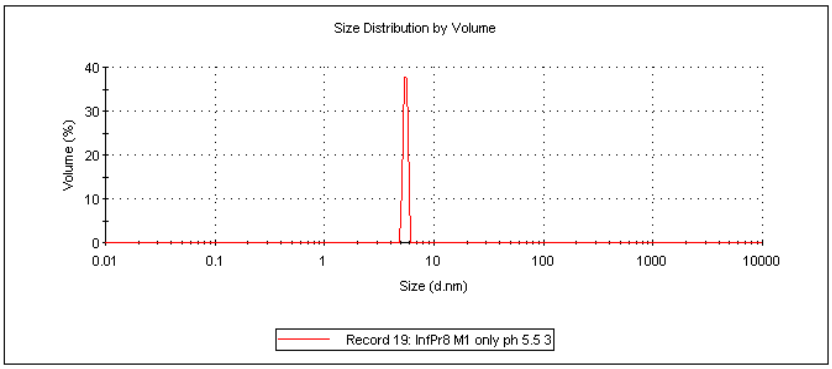

Figure 79 - Particle size distribution of Inf-M1 by DLS

Sample	Hydrodynamic particle size (diameter. nm)	Peak width (diameter. Nm)
Inf-M1	5.48	0.21

Table 20 - Particle size calculated from DLS

The small peak width indicates that the Inf-M1 molecules are likely in the same conformation in solution.

3.3 Differential Scanning Fluorimetry

In an attempt to find any conditions that may stop Inf-M1 from degrading as quickly, DSF analysis was carried out on it to identify binding partners. The same conditions and additives were used as for hRSV-M, as described in section 2.2. The protein was dialysed into 1mM Tris before usage. Only additives that caused a significant change in T_m are shown.

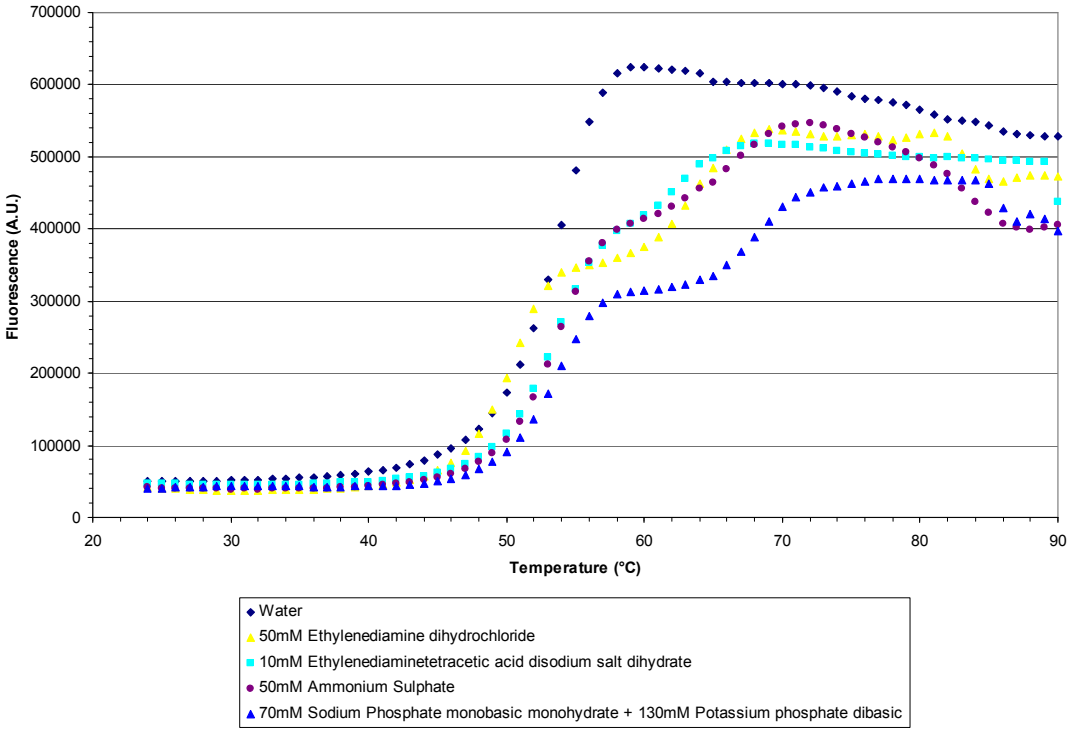

Table 21 - DSF data for Inf-M1 in 1mM Tris buffer pH 7.4

Additive	T_m1 (°C)	T_m2 (°C)
None (PBS buffer)	53.8	-
50mM Ethylenediamine dihydrochloride	50.5	63.6
10mM Ethylenediaminetetraacetic acid disodium salt dehydrate	53.7	62.6
50mM Ammonium Sulphate	53.9	65.9
70mM Sodium Phosphate monobasic monohydrate + 130mM Potassium phosphate dibasic	54.0	68.3

Table 22 - T_m values for Inf-M1 with additives used in DSF experiments

The addition of the compounds shown in the collected data resulted in a second Tm being identified. As the samples were heated, they first underwent a denaturation event with a T_m of around 53°C which was largely unchanged by the additives. However, while this was a single event for the protein alone, with the above additives a second denaturation event can be seen with a much higher T_m. One interpretation of this is that these two events correspond to the separate C- and N-terminuses of the protein denaturing separately. Given the apparent structural order in the N-terminus, it seems likely that the change results from the C-terminus becoming more ordered.[118] The additives causing this effect being either metal chelators (Ethylenediamine,

EDTA) or ions that may precipitate metals (phosphate, sulphate) suggest that the increase in stability may be caused by the removal of a metal ion. Alternatively, it has been shown that some proteins contain phosphate/sulphate binding sites which can greatly increase their stability to denaturation though an increase in the solution surface tension of the protein.[169-171] The exact cause of this change in stability cannot be determined from these experiments, but it was decided henceforth to use sodium phosphate based buffers for work on this protein. Unfortunately this change in buffer conditions made no difference to the protein degradation problems, indicating they have a different cause.

3.4 Langmuir Isotherms and Brewster angle microscopy

A plan was made to conduct Langmuir isotherm experiments in much the same way as ha been done for hRSV-M. The first experiment to be done was the effect of Inf-M1 onto the air-water interface. However, when the protein was added it was found that the time taken for it to equilibrate was extremely long, far greater than would make it reasonable to perform isotherms on monolayers at equilibrium. The pressure could not even be seen to change until a large amount of protein had been added.

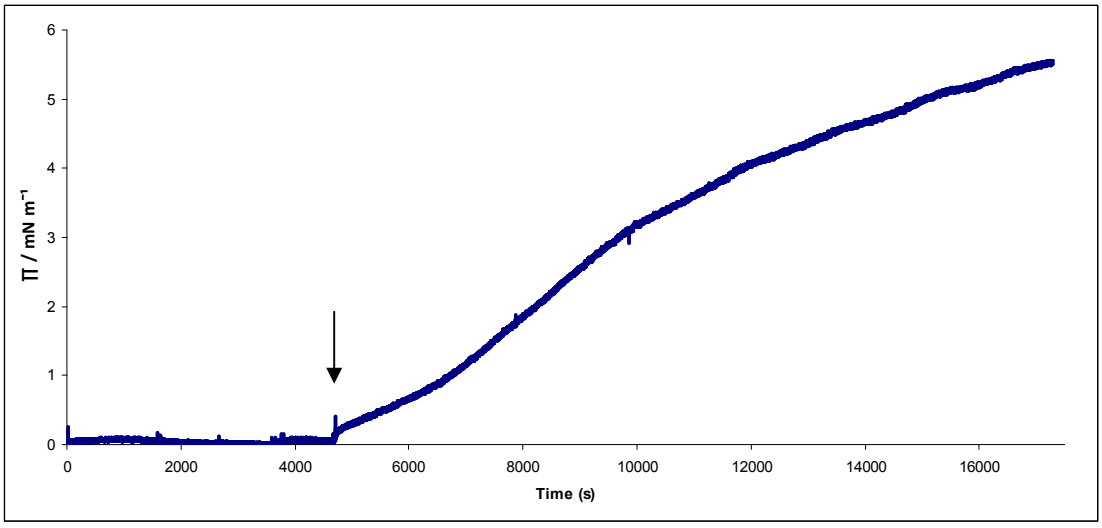

Figure 80 - Time/Pressure plot for additions of Inf-M1 to a clean PBS subphase. At T=0, Inf-M1 concentration was 1.49 nM, at arrow indicated more was added to make 25.26 nM total.

While this made characterisation of Inf-M1 impossible by this method, Brewster angle microscopy images could still be obtained to view any structures formed on the surface during this slow process.

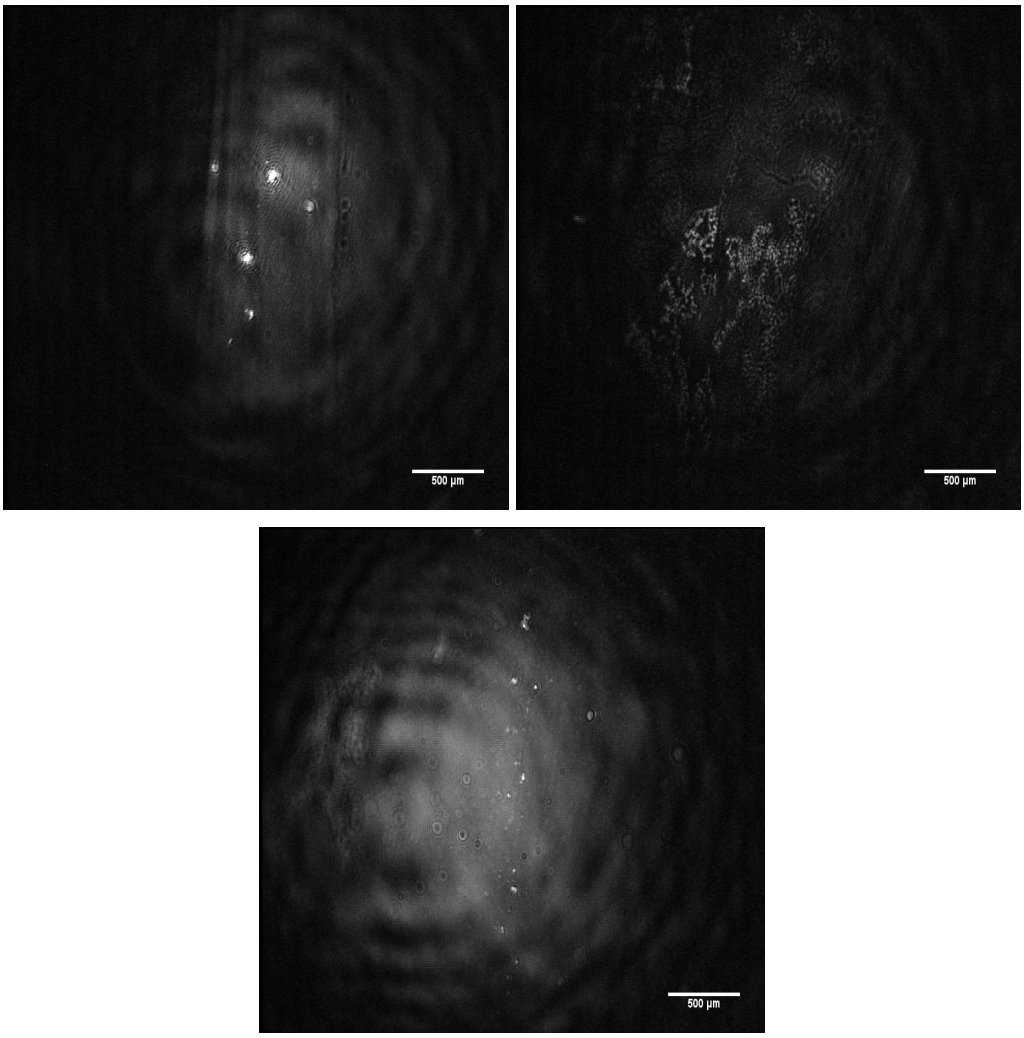

Figure 81 - BAM images of Inf-M1 on a PBS subphase. Top right Π = 0.1 mN m^{-1}, top left Π = 1.1 mN m^{-1}, bottom Π = 4.6 mN m^{-1}

The images collected show that Inf-M1 does appear to form a condensed layer on the surface slowly over time, much like hRSV-M.

Through the addition of a great excess of Inf-M1 to the subphase, it was possible to obtain a value for Π_{max} of 21.2 mN m^{-1} for Inf-M1, achieved in excess of 122 nM.

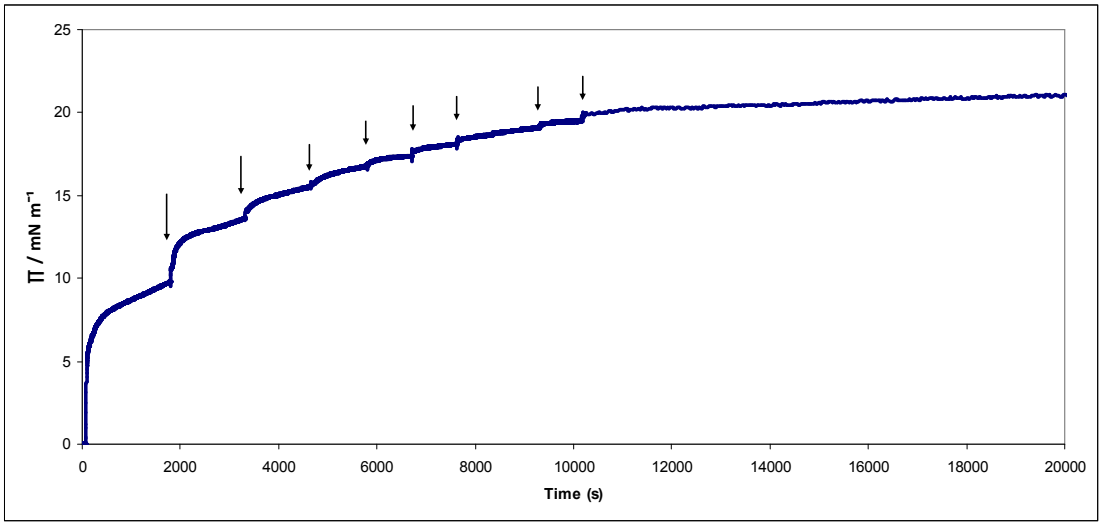

Figure 82 - Pressure / Time plot for Inf-M1. The arrows indicate the addition of extra Inf-M1, giving a final concentration of 122 nM

While most Langmuir trough experiments were ruled out, one further experiment was attempted. In order to see if Inf-M1 would have any effect on a monolayer over a long period of time, a monolayer of 15 µg DOPC/POPS (4:1) was formed, reaching Π = 44.2 mN m^{-1}. Once the pressure was stable, 5% (w/w) of Inf-M1 was added underneath the surface, giving a concentration of 13.62 nM. The pressure was then monitored over time, with BAM images being taken when possible.

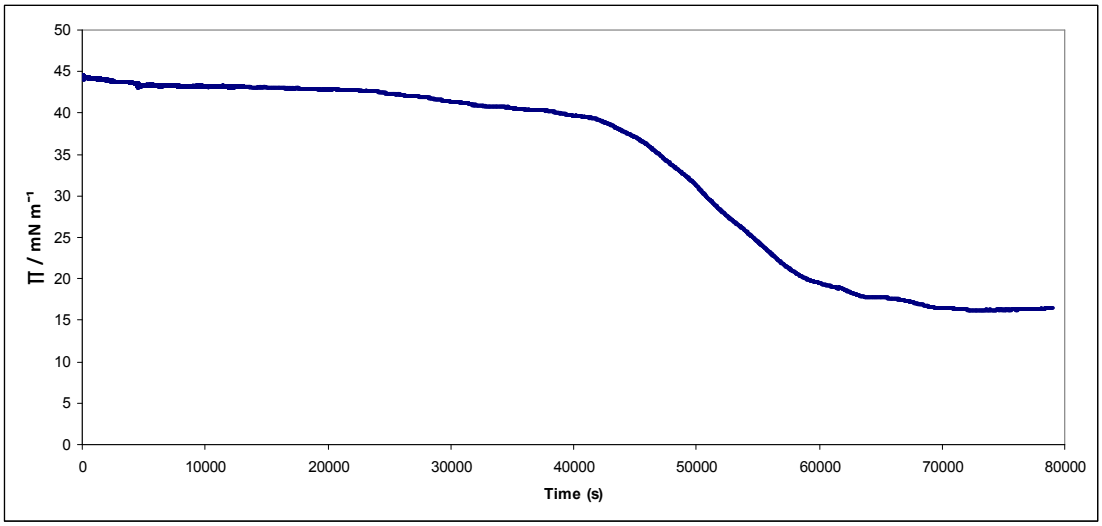

Figure 83 - Pressure/ Time plot of 15ug DOPC/POPS (4:1) with 5% (w/w) Inf-M1 added to subphase (13.62 nM)

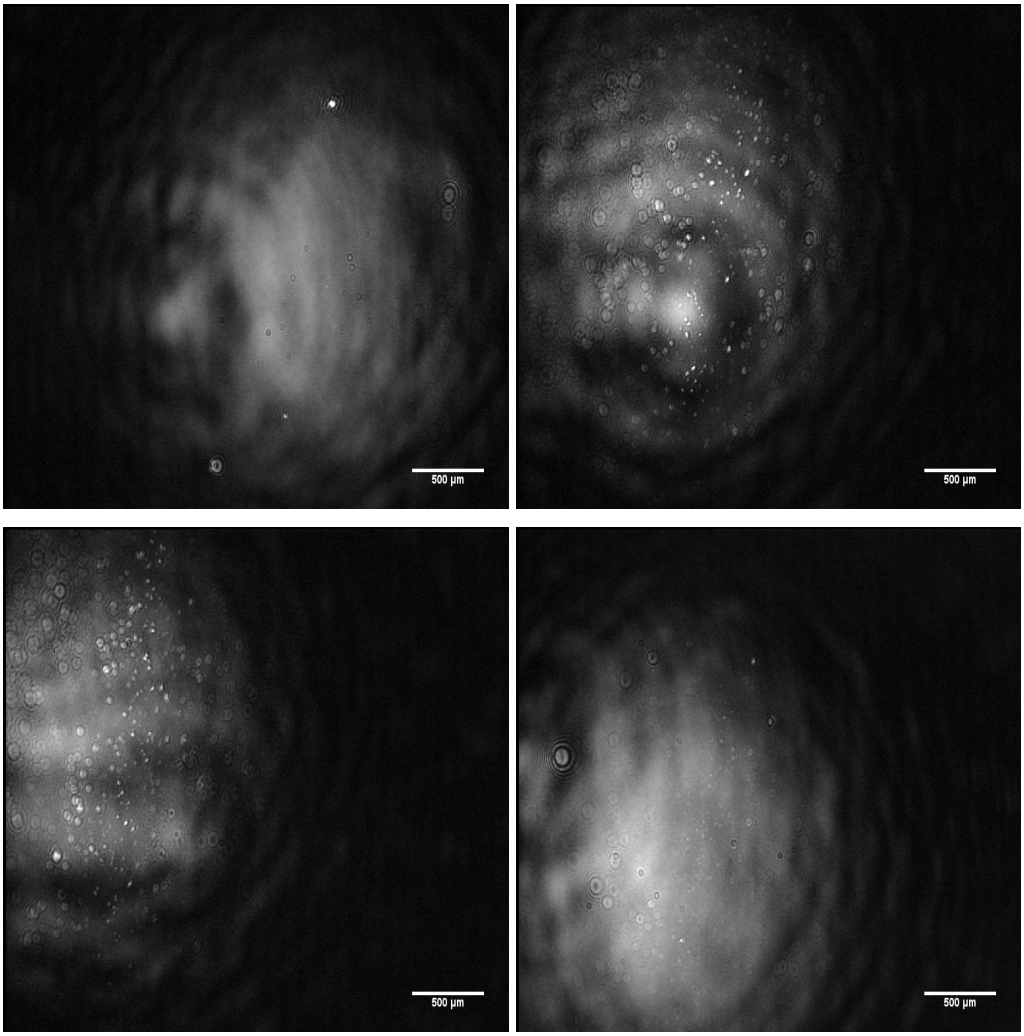

Figure 84 - Bam images of Pressure / Time plot of 15ug DOPC/POPS (4:1) with 5% (w/w) Inf-M1 added to subphase (13.62 nM) . Top left = DOPC/POPS only, top right = 20000 seconds, bottom left = 30000 seconds, bottom right = 75000 seconds

As can be seen in the data, very little change is seen in the pressure of the monolayer for the first 30000 seconds. However the BAM images show small domains forming on the surface. It appears the number of these domains becomes greater over time, until approx 45000 seconds, when the pressure begins to drop at a much faster rate. This may be interpreted as a loss of material from the surface. The pressure stabilised afterwards at 16.3 mN m^{-1}. One possibility for this behaviour is that Inf-M1 has slowly been binding to the lipid monolayer, however it is only once it has reached a critical concentration at the monolayer that it is able to have an effect. It is then subducting lipids away from the surface, most likely in the form of micelles or liposomes surrounded by Inf-M1. This continues slowly until the remaining pressure makes the lipid too disperse for Inf-M1 to bind them and thus the process stops.

Unfortunately, time was not available to carry out follow up experiments to probe this behaviour.

3.5 Giant Unilamellar Vesicles and confocal microscopy

Inf-M1 was labelled with FITC in a 1:1 ratio using the same method as hRSV-M (section 2.10). It was then applied to GUVs consisting of DOPC/POPS (1:1) at a final concentration of 5 µM. This high proportion of phosphatidylserine was used due to preivous reports that Inf-M1 binds to membranes containing at least 50% phosphatidylserine.[70, 83] The sample was then observed by confocal microscopy over one hour. Images are presented in false colour.

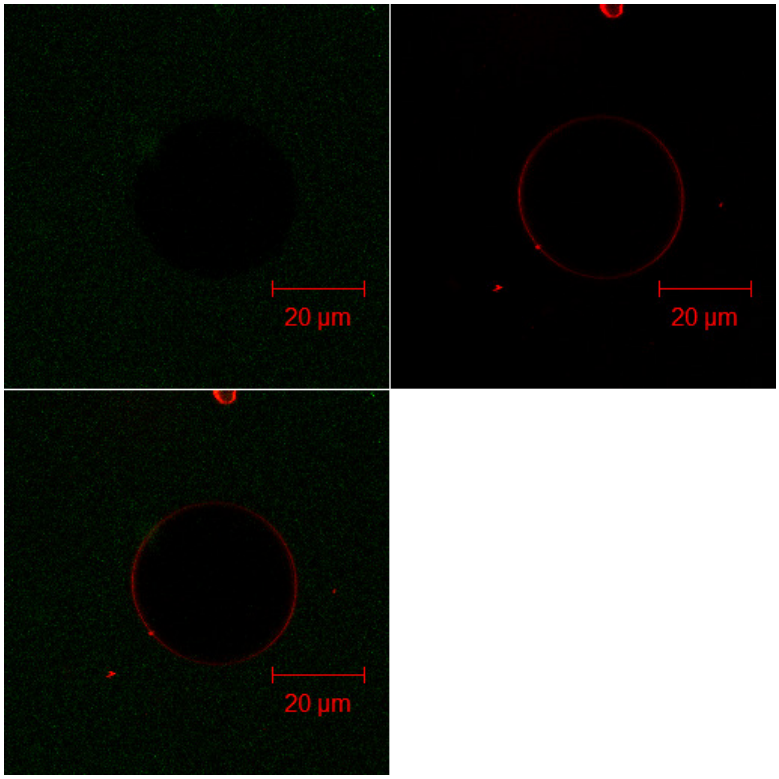

Figure 85 - Confocal image of DOPC/POPS (1:1) GUVs with 5 µM Inf-M1-FITC at T = 0 minutes. Top left = green channel, Top right = red channel, bottom = merged image

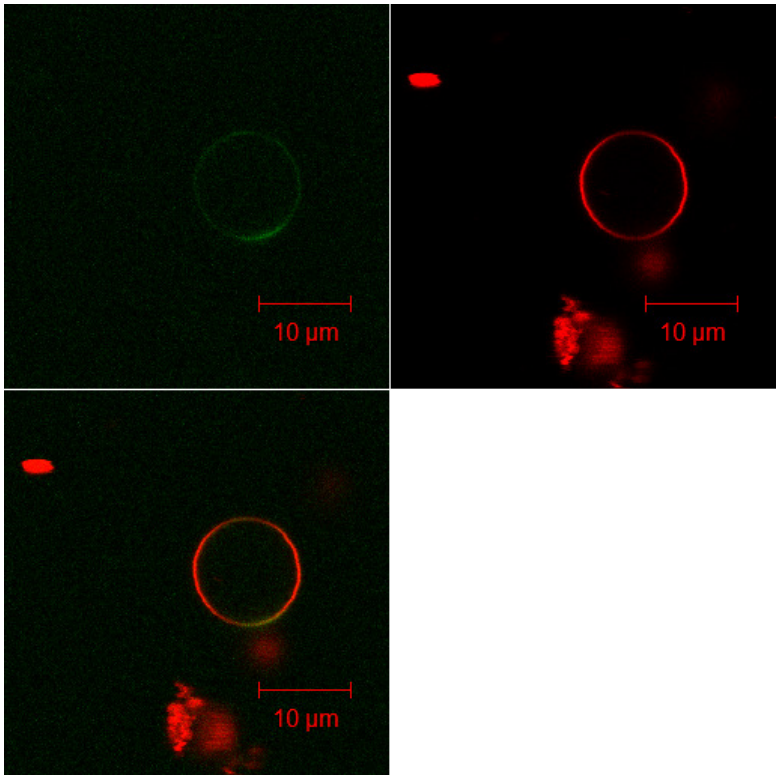

Figure 86 - Confocal image of DOPC/POPS (1:1) GUVs with 5 µM Inf-M1-FITC at T = 8 minutes. Top left = green channel, Top right = red channel, bottom = merged image

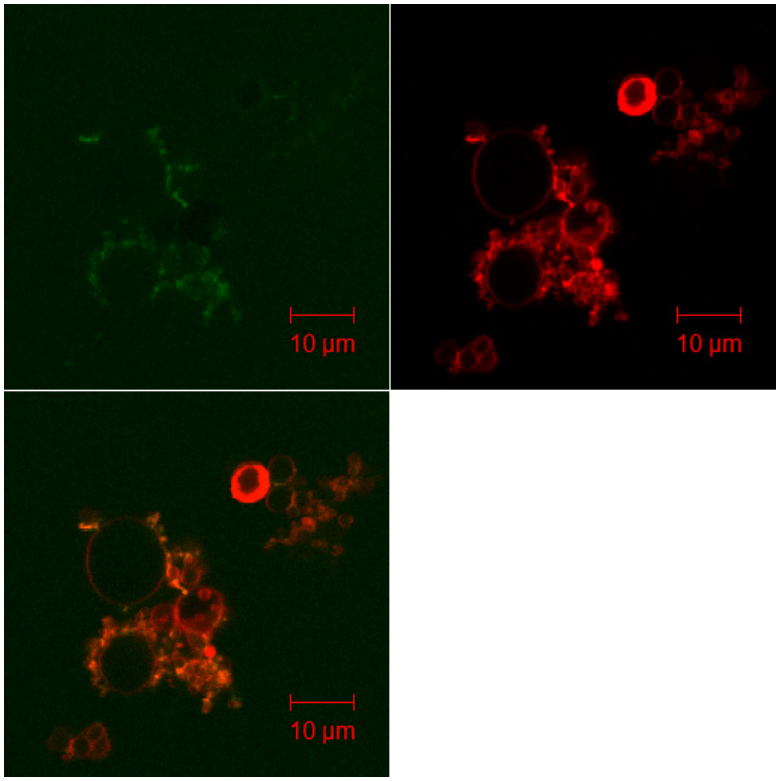

Figure 87 - Confocal image of DOPC/POPS (1:1) GUVs with 5 µM Inf-M1-FITC at T = 30 minutes. Top left = green channel, Top right = red channel, bottom = merged image

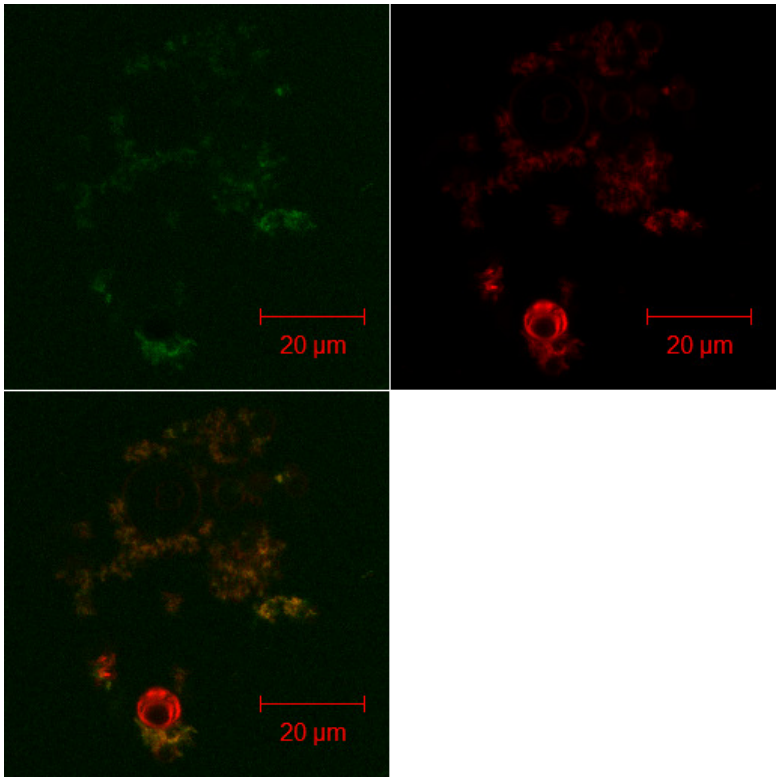

Figure 88 - Confocal image of DOPC/POPS (1:1) GUVs with 5 µM Inf-M1-FITC at T = 50 minutes. Top left = green channel, Top right = red channel, bottom = merged image

As the data shows, initially no binding of Inf-M1-FITC to GUVs can be seen. However after 8 mins it was observed that Inf-M1-FITC was binding to the surface of GUVs, with some denser patches of Inf-M1-FITC forming, as seen by the higher fluorescence. By 30 minutes into the experiment, the Inf-M1-FITC appears to have budded away from the surface of the GUVs and forming new small vesicles with some of the material. By 50 minutes there were few remaining large GUVs, with most now having budded into small vesicles, although these still remain associated with each other.

This behaviour of budding vesicles is not unique to Inf-M1, it has been described in Newcastle disease virus previously, however the budding was internal to the GUV, not externally as seen in the data presented here.[118] The budding may be caused by crowding of the protein at the surface of the GUVs, where lateral pressure exerted by proteins being in close proximity on the surface cause a curvature and eventual vesicle budding from a bilayer.[172] However we cannot identify from this experiment if the protein remains on the outer or inner face of the new vesicles.

4 Discussion and Conclusions

4.1 hRSV-M as a calcium binding protein

While this project began focused on the lipid interactions of hRSV-M, the experiments performed have led to alternative discoveries. Since the x-ray crystal structure of hRSV-M has been previously determined, and previous mass spectrometry experiments had failed to find any metals bound to hRSV-M, it was not expected that further experiments would show the presence of metals.[39, 47] However this has proven to not be the case, with the data presented here showing that when the protein is incubated with calcium, and kept out of conditions that precipitate or chelate calcium ions, that calcium ions can be found bound. Two sites were identified, one with strong binding and another with very weak. Given the ICPMS data showed only one calcium bound per protein, it is likely that this second site is non-function with respect to in-vivo activities.

The presence of metals in viral proteins is well known, however to date they have mainly been localised to proteins involving transcription and interactions with RNA, for example Ebola virus VP30 binding zinc to activate transcription and HIV-1 RNase-H using magnesium as a cofactor.[173, 174] A search of the literature shows that zinc is by far the most common metal ion found to bind viral proteins, and there was only one instance of a viral matrix protein binding metal, the Zinc binding behaviour of Influenza A M1.[175] Calcium binding to viral structural proteins was unknown until very recently, although it has been known that viruses do have large effects on calcium levels within cells and utilise cellular calcium binding proteins.[126]

However, following the completion of this work on hRSV-M's calcium binding characteristics, a paper by Leyrat *et al.* was published showing the crystal structure and calcium binding sites of Human Metapneumovirus M (HMVP-M).[176] The structure shows very high homology with that of hRSV-M, and a calcium ion can be found bound to a site within the N-terminus. The binding residues are Glu24, Asp26, Leu/Asp28 (in HMPV-M / RSV-M respectively) and Lys101.

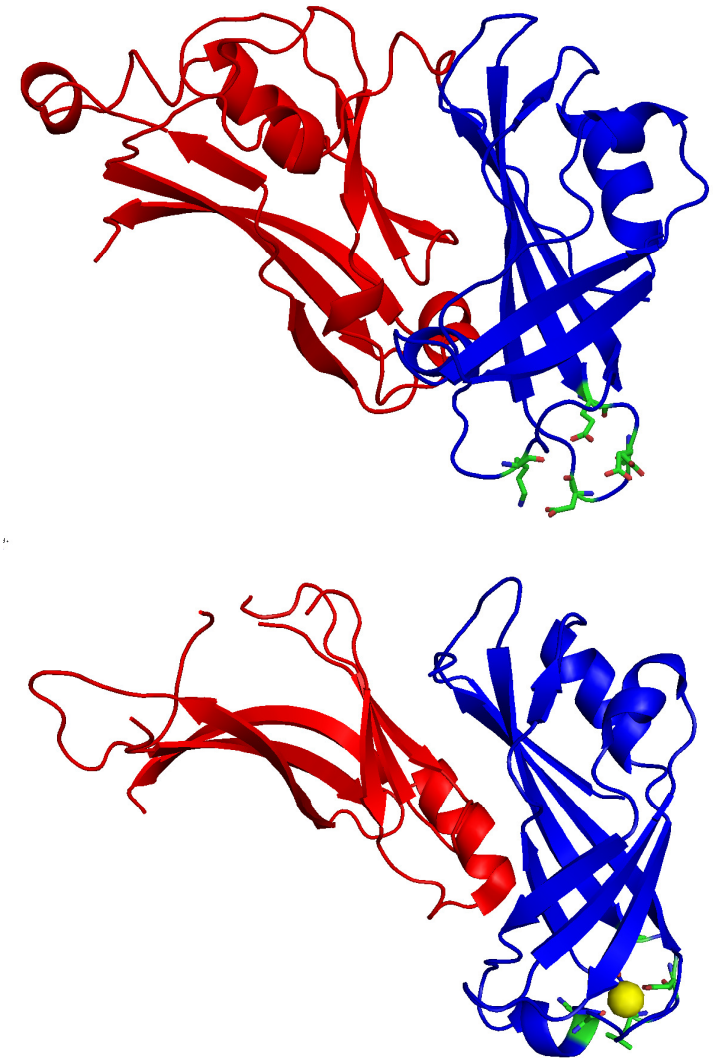

Figure 89 - X-ray crystal structures of hRSV-M (Top, PDB ID = 2VQP) and HMPV-M (Bottom, PDB ID = 4LP7). Blue = N-terminus, Red = C-terminus, Green = Residues of high affinity Ca^{2+} binding site

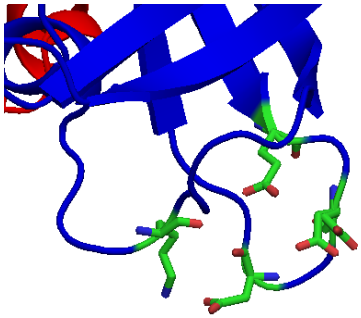

Figure 90 - Close view of residues Glu24, Asp26, Asp28 and Lys101, forming potential calcium binding site

As can be seen from the X-ray structures, the high affinity calcium binding site of HMPV-M is highly conserved in hRSV-M, making it very likely that this site is the

higher affinity site observed in our data. However, the residues in hRSV-M are in an open conformation, with the residues turned away from the potential calcium site. This is likely also responsible for the large differences in K_d calculated for this site in hRSV-M (K_d = 1.95μM) and HMPV-M (K_d = 2.0nM). I t appears that the slight structural changes in hRSV-M are enough to lower the affinity of this binding site.[176] In the x-ray crystal strucuture of hRSV-M, these residues around the binding site have slightly less well defined electron density, with residues 99 and 100 not being directly assigned in the structure, further showing that this binding pocket may be flexible.

They also identified a second potential calcium binding site with a much higher K_d (158 μM), formed of residues Val94, Asp97, Glu98 and Gln231. These residues are again conserved in hRSV-M, suggesting this is also the low affinity site in this protein. Since ICPMS showed this site to not be occupied once the protein was removed from a calcium containing solution, this site may be involved in increasing stability of the protein in the extracellular fluid where the free calcium concentration is much higher.

The role of calcium in hRSV-M has yet to be established. Calcium levels within a cell are altered by many viruses, with RSV replication and syncitium formation shown to be inhibited by low cellular levels of calcium, and the degree of conservation of these residues suggests that they are important for the virus.[177] The calcium content of a cell Leyrat *et al.* suggest that since the Ca^{2+} binding site is on the convex face of M it is in contact with the nucleocapsid proteins, and so Ca^{2+} binding may be a method of controlling virus assembly and budding.

4.2 hRSV-M interacting with lipids and membranes

This work has helped further our understanding of hRSV-M interacting with lipids. Our group has previously reported on the interactions of hRSV-M with DOPC/Sphingomyelin/Cholesterol monolayer mixtures, with the opinion that hRSV-M was partitioning into the L_d phases of this mixture, while binding extrinsically to the L_o phases. Experiments using single component monolayers of cholesterol and sphingomyelin showed that these lipids do not show any specific interaction with

hRSV-M. However when these lipids were combined the behaviour of the protein changed but still showed insertion into the monolayer. This suggest that the previously observed behaviour is unique to the ternary mixture of these lipids. One possibility is that the protein requires a specific line tension in order for interaction with the surface to occur, as line tension has been shown to be important in viral budding.[178, 179] This is supported by the experiments with DOPC/SM/Chol GUVs which again showed binding of small amount of hRSV-M to their surface.

This work has also shown that hRSV-M has a great affinity for binding the negatively charged phosphatidylserine lipids. The binding of hRSV-M to a monolayer of DOPC/DPPS can be seen by BAM to induce the formation of small domains, presumably clusters of protein that have organised the lipids into DPPS rich domains, and overall stabilising the monolayer. The experiments with GUVs however showed the most convincing results with phosphatidylserine. It could be seen the hRSV-M was unable to cross a membrane bilayer, but instead could be found binding to patches on the outside of phosphatidylserine containing GUVs. The domains were smaller on those GUVs with a lower phosphatidylserine ratio, likely due to hRSV-M clustering the available DPPS into highly enriched domains, but the available DPPS being depleted before these domains could grow larger. This interaction of HRSV-M with a negatively charged membrane has also been shown in other viral matrix proteins, such as HIV-1-Gag, Influenza a M1 and Ebola VP40.[83, 90, 180] The strong interaction with negatively charged lipids is likely due to the 600 $Å^2$ positively charged face of the protein found in the x-ray crystal structure.[39]

When the L_o domains of a sphingomyelin/cholesterol mixture and phosphatidylserine were combined, the effect of hRSV-M on the GUV changed quite dramatically. While at first hRSV-M bound all over the surface of the GUVs, after a short time small spots of high hRSV-M density were observed. It is possible that a combination hRSV-M clustering phosphatidylserine together and the increased membrane pressure from the L_o lipid components crated conditions for hRSV-M to oligomerise and form the beginnings of a virus-like particle.

Unfortunately the work started on hRSV-M with lipid nanodiscs was not able to be fully completed due to time constrains. However the initial experiments showing

potential hRSV-M binding to POPS nanodisc does suggest that these may be a useful tool in the future for studying peripheral membrane binding proteins and determining their membrane bound structure.

4.3 Influenza A M1

While work on Influenza A M1 was not advanced very far due to time constraints, the experiments so far have proved a useful starting point for further work to study this protein. A robust method has been developed for the expression and purification of Inf-M1, and the limits of its stability have been found. Domain formation of phosphatidylserine containing monolayers was observed, in a similar manner to that described for hRSV-M, except over a much longer time span. The longer time span involved in Inf-M1 membrane interactions suggests that there is another mechanism involved in targeting it to membranes that has yet to be identified.

Inf-M1 binding to GUVs containing a high proportion of phosphatidylserine showed that the protein is able to induce vesicle budding over time. A likely interpretation of this is that Inf-M1 binds to the surface and induces a change in membrane curvature. After a critical amount of protein has bound to a small portion of the membrane the pressure exerted by the protein is enough to cause the budding. This mechanism has been identified as an intrinsic property in several other proteins.[179, 181] Similar behaviour has been observed in the related Newcastle disease virus, where binding of the protein caused vesicle formation, however this did not require phosphatidylserine and the vesicles budded inward of the GUV.[97, 182] The observed affinity of Inf-M1 to a negatively charged membrane corresponds to previously published data.[83]

4.4 Future Work

4.4.1 hRSV-M

While the investigation of calcium interacting with hRSV-M was started, there are further experiments that may be conducted in the future to expand our knowledge. A first step, given the results of Leyrat *et al.* is to attempt to crystallise hRSV-M with calcium present. If a structure can be found with one or both calcium binding sites occupied it may help to explain the differences in calcium K_d seen between HMPV-M and hRSV-M, and the changes in protein stability observed. This experiment was attempted and crystals were formed, however they did not diffract. If crystals are unable to be formed, then small angle x-ray scattering (SAXS) to give some structural information of any possible changes upon calcium binding.

While a calcium binding constant was collected during this work, it would be advisable to confirm the values through other experiments. A technique such as isothermal titration calorimetry could be used for this, while also giving extra parameters for the interaction. The main downside of this is that the weak binding of the second site may make it difficult to analyse. Another alternative technique would be to use a fluorescent calcium binding molecule and conduct a competitive binding assay.

While the lipid binding characteristics of hRSV-M have been clarified further, there are still more interesting possibilities to look into. While the negatively charged phosphatidylserines have been looked at in this work, it would be useful to study other negatively charged lipids found in the membrane. Particularly, the phosphatidylinositols can be highly negatively charged due to multiple phosphate groups, and are often found in viral envelopes.[141] Phosphatidylglycerols may also be a good candidate, since they are found predominately in lung surfactant, which hRSV-M is likely to come into contact with during infection cycles.[183]

GUV experiments may also be continued. It may be useful to study mixtures of lipids where phosphatidylserine is localised to either L_o or L_d domains, to see if the clustering effect of hRSV-M on these lipids remains. GUVs can also be formed out of lipids extracted from cells, and using these would reveal the natural behaviour of hRSV-M on cell membranes.[155] The binding kinetics could also be studied by using a micro-injector to inject small amounts of hRSV-M close to the surface of a GUV and monitor its effects over time. Domain formation could also be visualised by this

method. GUVs could also be used for patch-clamp experiments, monitoring the electrical admittance over time as hRSV-M binds to the surface.

To study the conformation of hRSV-M binding to lipids, Fluorescence resonance energy transfer (FRET) could be used. This could be done in two different ways to give different information. By a modification of the existing GUV method using two suitable fluorophores, one on the protein and one in the membrane, and a confocal microscope able to do fluorescence lifetime imaging (FLIM). Measuring the distance between the fluorophores would tell us at what orientation the protein has bound to the membrane. Alternatively, by labelling the protein with two fluorophores, one at the N-terminus and one at the C-terminus, it may be possible to determine the orientation of the two domains relative to each other upon lipid binding.

The orientation of hRSV-M could also be determined by neutron reflectivity experiments. An attempt was made to do this at ILL, Grenoble, however binding could not be seen. With the details learned in the work about the binding of hRSV-M, it may be possible to collect better data now.

4.4.2 Infuenza-A-M1

Many of the experiments carried out on hRSV-M can be extended to Inf-M1. A major goal in research on Inf-M1 would be the crystallisation and 3D structural determination of the intact protein. While the N-terminus has been determined, the C-terminus and linker region have not been crystallised. Conditions were tested for crystallisation, however no crystals formed. SAXS and Neutron reflectivity may also prove useful in determining the full structure of Inf-M1.

One planned experiment that unfortunately could not be completed was to apply Inf-M1 to lipid nanodiscs in the same matter as hRSV-M. The reasoning for this was that the rapid degradation of the protein may make crystallisation of the intact protein impossible, and so by instead binding Inf-M1 to nanodiscs and collecting the electron

density from Cryo-EM images it may be possible to build up a model of Inf-M1. It may also give valuable information on its lipid binding surface and possible oligomers formed at the lipid surface. FRET experiments similar to those described above may also be useful.

Since Langmuir isotherms may not be a possible method for examining Inf-M1 lipid binding, other methods may be examined. Using ITC with Inf-M1 and liposomes would allow binding parameters to be calculated. Imaging of Inf-M1 bound to a membrane could also provide valuable information, and could be achieved by atomic force microscopy of a prepared bilayer from a Langmuir-Blodgett deposition.

The ability of Inf-M1 to bud small vesicles/liposomes away from giant vesicles suggests that it may be a good candidate for patch clamp technique. This technique has already been used for similar behaviour seen in Newcastle disease virus.[182] By taking a patch of a GUV membrane and applying Inf-M1 to it, the electrical admittance would change as the composition of the membrane changes as lipids are removed.

5 References

1. H. Lodish, A. Berk, P. Matsudaira, C. Kaiser, M. Krieger, M. Scott, S. L. Zipursky and J. Darnell, *Molecular Cell Biology*, 5th edn., W. H. Freeman and Company, 2004.
2. V. G. Khurana and F. B. Meyer, *Journal of Cerebral Blood Flow and Metabolism*, 2003, **23**, 1251-1262.
3. Baltimor.D, *Bacteriological Reviews*, 1971, **35**, 235-241.
4. M. Marsh, *Biochemical Journal*, 1984, **218**, 1-10.
5. E. Fahy, S. Subramaniam, H. A. Brown, C. K. Glass, A. H. Merrill, R. C. Murphy, C. R. H. Raetz, D. W. Russell, Y. Seyama, W. Shaw, T. Shimizu, F. Spener, G. van Meer, M. S. VanNieuwenhze, S. H. White, J. L. Witztum and E. A. Dennis, *Journal of Lipid Research*, 2005, **46**, 839-861.
6. S. J. Singer and G. L. Nicolson, *Science*, 1972, **175**, 720-731.
7. J. M. Sanderson, *Organic & Biomolecular Chemistry*, 2005, **3**, 201-212.
8. J. Eisenblatter and R. Winter, *Biophysical Journal*, 2006, **90**, 956-966.
9. T. P. W. McMullen, R. Lewis and R. N. McElhaney, *Current Opinion in Colloid & Interface Science*, 2004, **8**, 459-468.
10. L. J. Johnston, *Langmuir*, 2007, **23**, 5886-5895.
11. D. A. Brown and J. K. Rose, *Cell*, 1992, **68**, 533-544.
12. D. A. Brown and E. London, *Annual Review of Cell and Developmental Biology*, 1998, **14**, 111-136.
13. D. Lichtenberg, F. M. Goni and H. Heerklotz, *Trends in Biochemical Sciences*, 2005, **30**, 430-436.
14. H. J. Kaiser, D. Lingwood, I. Levental, J. L. Sampaio, L. Kalvodova, L. Rajendran and K. Simons, *Proceedings of the National Academy of Sciences of the United States of America*, 2009, **106**, 16645-16650.
15. S. May, *Soft Matter*, 2009, **5**, 3148-3156.
16. P. Rock, M. Allietta, W. W. Young, T. E. Thompson and T. W. Tillack, *Biochemistry*, 1990, **29**, 8484-8490.
17. A. Asanov, A. Zepeda and L. Vaca, *Biochimica Et Biophysica Acta-Molecular and Cell Biology of Lipids*, 2010, **1801**, 147-155.
18. D. Lingwood and K. Simons, *Science*, 2010, **327**, 46-50.
19. N. Chazal and D. Gerlier, *Microbiology and Molecular Biology Reviews*, 2003, **67**, 226-237.
20. P. Scheiffele, P. Verkade, A. M. Fra, H. Virta, K. Simons and E. Ikonen, *Journal of Cell Biology*, 1998, **140**, 795-806.
21. G. Brown, C. E. Jeffree, T. McDonald, H. W. M. Rixon, J. D. Aitken and R. J. Sugrue, *Virology*, 2004, **327**, 175-185.
22. R. C. Aloia, H. R. Tian and F. C. Jensen, *Proceedings of the National Academy of Sciences of the United States of America*, 1993, **90**, 5181-5185.
23. S. Bavari, C. M. Bosio, E. Wiegand, G. Ruthel, A. B. Will, T. W. Geisbert, M. Hevey, C. Schmaljohn, A. Schmaljohn and M. J. Aman, *Journal of Experimental Medicine*, 2002, **195**, 593-602.
24. Current Status of Respiratory Syncytial Virus (RSV) and Parainfluenza Virus Type 3 (PIV3) Vaccine Development: Memorandum from a Joint WHO/NIAID Meeting, 1997, *World Health Organisation*, http://www.who.int.

25. A. R. Falsey, K. L. Becker, A. J. Swinburne, E. S. Nylen, M. A. Formica, P. A. Hennessey, M. M. Criddle, D. R. Peterson, A. Baran and E. E. Walsh, *Journal of Infectious Diseases*, 2013, **208**, 432-441.
26. A. R. Falsey, P. A. Hennessey, M. A. Formica, C. Cox and E. E. Walsh, *New England Journal of Medicine*, 2005, **352**, 1749-1759.
27. O. Dibben, L. C. Thorpe and A. J. Easton, *Virus Research*, 2008, **131**, 47-53.
28. K. El Omari, B. Dhaliwal, J. Ren, N. G. A. Abrescia, M. Lockyer, K. L. Powell, A. R. Hawkins and D. K. Stammers, *Acta Crystallographica Section F-Structural Biology and Crystallization Communications*, 2011, **67**, 1179-1183.
29. B. GarciaBarreno, T. Delgado and J. A. Melero, *Journal of Virology*, 1996, **70**, 801-808.
30. J. Fix, M. Galloux, M.-L. Blondot and J.-F. Eleouet, *The Open Virology Journal*, 2011, **5**, 103-108.
31. S. Swedan, A. Musiyenko and S. Barik, *Journal of Virology*, 2009, **83**, 9682-9693.
32. S. F. Swedan and S. Barik, *Faseb Journal*, 2009, **23**, 5353-5362.
33. X. Zhao, M. Singh, V. N. Malashkevich and P. S. Kim, *Proceedings of the National Academy of Sciences of the United States of America*, 2000, **97**, 14172-14177.
34. G. W. Wertz, P. L. Collins, H. A. Yung, C. Gruber, S. Levine and L. A. Ball, *Proceedings of the National Academy of Sciences of the United States of America*, 1985, **82**, 4075-4079.
35. S. Fuentes, K. C. Tran, P. Luthra, M. N. Teng and B. He, *Journal of Virology*, 2007, **81**, 8361-8366.
36. T. Takimoto and A. Portner, *Virus Research*, 2004, **106**, 133-145.
37. S. R. Roberts, R. W. Compans and G. W. Wertz, *Journal of Virology*, 1995, **69**, 2667-2673.
38. M. Batonick, A. G. P. Oomens and G. W. Wertz, *Journal of Virology*, 2008, **82**, 8664-8672.
39. V. A. Money, H. K. McPhee, J. A. Mosely, J. M. Sanderson and R. P. Yeo, *Proceedings of the National Academy of Sciences of the United States of America*, 2009, **106**, 4441-4446.
40. J. M. Sanderson and E. J. Whelan, *Physical Chemistry Chemical Physics*, 2004, **6**, 1012-1017.
41. K. Latiff, J. Meanger, J. Mills and R. Ghildyal, *Clinical Microbiology and Infection*, 2004, **10**, 945-948.
42. E. C. Coronel, T. Takimoto, K. G. Murti, N. Varich and A. Portner, *Journal of Virology*, 2001, **75**, 1117-1123.
43. R. Ghildyal, D. S. Li, I. Peroulis, B. Shields, P. G. Bardin, M. N. Teng, P. L. Collins, J. Meanger and J. Mills, *Journal of General Virology*, 2005, **86**, 1879-1884.
44. R. Ghildyal, J. Mills, M. Murray, N. Vardaxis and J. Meanger, *Journal of General Virology*, 2002, **83**, 753-757.
45. M. N. Teng and P. L. Collins, *Journal of Virology*, 1998, **72**, 5707-5716.
46. M. Gaudier, Y. Gaudin and M. Knossow, *Virology*, 2001, **288**, 308-314.
47. H. K. McPhee, J. L. Carlisle, A. Beeby, V. A. Money, S. M. D. Watson, R. P. Yeo and J. M. Sanderson, *Langmuir*, 2011, **27**, 304-311.
48. A. Marty, J. Meanger, J. Mills, B. Shields and R. Ghildyal, *Archives of Virology*, 2004, **149**, 199-210.

49. G. Henderson, J. Murray and R. P. Yeo, *Virology*, 2002, **300**, 244-254.
50. R. Ghildyal, C. Baulch-Brown, J. Mills and J. Meanger, *Archives of Virology*, 2003, **148**, 1419-1429.
51. A. Harris, B. D. Sha and M. Luo, *Journal of General Virology*, 1999, **80**, 863-869.
52. D. P. Nayak, R. A. Balogun, H. Yamada, Z. H. Zhou and S. Barman, *Virus Research*, 2009, **143**, 147-161.
53. Y. Lu, M. Wambach, M. G. Katze and R. M. Krug, *Virology*, 1995, **214**, 222-228.
54. R. E. O'Neill, J. Talon and P. Palese, *Embo Journal*, 1998, **17**, 288-296.
55. R. M. Pielak and J. J. Chou, *Biochimica Et Biophysica Acta-Biomembranes*, 2011, **1808**, 522-529.
56. M. Veit and B. Thaa, *Advances in virology*, 2011, **2011**, 1-14.
57. J. S. Rossman and R. A. Lamb, *Virology*, 2011, **411**, 229-236.
58. W. F. Shi, F. M. Lei, C. D. Zhu, F. Sievers and D. G. Higgins, *Plos One*, 2010, **5**, e14454.
59. L. J. Calder, S. Wasilewski, J. A. Berriman and P. B. Rosenthal, *Proceedings of the National Academy of Sciences of the United States of America*, 2010, **107**, 10685-10690.
60. P. C. Roberts, R. A. Lamb and R. W. Compans, *Virology*, 1998, **240**, 127-137.
61. P. W. Choppin, J. S. Murphy and I. Tamm, *Journal of Experimental Medicine*, 1960, **112**, 895-920.
62. S. Arzt, F. Baudin, A. Barge, P. Timmins, W. P. Burmeister and R. W. H. Ruigrok, *Virology*, 2001, **279**, 439-446.
63. B. D. Sha and M. Luo, *Acta Crystallographica Section D-Biological Crystallography*, 1997, **53**, 458-460.
64. A. V. Shishkov, V. I. Goldanskii, L. A. Baratova, N. V. Fedorova, A. L. Ksenofontov, O. P. Zhirnov and A. V. Galkin, *Proceedings of the National Academy of Sciences of the United States of America*, 1999, **96**, 7827-7830.
65. C. Elster, E. Fourest, F. Baudin, K. Larsen, S. Cusack and R. W. H. Ruigrok, *Journal of General Virology*, 1994, **75**, 37-42.
66. C. Elster, K. Larsen, J. Gagnon, R. W. H. Ruigrok and F. Baudin, *Journal of General Virology*, 1997, **78**, 1589-1596.
67. L. Wakefield and G. G. Brownlee, *Nucleic Acids Research*, 1989, **17**, 8569-8580.
68. J. J. Zhang, G. Li, X. L. Liu, Z. F. Wang, W. J. Liu and X. Ye, *Journal of General Virology*, 2009, **90**, 2751-2758.
69. R. W. Hankins, K. Nagata, A. Kato and A. Ishihama, *Research in Virology*, 1990, **141**, 305-314.
70. F. Baudin, I. Petit, W. Weissenhorn and R. W. H. Ruigrok, *Virology*, 2001, **281**, 102-108.
71. X. Y. Huang, T. Liu, J. Muller, R. A. Levandowski and Z. P. Ye, *Virology*, 2001, **287**, 405-416.
72. I. Garcia-Robles, H. Akarsu, C. W. Muller, R. W. H. Ruigrok and F. Baudin, *Virology*, 2005, **332**, 329-336.
73. H. Akarsu, W. P. Burmeister, C. Petosa, I. Petit, C. W. Muller, R. W. H. Ruigrok and F. Baudin, *Embo Journal*, 2003, **22**, 4646-4655.
74. G. R. Whittaker and P. Digard, *Influenza Virology: Current Topics*, 2006, 37-64.

75. P. Digard, D. Elton, K. Bishop, E. Medcalf, A. Weeds and B. Pope, *Journal of Virology*, 1999, **73**, 2222-2231.
76. R. T. Avalos, Z. Yu and D. P. Nayak, *Journal of Virology*, 1997, **71**, 2947-2958.
77. M. Simpson-Holley, D. Ellis, D. Fisher, D. Elton, J. McCauley and P. Digard, *Virology*, 2002, **301**, 212-225.
78. M. Enami and K. Enami, *Journal of Virology*, 1996, **70**, 6653-6657.
79. A. Ali, R. T. Avalos, E. Ponimaskin and D. P. Nayak, *Journal of Virology*, 2000, **74**, 8709-8719.
80. K. Iwatsuki-Horimoto, T. Horimoto, T. Noda, M. Kiso, J. Maeda, S. Watanabe, Y. Muramoto, K. Fujii and Y. Kawaoka, *Journal of Virology*, 2006, **80**, 5233-5240.
81. M. F. McCown and A. Pekosz, *Journal of Virology*, 2006, **80**, 8178-8189.
82. E. Kretzschmar, M. Bui and J. K. Rose, *Virology*, 1996, **220**, 37-45.
83. R. W. H. Ruigrok, A. Barge, P. Durrer, J. Brunner, K. Ma and G. R. Whittaker, *Virology*, 2000, **267**, 289-298.
84. S. V. Bourmakina and A. Garcia-Sastre, *Journal of Virology*, 2005, **79**, 7926-7932.
85. P. Gomez-Puertas, C. Albo, E. Perez-Pastrana, A. Vivo and A. Portela, *Journal of Virology*, 2000, **74**, 11538-11547.
86. T. Latham and J. M. Galarza, *Journal of Virology*, 2001, **75**, 6154-6165.
87. S. V. Bourmakina and A. Garcia-Sastre, *Journal of General Virology*, 2003, **84**, 517-527.
88. T. Liu, J. Muller and Z. P. Ye, *Virology*, 2002, **304**, 89-96.
89. A. Dessen, V. Volchkov, O. Dolnik, H. D. Klenk and W. Weissenhorn, *Embo Journal*, 2000, **19**, 4228-4236.
90. R. W. H. Ruigrok, G. Schoehn, A. Dessen, E. Forest, V. Volchkov, O. Dolnik, H. D. Klenk and W. Weissenhorn, *Journal of Molecular Biology*, 2000, **300**, 103-112.
91. T. Hoenen, V. Volchkov, L. Kolesnikova, E. Mittler, J. Timmins, M. Ottmann, O. Reynard, S. Becker and W. Weissenhorn, *Journal of Virology*, 2005, **79**, 1898-1905.
92. T. Hoenen, N. Biedenkopf, F. Zielecki, S. Jung, A. Groseth, H. Feldmann and S. Becker, *Journal of Virology*, 2010, **84**, 7053-7063.
93. L. P. Silva, M. Vanzile, S. Bavari, J. M. J. Aman and D. C. Schriemer, *Plos One*, 2012, **7**.
94. K. S. Faaberg and M. E. Peeples, *Virology*, 1988, **166**, 123-132.
95. H. D. Pantua, L. W. McGinnes, M. E. Peeples and T. G. Morrison, *Journal of Virology*, 2006, **80**, 11062-11073.
96. J. P. Laliberte, L. W. McGinnes, M. E. Peeples and T. G. Morrison, *Journal of Virology*, 2006, **80**, 10652-10662.
97. A. V. Shnyrova and J. Zimmerberg, in *Methods in Enzymology; Liposomes, Pt F*, ed. N. Duzgunes, Elsevier Academic Press Inc, San Diego, Editon edn., 2009, vol. 464, pp. 55-75.
98. N. A. Coleman and M. E. Peeples, *Virology*, 1993, **195**, 596-607.
99. M. E. Peeples, W. Can, K. C. Gupta and N. Coleman, *Journal of Virology*, 1992, **66**, 3263-3269.
100. J. McLauchlan, *Journal of Viral Hepatitis*, 2000, **7**, 2-14.
101. P. Targett-Adams, G. Hope, S. Boulant and J. McLauchlan, *Journal of Biological Chemistry*, 2008, **283**, 16850-16859.

102. R. G. Hope, M. J. McElwee and J. McLauchlan, *Journal of General Virology*, 2006, **87**, 623-627.
103. N. Majeau, V. Gagne, M. Bolduc and D. Leclerc, *Journal of General Virology*, 2005, **86**, 3055-3064.
104. E. Santolini, G. Migliaccio and N. Lamonica, *Journal of Virology*, 1994, **68**, 3631-3641.
105. G. Barba, F. Harper, T. Harada, M. Kohara, S. Goulinet, Y. Matsuura, G. Eder, Z. Schaff, M. J. Chapman, T. Miyamura and C. Brechot, *Proceedings of the National Academy of Sciences of the United States of America*, 1997, **94**, 1200-1205.
106. K. Ogawa, T. Hishiki, Y. Shimizu, K. Funami, K. Sugiyama, Y. Miyanari and K. Shimotohno, *Proceedings of the Japan Academy Series B-Physical and Biological Sciences*, 2009, **85**, 217-228.
107. S. Boulant, M. W. Douglas, L. Moody, A. Budkowska, P. Targett-Adams and J. McLauchlan, *Traffic*, 2008, **9**, 1268-1282.
108. G. Qiang, L. Yang, R. P. Witek and R. Jhaveri, *Virus Research*, 2009, **139**, 127-130.
109. K. H. Kim, S. P. Hong, K. Kim, M. J. Park, K. J. Kim and J. Cheong, *Biochemical and Biophysical Research Communications*, 2007, **355**, 883-888.
110. E. Blanchard, C. Hourioux, D. Brand, M. Ait-Goughoulte, A. Moreau, S. Trassard, P. Y. Sizaret, F. Dubois and P. Roingeard, *Journal of Virology*, 2003, **77**, 10131-10138.
111. S. Boulant, P. Targett-Adams and J. McLauchlan, *Journal of General Virology*, 2007, **88**, 2204-2213.
112. P. Roingeard, C. Hourioux, E. Blanchard and G. Prensier, *Histochemistry and Cell Biology*, 2008, **130**, 561-566.
113. R. G. Hope and J. McLauchlan, *Journal of General Virology*, 2000, **81**, 1913-1925.
114. R. G. Hope, D. J. Murphy and J. McLauchlan, *Journal of Biological Chemistry*, 2002, **277**, 4261-4270.
115. A. J. Perez-Berna, A. S. Veiga, M. Castanho and J. Villalain, *Journal of Viral Hepatitis*, 2008, **15**, 346-356.
116. C. Hourioux, M. Ait-Goughoulte, R. Patient, D. Fouquenet, F. Arcanger-Doudet, D. Brand, A. Martin and P. Roingeard, *Cellular Microbiology*, 2007, **9**, 1014-1027.
117. N. Majeau, R. Fromentin, C. Savard, M. Duval, M. J. Tremblay and D. Leclerc, *Journal of Biological Chemistry*, 2009, **284**, 33915-33925.
118. G. Barba, F. Harper,T. Harada, M. Kohara, S. Goulinet,Y. Matsuura, G. Eder, Zs. Schaff, M. J. Chapman, T. Miyamura, and C. Bréchot, PNAS, 1997, **94**, 1200-1205
119. F. H. Niesen, H. Berglund and M. Vedadi, *Nature Protocols*, 2007, **2**, 2212-2221.
120. J. K. Kranz and C. Schalk-Hihi, *Fragment-Based Drug Design: Tools, Practical Approaches, and Examples*, 2011, **493**, 277-298.
121. C. B. Anfinsen, *Science*, 1973, **181**, 223-230.
122. S. Duhr and D. Braun, *Proceedings of the National Academy of Sciences of the United States of America*, 2006, **103**, 19678-19682.
123. S. A. I. Seidel, P. M. Dijkman, W. A. Lea, G. van den Bogaart, M. Jerabek-Willemsen, A. Lazic, J. S. Joseph, P. Srinivasan, P. Baaske, A. Simeonov, I.

Katritch, F. A. Melo, J. E. Ladbury, G. Schreiber, A. Watts, D. Braun and S. Duhr, *Methods*, 2013, **59**, 301-315.
124. C. J. Wienken, P. Baaske, U. Rothbauer, D. Braun and S. Duhr, *Nature Communications*, 2010, **1,** 100.
125. X. J. Liang and Y. G. Huang, *Bioscience Reports*, 2000, **20**, 129-138.
126. Y. Zhou, T. K. Frey and J. J. Yang, *Cell Calcium*, 2009, **46**, 1-17.
127. R. Shainkinkestenbaum, Y. Winikoff, C. Chaimovitz, S. Zimlichman and I. Sarov, *Israel Journal of Medical Sciences*, 1993, **29**, 2-6.
128. S. W. Gan, L. Ng, X. Lin, X. Gong and J. Torres, *Protein Science*, 2008, **17**, 813-820.
129. S. M. Kelly, T. J. Jess and N. C. Price, *Biochimica Et Biophysica Acta-Proteins and Proteomics*, 2005, **1751**, 119-139.
130. L. Whitmore and B. A. Wallace, *Biopolymers*, 2008, **89**, 392-400.
131. B. Persson, A. F. Hartog, J. Rydstrom and J. A. Berden, *Biochimica Et Biophysica Acta*, 1988, **953**, 241-248.
132. M. Miki, *Journal of Biochemistry*, 1985, **97**, 1067-1072.
133. W. J. Cooper, R. G. Zika, R. G. Petasne and J. M. C. Plane, *Environmental Science & Technology*, 1988, **22**, 1156-1160.
134. R. Koynova and M. Caffrey, *Biochimica Et Biophysica Acta-Biomembranes*, 2001, **1513**, 82-82.
135. R. B. Chan, L. Tanner and M. R. Wenk, *Chemistry and Physics of Lipids*, 2010, **163**, 449-459.
136. F. M. Goni, A. Alonso, L. A. Bagatolli, R. E. Brown, D. Marsh, M. Prieto and J. L. Thewalt, *Biochimica Et Biophysica Acta-Molecular and Cell Biology of Lipids*, 2008, **1781**, 665-684.
137. D. S. Y. Yeo, R. Chan, G. Brown, L. Ying, R. Sutejo, J. Aitken, B. H. Tan, M. R. Wenk and R. J. Sugrue, *Virology*, 2009, **386**, 168-182.
138. C. S. Adamson and I. M. Jones, *Reviews in Medical Virology*, 2004, **14**, 107-121.
139. P. Palestini, C. Calvi, E. Conforti, L. Botto, C. Fenoglio and G. Miserocchi, *American Journal of Physiology-Lung Cellular and Molecular Physiology*, 2002, **282**, 1382-1390.
140. X. J. Liang and Y. G. Huang, *International Journal of Biochemistry & Cell Biology*, 2002, **34**, 1248-1255.
141. Grunstone, Harwood and Padley, *The Lipid Handbook*, Chapman and Hall, London, 1995.
142. R. C. Macdonald and S. A. Simon, *Proceedings of the National Academy of Sciences of the United States of America*, 1987, **84**, 4089-4093.
143. H. M. Mansour and G. Zografi, *Langmuir*, 2007, **23**, 3809-3819.
144. R. Maget-Dana, *Biochimica Et Biophysica Acta-Biomembranes*, 1999, **1462**, 109-140.
145. D. Vollhardt and V. B. Fainerman, *Advances in Colloid and Interface Science*, 2000, **86**, 103-151.
146. A. Krishnan, C. A. Siedlecki and E. A. Vogler, *Langmuir*, 2003, **19**, 10342-10352.
147. A. Krishnan, Y. H. Liu, P. Cha, D. Allara and E. A. Vogler, *Journal of the Royal Society Interface*, 2006, **3**, 283-301.
148. R. E. Heikkila, C. N. Kwong and D. G. Cornwell, *Journal of Lipid Research*, 1970, **11**, 190-194.

149. M. M. Hossain, K.-i. Iimura and T. Kato, *Journal of Colloid and Interface Science*, 2008, **319**, 295-301.
150. Eftaiha, Brunet and Paige, in *Current Microscopy Contributions to Advances in Science and Technology*, eds. Mendez-Villas and Dias, Editon edn., 2012, vol. 2.
151. R. S. Davidson and M. M. Hilchenbach, *Photochemistry and Photobiology*, 1990, **52**, 431-438.
152. M. I. Angelova and D. S. Dimitrov, *Faraday Discussions*, 1986, **81**, 303-311.
153. P. Walde, K. Cosentino, H. Engel and P. Stano, *Chembiochem*, 2010, **11**, 848-865.
154. L. A. Bagatolli, T. Parasassi and E. Gratton, *Chemistry and Physics of Lipids*, 2000, **105**, 135-147.
155. L. R. Montes, A. Alonso, F. M. Goni and L. A. Bagatolli, *Biophysical Journal*, 2007, **93**, 3548-3554.
156. S. L. Veatch, *Methods in Molecular Biology*, 2007, **398**, 59-72.
157. J. Juhasz, J. H. Davis and F. J. Sharom, *Biochemical Journal*, 2010, **430**, 415-423.
158. T. Baumgart, A. T. Hammond, P. Sengupta, S. T. Hess, D. A. Holowka, B. A. Baird and W. W. Webb, *Proceedings of the National Academy of Sciences of the United States of America*, 2007, **104**, 3165-3170.
159. A. V. Samsonov, I. Mihalyov and F. S. Cohen, *Biophysical Journal*, 2001, **81**, 1486-1500.
160. C. G. Brouillette, J. L. Jones, T. C. Ng, H. Kercret, B. H. Chung and J. P. Segrest, *Biochemistry*, 1984, **23**, 359-367.
161. T. H. Bayburt, Y. V. Grinkova and S. G. Sligar, *Nano Letters*, 2002, **2**, 853-856.
162. I. G. Denisov, Y. V. Grinkova, A. A. Lazarides and S. G. Sligar, *Journal of the American Chemical Society*, 2004, **126**, 3477-3487.
163. A. Nath, W. M. Atkins and S. G. Sligar, *Biochemistry*, 2007, **46**, 2059-2069.
164. F. Hagn, M. Etzkorn, T. Raschle and G. Wagner, *Journal of the American Chemical Society*, 2013, **135**, 1919-1925.
165. S. Graslund, P. Nordlund, J. Weigelt, J. Bray, B. M. Hallberg, O. Gileadi, S. Knapp, U. Oppermann, C. Arrowsmith, R. Hui, J. Ming, S. Dhe-Paganon, H. W. Park, A. Savchenko, A. Yee, A. Edwards, R. Vincentelli, C. Cambillau, R. Kim, S. H. Kim, Z. Rao, Y. Shi, T. C. Terwilliger, C. Y. Kim, L. W. Hung, G. S. Waldo, Y. Peleg, S. Albeck, T. Unger, O. Dym, J. Prilusky, J. L. Sussman, R. C. Stevens, S. A. Lesley, I. A. Wilson, A. Joachimiak, F. Collart, I. Dementieva, M. I. Donnelly, W. H. Eschenfeldt, Y. Kim, L. Stols, R. Wu, M. Zhou, S. K. Burley, J. S. Emtage, J. M. Sauder, D. Thompson, K. Bain, J. Luz, T. Gheyi, F. Zhang, S. Atwell, S. C. Almo, J. B. Bonanno, A. Fiser, S. Swaminathan, F. W. Studier, M. R. Chance, A. Sali, T. B. Acton, R. Xiao, L. Zhao, L. C. Ma, J. F. Hunt, L. Tong, K. Cunningham, M. Inouye, S. Anderson, H. Janjua, R. Shastry, C. K. Ho, D. Y. Wang, H. Wang, M. Jiang, G. T. Montelione, D. I. Stuart, R. J. Owens, S. Daenke, A. Schutz, U. Heinemann, S. Yokoyama, K. Bussow, K. C. Gunsalus, S. G. Consortium, B. Architecture Fonction Macromol, S. G. Ctr, C. S. G. Consortium, C. Integrated, S. Function, I. S. P. Ctr, S. Joint Ctr, Genomics, M. C. S. Genomics, X. R. C. New York Struct Genomi, N. E. S. G. Consortium, O. P. P. Facility, P. Sample, P. Facility, R. S. G. Max Delbruck Ctr Mol Med and S. C. Proteomics, *Nature Methods*, 2008, **5**, 135-146.

166. F. W. Studier, *Protein Expression and Purification*, 2005, **41**, 207-234.
167. A. L. Ksenofontov, E. N. Dobrov, N. V. Fedorova, V. A. Radyukhin, G. A. Badun, A. M. Arutyunyan, E. N. Bogacheva and L. A. Baratova, *Molecular Biology*, 2011, **45**, 634-640.
168. A. Shishkov, E. Bogacheva, N. Fedorova, A. Ksenofontov, G. Badun, V. Radyukhin, E. Lukashina, M. Serebryakova, A. Dolgov, A. Chulichkov, E. Dobrov and L. Baratova, *Febs Journal*, 2011, **278**, 4905-4916.
169. F. Ahmad and C. C. Bigelow, *Journal of Protein Chemistry*, 1986, **5**, 355-367.
170. R. L. Baldwin, *Biophysical Journal*, 1996, **71**, 2056-2063.
171. X. Tadeo, B. Lopez-Mendez, D. Castano, T. Trigueros and O. Millet, *Biophysical Journal*, 2009, **97**, 2595-2603.
172. J. C. Stachowiak, E. M. Schmid, C. J. Ryan, H. S. Ann, D. Y. Sasaki, M. B. Sherman, P. L. Geissler, D. A. Fletcher and C. C. Hayden, *Nature Cell Biology*, 2012, **14**, 944-949.
173. M. Olejniczak, Z. Gdaniec, A. Fischer, T. Grabarkiewicz, L. Bielecki and R. W. Adamiak, *Nucleic Acids Research*, 2002, **30**, 4241-4249.
174. J. Modrof, S. Becker and E. Muhlberger, *Journal of Virology*, 2003, **77**, 3334-3338.
175. U. C. Chaturvedi and R. Shrivastava, *Fems Immunology and Medical Microbiology*, 2005, **43**, 105-114.
176. C. Leyrat, M. Renner, K. Harlos, J. T. Huiskonen and J. M. Grimes, *Structure*, 2014, **22**, 136-148.
177. M. S. Shahrabadi and P. W. K. Lee, *Journal of Clinical Microbiology*, 1988, **26**, 139-141.
178. J. S. Rossman and R. A. Lamb, *Annual Review of Cell and Developmental Biology, Vol 29*, 2013, **29**, 551-569.
179. J. B. Hutchison, R. M. Weis and A. D. Dinsmore, *Langmuir*, 2012, **28**, 5176-5181.
180. A. Alfadhli, D. Huseby, E. Kapit, D. Colman and E. Barklis, *Journal of Virology*, 2007, **81**, 1472-1478.
181. J. C. Stachowiak, C. C. Hayden and D. Y. Sasaki, *Proceedings of the National Academy of Sciences of the United States of America*, 2010, **107**, 7781-7786.
182. A. V. Shnyrova, J. Ayllon, Mikhalyov, II, E. Villar, J. Zimmerberg and V. A. Frolov, *Journal of Cell Biology*, 2007, **179**, 627-633.
183. R. J. King and M. C. Macbeth, *Biochimica Et Biophysica Acta*, 1981, **647**, 159-168.

6 Materials and Methods

6.1 General

All chemicals were used as received unless stated otherwise. All solvents used were reagent grade from Fischer Scientific, (Thermo Fisher Scientific, Loughborough, UK). Water was purified using a Milli-Q system (Millipore, Billerica, MA, USA) to a resistivity of 18.2 MΩ.

Phosphate buffered saline (PBS) pH 7.4 was purchased from Invitrogen, Paisley, UK, at 10x concentration (105 mM KH_2PO_4, 305 mM Na_2HPO_4, 1.54 M NaCl) and diluted to a working stock of 1x, the pH readjusted to 7.4 with HCl. All buffer components were purchased from Sigma Aldrich (Sigma-Aldrich Ltd, Dorset, UK).

Factor Xa was purchased from Novagen (Novagen, Merck Chemicals Ltd, Nottingham, UK). PreScission® Protease and Glutathione-Sepharose B beads was purchased from GE Healthcare (GE Healthcare Life Sciences, Buckinghamshire, UK). Protein Markers, Restriction Enzymes and Pfu polymerase were purchased from NEB (New England Biolabs (UK) Ltd, Hertfordshire, UK). Ni-NTA beads were purchased from Quiagen (Quiagen, Manchester, UK)

All lipids were obtains as solids. DPPC (1,2-dipalmitoyl-sn-glycero-3-phosphocholine) was purchased from Bachem AG, Bubendorf, Switzerland. DOPC (1,2-dioleoyl-sn-glycero-3-phosphocholine), DPPS (1,2-dipalmitoyl-sn-glycero-3-phospho-L-serine) and cholesterol were Sigma brand (Sigma-Aldrich Ltd, Dorset, UK). POPS (1-palmitoyl-2-oleoyl-sn-glycero-3-phospho-L-serine) and Egg Sphingomyelin were purchased from Avanti Polar Lipids (Avanti Polar Lipids, Alabama, UK). Lipids were dissolved in chloroform or 3:1 chloroform: methanol and stored at -20°C.

6.2 Expression and Purification of hRSV-M

A pET16b vector containing the ORF of M protein was transformed into $CaCl_2$ competent *E. coli* BL21(DE3)pLysS by heat shock transformation. After culturing of a small overnight starter culture, the bacteria were grown in ZYM-5052 auto-inducing media with Ampicillin (100 µg/mL) and Chloramphenicol (50 µg/mL) at 37^{o}C for 8 hours, then 20^{o}C for 48 hours until no change in the OD600nm was observed. The cells were harvested by centrifugation of the culture at 5000 x g for 15 minutes.

For protein extraction, the *E.Coli* pellet was resuspended in 1/20th the culture volume of Tris based buffer (20 mM Tris-HCl, 0.2 M NaCl, 5 mM $CaCl_2$ pH 7.4) with Lysozyme (1µg/mL) and chilled in ice for 30 minutes. DNase 1 (1 µg/mL) and RNase A (1 µg/mL) were added and the cells lysed by sonication. CHAPS (8 mM) was added and the lysate was centrifuged at 50,000 x g for 30 minutes; removing the supernatant. Imidazole (0.05 M final concentration) and Ni-NTA agarose beads (50% suspension, 0.75 mL per L of culture) were added and the mixture placed on a carousel for 30 minutes at 4^{o}C. The mixture was centrifuged at 100 x g for 2 minutes and the supernatant discarded. The beads were resuspended in 50 ml Tris buffer with Imidazole (0.05 M) and loaded onto a column. The liquid was allowed to flow through under gravity, before the beads were washed with 50 ml Tris buffer with Imidazole (0.1 M). The protein was eluted from the Ni-NTA beads using successive washes of 10 ml Tris buffer with increasing concentrations of imidazole (0.2 – 0.5 M) and the fractions analyzed by SDS-PAGE. Fractions containing the protein were dialysed into Tris buffer and stored at 4^{o}C. The His-tag was removed using Factor Xa enzyme, as per the manufacturer's instructions (Novagen, Merck Chemicals Ltd, Nottingham, UK).

6.3 Cloning, Expression and Purification of Inf-M1

6.3.1 Cloning

Template plasmid containing the M1 gene was supplied by collaborators and was amplified using the Pfu DNA polymerase according to manufacturers instructions and the primers described below, containing EcoRI and XhoI restriction sites, followed by purification using a QIAquick PCR purification kit (Quiagen). The target plasmid pGEX-6p-1, and the amplified gene were restricted using EcoRI and XhoI according to the manufacturer's instructions and purified using a QIAquick gel extraction kit (Quiagen). The restricted plasmid and gene were ligated overnight with T4 polymerase and transformed into *E.Coli* XL1-Blue and the grown overnight on ampicillin containing LB-Agar plates. Colonies were screen by colony PCR and positive colonies were picked to be cultured and used to harvest more of the cloned plasmid.

Inf-M1 primers:

Forward Primer: CACCCCGAATTCACCATGAGTCTTCTAACCGAGGT

Reverse Primer: CGACGGCCGCTCGAGACTTGAACCGTTGCATC

6.3.2 Expression and Purification

pGEX-6P-1-Inf-M1 was transformed into $CaCl_2$ competent *E. coli* BL21(DE3) by heat shock transformation. An overnight starter culture of 10ml LB medium with Ampicillin (100 µg/mL) was inoculated with the transformed *E.Coli*. A 2 Litre Bioreactor (Sartorius, Goettingen, Germany) was set up, containing 2L ZYM-5052 autoinduction media with 100uL Antifoam A (Sigma-Aldrich), Ampicillin (100 µg/mL) and Chloramphenicol (50 µg/mL). This was inoculated with 10ml of the overnight starter culture. The bioreactor was kept agitated by a mixing motor @ 1000rpm, and had a constant compressed air supply piped into the bottom of the reactor. The culture was heated to 37°C using a heating jacket for 5 hours, and then the temperature reduced to 20°C. The OD 600 nm was monitored throughout the experiment and when the value stopped increasing (usually 24 hrs), the cells were harvested by centrifugation of the culture at 5000 x g for 15 minutes.

For protein extraction, the *E.Coli* pellet was resuspended in $1/20^{th}$ the culture volume of Phosphate buffer (50 mM NaH_2PO_4, 0.2 M NaCl, pH 7.4 pH 7.4) with Lysozyme

(1μg/mL) and chilled in ice for 30 minutes. DNase 1 (1 μg/mL) and RNase A (1 μg/mL) were added and the cells lysed by sonication. CHAPS (8 mM) was added and the lysate was centrifuged at 50,000 x g for 30 minutes; removing the supernatant. Glutathione-Sepharose B beads (50% suspension, 1 mL per L of culture) were added and the mixture placed on a carousel for 1 hour at 4°C. The mixture was centrifuged at 100 x g for 2 minutes and the supernatant discarded. The beads were resuspended in 50 ml Phosphate buffer and loaded onto a column. The liquid was allowed to flow through under gravity, before the beads were washed with 50 ml Phosphate buffer. The beads were then removed and treated with 50mM reduced glutathione. The supernatant was dialysed into Phosphate buffer with a minimum 20x volume, and then PreScission® Protease added (0.5 μl per ml) and incubated overnight at 4°C. Afterwards, Glutathione-Sepharose B beads (1ml) were added and the mixture placed on a carousel for 1 hour at 4°C. The supernatant was removed and applied to a Superose 12 HR 10/30 (GE Healthcare) column equilibrated with Phosphate buffer. The column was ran at a rate of 0.5 ml per minute and fractions of 0.5 ml collected. Fractions were analyzed by SDS-PAGE. Fractions containing the protein were dialysed into PBS and stored at 4°C.

6.4 Protein Characterisation

6.4.1 SDS-Page Gel electrophoresis

SDS-Page gels were made using the Biorad Mini-Protean Equipment. The gels used were 12.5 % acrylamide gels, with the following compositions for 1 gel:
12.5 % Resolving Gel:
H_2O – 1.75 ml
Resolving buffer – 1.25 ml
30 % Acrylamide – 2 ml
10 % Ammonium Persulphate – 25 μl
TEMED – 5 μl

4 % Stacking Gel:

H_2O – 1.15 ml
Stacking buffer – 0.5 ml
30 % Acrylamide – 0.335 ml
10 % Ammonium Persulphate – 15 µl
TEMED – 2.5 µl

SDS Running buffer:
Glycine – 196 mM
3.6 % Sodium Dodecyl Sulphate
Tris-HCl – 50 mM
pH 8.3 using HCl

The gel was assembled as described in the manufacturer's instructions. The proteins samples to be run on the gel were mixed 1:1 with SDS loading buffer (50 mM Tris-HCl pH 6.8, 2% SDS, 10% glycerol, 1% β-mercaptoethanol, 12.5 mM EDTA, 0.02 % bromophenol blue) and heated at 95^{o}C for 15 mins. The gel was placed into a tank filled with running buffer and 10-20 µl of the sample was then loaded into the gel. The electrophoresis power pack was set to 200 V for 40 mins and the gel ran.
The gel was then stained with 0.05 % coomassie blue stain and destained with 10 % methanol / 10 % acetic acid solution, to show the protein as blue bands on the gel. Along with the samples to be analysed, a maker was also always added to estimate the size of the protein's on the gel.

6.4.2 Protein Concentration Measurement

A quartz cuvette filled with 1 ml of 6M Guanidinium Hydrochloride was used as a blank in a UV spectrometer at 280 nm. Sequentially, 5 µl, 10 µl, 15 µl and 20 µl of protein solution were added to the cuvette and the absorbance recorded. Absorbance values were corrected for the change in volume (A(Corr)).

$$A(Corr) = A\frac{(V_0 + V)}{V_0}$$

Equation 29

Using a variation of the Beer-Lambert law:

$$A(Corr) = \frac{\varepsilon.x.V}{V_0}$$

Where ε is the absorption coefficient of the protein ($M^{-1}cm^{-1)}$ and x is the protein concentration (M). A plot of A(corr) against V gave a straight line with a gradient $(\varepsilon x)/V_0$ ad so x can be calculated.

Values for ε were calculated based on their amino acid composition where:

$$\varepsilon(protein) = [n(Tyr) \times \varepsilon(Tyr)] + [n(Trp) \times \varepsilon(Trp)] + [n(Cystine) \times \varepsilon(Cystine)]$$

Using ε(Tyr) = 1285, ε(Trp) = 5685 and ε(Cystine) = 125 $M^{-1}cm^{-1}$
From this, values of ε = 24220 $M^{-1}cm^{-1}$ were used for hRSV-M, and ε = 13075 $M^{-1}cm^{-1}$ for Inf-M1.

6.4.3 Mass Spectrometry

Samples were processed by the Mass Spectrometry unit at Durham University.
For routine mass spectrometry, samples were analysed by MALDI-TOF mass spectrometry with a sinapinic matrix on a Bruker Daltonics Autoflex TOF/TOF.
For MS/MS experiments, samples were run on a LTQ FT (ThermoFinnigan) coupled to a liquid chromatography system.

6.4.4 Differential Scanning Fluorimetry

A 96 well plate was filled with 2 µl of solution from a Hampton Solubility and Stability Screen (see Appendix) using a Innovadyne pipetting robot. Protein of concentration 0.1-0.5 mg/ml was mixed with SYPRO orange 5000X (Sigma-Aldrich) to a final dye concentration of 10X and 18µl added to each well. The plate was sealed and centrifuged at 1000 rpm for 2 minutes. The plate was then placed into a Applied Biosystems 7500 FAST real time PCR system. The samples were then heated for 24

to 95°C at a rate of 1°C per minute and the fluorescence data collected using filter set 3.

6.4.5 ICPMS

hRSV-M was incubated with 5mM $CaCl_2$ for one hour, followed by salt exchange using a PD-10 desalting column (GE Healthcare) equilibrated in 10 mM MOPS, pH 7.4, with the effluent collected in 0.5ml fractions. The protein concentration of each fraction was determined before continuing. 3 ml samples were prepared consisting of 2.4 ml Nitric acid, 300 µl H_2O and 300 µl of protein fraction. Alongside this, standards of CaCl2 were prepared with the same component consistency as the protein samples (40 ml Nitric acid, 5 ml buffer, 5 ml water) at concentrations of 10 ppm, 1 ppm, 100 ppb and 10 ppb. Samples and standard were then loaded into an Inductively coupled plasma-mass spectrometer (ICP-MS) (Thermo X-series) with Cetac ASX510 autosampler. The spectrometer was set to measure calcium at 40.078 Da and the samples processed.

6.4.6 Microscale Thermophoresis

hRSV-M was labelled with the dye NT-647 (L001 Monolith™ NT.115 Protein Labelling Kit RED-NHS**)** in a 1:1 ratio according to the manufacturers instructions. The protein was then buffer exchanged into MST optimised buffer (50 mM Tris-HCl, 150 mM NaCl, 0,05 % Tween-20). A set of serial dilutions of $CaCl_2$ in MST optimised buffer were prepared (10 nM – 10 mM final concentration) and 20 µM final concentration of hRSV-M-NT-647 added to each. 4 µl of each sample was then loaded into capillary tubes and placed into the Monolith NT.115 Instrument (NanoTemper Technologies GmbH, Munchen, Germany). The experiment was then run using preset settings and the resulting data analysed on the software's bespoke tools.

6.4.7 Circular Dichroism Spectroscopy

Protein samples were dialysed into 1mM Tris pH7.4 or 5mM phosphate buffer pH 7.4 with any additives before use. A sample of the same buffer was used as a blank. Samples were placed into a 0.2 cm pathlength quartz cuvette and loaded into a Jasco J-810 Spectropolarimeter. The temperature was held at 25°C using a peltier controlled water jacket. Spectra were collected between 260 and 180 nm at a rate of 10 nm/min, a pitch of 0.5 nm, a bandwidth of 1 nm and a response time of 2 s. 8 spectra were collected for each sample and averaged for analysis. Protein samples were diluted down until the detector was not saturated within the collection range. The blank buffer spectra were subtracted from the collected protein spectra and then subjected to analysis. Data points for which the HT voltage was over 600 were discarded as unreliable. The package CDPro was used for analysis, containing the secondary structure algorithms SELCON3, CDSSTR and CONTIN/LL. All viable reference protein sets were used, but dataset 10 resulted in the best fittings for all proteins studied.

6.5 Membrane Interactions

6.5.1 Langmuir Isotherms

Experiments were carried out on a 150 x 70 mm Langmuir trough (102 M, Nima Technology Ltd, Coventry, UK) with two moveable Delrin barriers. Before and after each experiment the trough was thoroughly cleaned using Kimwipes and either isopropyl alcohol or chloroform / methanol 8:2. With the barriers open, the trough was filled with PBS pH 7.4, the Wilhelmy plate attached to the pressure sensor and the surface cleaned with an aspirator. The barriers were then closed and the pressure monitored. The surface was cleaned further until the change in pressure was less than 0.2 mN m^{-1} in total. The required mass of lipids dissolved in chloroform (+ methanol if required) were deposited on the surface using a glass micro-syringe and allowed 15 minutes to equilibrate. For pressure/area experiments with protein (with or without lipids), the protein was added first to the surface with a micropipette followed

immediately by the lipid if required and given 15 minutes to equilibrate. Isotherms were collected by closing the barriers at a rate of 8 cm^2 per minute and the change in pressure recorded every 0.2 seconds. For protein only experiments at a fixed area, the change in pressure was recorded without any equilibration time, starting from when the protein was first added. For protein being added to a fixed area lipid monolayer, the lipids were deposited on the surface first, followed by injection of the protein just underneath the surface of the subphase and data immediately recorded.

6.5.2 Brewster Angle Microscopy

The equipment used in this experiment is shown in figure 43. The Langmuir trough was filled with PBS and the surface cleaned by aspiration. Light from a p-polarised 633 nm helium-neon laser (CVI Melles-Griot, Leicester, UK) was passed through a Glan-Taylor Polariser and adjusted with mirrors so it made an incident angle of 53° to the subphase surface. The CCD video camera (OPtem Zoom 70, Qioptik Imaging Solutions, Newport, NY, USA) was also set to this angle to capture reflected light. The angle of the incident beam was adjusted slightly until no reflection could be seen from the clean subphase surface. Samples on the subphase surface were then set up in the same manner as Langmuir isotherm experiments. Images were recorded and saved manually during the experiment.

Fluorescent labelling of protein

Either FITC (10 mM in DMSO) or NBD-Cl (10mM in DMF) was added in a 1:1 molar ratio to protein in its storage buffer and incubated at room temperature for one hour. The protein was then applied to a PD-10 desalting column equilibrated in storage buffer, mand eluted with further buffer. The eluted protein was analysed by UV-Vis spectroscopy at 280 nm (protein) and 494 nm for FITC (ε = 68000 M^{-1} cm^{-1}) or 480 nm for NBD (ε = 25000 M^{-1} cm^{-1}) to determine the extent of labelling.

6.5.3 Giant Unilamellar Vesicle preparation

10 µg of lipids in chloroform were dried onto the conductive sides of two ITO coated slides (30-60 Ω/sq, Sigma-Aldrich) for at least 1 hour in a desiccator. A nitrile-o-ring was lightly covered in vacuum grease and the slides with dry lipids pointing inwards were then assembled separated by the o-ring with 170µl of sucrose solution (5 mM Phosphate buffer pH 7.4, 300 mM Sucrose) filling the well. The slides were brought into in contact with copper strips connected to a programmable function generator. The whole assembly was then placed inside a thermostatically controlled oven. The entire apparatus was pre-heated to 70°c and maintained for the electroformation steps. The function generator was then used to pass a current gradient through the cell with the following steps:

Step	Time (hr:min)	Start Voltage (V)	End Voltage (V)	Frequency (Hz)	Wave form
1	0:10	0.1	1.2	10	Sine
2	3:00	1.2	1.2	10	Sine
3	0:20	1.2	1.2	5	Square

Table 23 - Function generator settings for GUV formation

Following completion of the electroformation steps, the apparatus was slowly cooled from 70°C to 20°C over 3 hours. The GUVs were then removed and ready for use.

6.5.4 Confocal Microscopy

A Teflon coated well was made and glued on top of a glass cover slip. This was then treated with 1mg/ml BSA for 5 hours to passivate the surface, before being rinsed with 5 mM Phosphate buffer pH 7.4. For experiments using GUVs only, the well was filled with 1 ml of 5 mM Phosphate buffer, ~300 mM Glucose which had been adjusted to the same osmotic strength as the sucrose solution by adding more phosphate buffer. Osmotic strength was measured using a Osmomat® 030 (Gonotec, Berlin, Germany). The 5 µl of GUVs were then added to the solution, where they sank to the bottom of the well. For experiments where protein was to be added, the osmotic

strength of the fluorescent protein was measured and both the glucose and sucrose solutions were matched to this osmotic strength. The protein was then added to the well after the GUVs to a final concentration of 5 μM.

The samples were observed using either a Biorad Microradience 2000 (Biorad, Hertfordshire, UK) or a Zeiss 510 Meta (Carl Zeiss, Cambridge, UK). Rh-PE was excited using a 543.365 nm GreenNe Laser and fluorescence detected with a photomultiplier tube with an E570nm Longpass filter. NBD-PE and hRSV-M-FITC were excited using a 488.0 nm Argon Laser and fluorescence detected with a photomultiplier tube with a HQ530/60 nm Bandpass filter. Images were processed using LSM Image browser, given scale bars and false colour.

6.5.5 MSPE3D1 Nanodiscs

The gene for protein MSPE3D1 was supplied in a PET-28a vector containing a 6xHis tag sequence. The protein was expressed and purified according to instructions from the Sligar lab, University of Illinois. The plasmid was transformed into E.Coli BL21 DE3 and cultured in 1L LB medium containing 25 μg Kanamycin at 37C. When the OD600 reached 0.6, expression was induced with 1mM IPTG and the temperature reduced to 28°C. After 3 hours the cells were harvested by centrifugation at 5000 x g for 15 minutes. For extraction and purification, the cells were resuspended in PBS with 1% Triton X-100 and lysed by sonication. The lysate was centrifuged at 50,000 x g for 30 minutes and the supernatant removed. The supernatant was incubated with Ni-NTA beads (0.75 ml per L of culture) for 30 mins before loading into a column. The beads were then washed with 40 ml each of: **1**. 40 mM Tris/HCl, 0.3 M NaCl, 1% Triton, pH 8.0. **2**. 40 mM Tris/HCl, 0.3 M NaCl, 50 mM sodium cholate, pH 8.0, 20 mM imidazole. **3**. 40 mM Tris/HCl, 0.3 M NaCl, 50 mM imidazole, pH 8.0. Finally the protein was eluted in 40 mM Tris/HCl, 0.3 M NaCl, 0.5 M Imidazole. The protein was then dialysed into 10 mM Tris/HCL, 0.1 M NaCl, 0.5 mM EDTA, pH 7.4 and stored at 4°C.

The lipids to be constituted into Nanodiscs were dried into a thin layer inside a small round bottom flask on a rotary centrifuge, followed by drying in a desiccator

overnight. Buffer containing 10 mM Tris/HCL, 0.1 M NaCl, 0.5 mM EDTA, 100 mM Sodium Cholate was added to give a final lipid concentration of 50 mM. The lipids are solubilised by vortexing the flask, heating it under hot tap water, and sonicating in an ultrasonic bath until the solution is clear, and no lipid remains on the walls of the flask. MSPE3D1 and the lipid stock are then mixed together in the following rations depending on the lipids used:

Lipid	Optimal Ratio for MSP1E3D1	Incubation temperature
DPPC	170:1	37 °C
DMPC	150:1	25 °C
POPC / POPS	130:1	4 °C

Table 24 - Incubation conditions for formation of lipid nanodiscs

The final sodium cholate concentration is adjusted to between 12 – 40 nM if required. Nanodiscs are then formed by dialysing the sample against cholate-free buffer over 24 hours, with a minimum volume of 1000x that of the nanodisc mixture. The crude mixture of nanodiscs was finally purified by size exclusion chromatography on a HiLoad 16/600 Superdex 200 PG column (GE Healthcare), coupled to an inline Dynamic light scattering (DLS) machine (Zetasizer μV, Malvern). The DLS was attached to identify nanodiscs of the correct diameter as they came off the column.

6.5.6 Cryo-Electron Microscopy

The Nanodisc and hRSV-M mixture were then prepared for cryo-electron microscopy by loading 3-μl aliquots onto freshly glow-discharged c-flat holey carbon grids (CF-22-4C, Protochips Inc.) held at 4°C and 100% humidity in a Vitrobot vitrification robot (FEI). Grids were blotted for 4 s prior to being frozen by plunging into a bath of liquid nitrogen-cooled ethane slush. Vitrified specimens were imaged at low temperature in a JEOL 2200 FS cryo-microscope equipped with Gatan 626 or Oxford CT3500 cryo-stages. Low-dose (10 e/Å^2), energy-filtered images (slit width, 20 eV) were recorded on a Gatan ultrascan 16-megapixel charge-coupled-device camera at a magnification of 100,000×, corresponding to a sample frequency of 1.03 Å/pixel.

6.5.7 DLS

Samples for DLS were placed into 10 µl volume, 1 cm pathlength disposable cuvettes and placed into a Zetasizer µV DLS machine (Malvern Instruments, Worcestershire, UK). The IR laser was at 830 nm wavelength, and the scattering detector at 90° to the sample. Measurements were performed in triplicate and averaged. Analysis of collected data was done using a protein routine in the Zetasizer software.

7 Appendix

Solubility and Stability Screen HT Formulation for DSF							
Hampton Research - Copyright 2012							
Reagent #	**Well #**	**[Additive 1]**	**[Additive 1] units**	**Additive 1**	**[Additive 2]**	**[Additive 2] units**	**Additive 2**
01	A01	100	% v/v	Water			
02	A02	75	% w/v	Trichloroacetic acid			
03	A03	250	mM	L-Arginine			
04	A04	250	mM	L-Arginine	250	mM	L-Glutamic acid
05	A05	500	mM	Glycine			
06	A06	500	mM	L-Proline			
07	A07	120	mM	L-Histidine			
08	A08	500	mM	β-Alanine			
09	A09	500	mM	L-Serine			
10	A10	500	mM	L-Arginine ethyl ester dihydrochloride			
11	A11	500	mM	L-Argininamide dihydrochloride			
12	A12	500	mM	6-Aminohexanoic acid			
13	B01	500	mM	Gly-gly			
14	B02	200	mM	Gly-gly-gly			
15	B03	5	% w/v	Tryptone			
16	B04	2,500	mM	Betaine monohydrate			
17	B05	750	mM	D-(+)-Trehalose dihydrate			
18	B06	2,000	mM	Xylitol			
19	B07	2,000	mM	D-Sorbitol			
20	B08	2,000	mM	Sucrose			
21	B09	500	mM	Hydroxyectoine			

22	B 10	2,500	mM	Trimethylamine N-oxide dihydrate			
23	B 11	2,000	mM	Methyl-α-D-glucopyranoside			
24	B 12	10	% v/v	Triethylene glycol			
25	C 01	500	mM	Spermine tetrahydrochloride			
26	C 02	500	mM	Spermidine			
27	C 03	500	mM	5-Aminovaleric acid			
28	C 04	500	mM	Glutaric acid			
29	C 05	80	mM	Adipic acid			
30	C 06	500	mM	Ethylenediamine dihydrochloride			
31	C 07	500	mM	Guanidine hydrochloride			
32	C 08	500	mM	Urea			
33	C 09	500	mM	N-Methylurea			
34	C 10	200	mM	N-Ethylurea			
35	C 11	30	% w/v	N-Methylformamide			
36	C 12	3	% w/v	Hypotaurine			
37	D 01	100	mM	TCEP hydrochloride			
38	D 02	10	mM	GSH (L-Glutathione reduced)	10	mM	GSSG (L-Glutathione oxidized)
39	D 03	5	% w/v	Benzamidine hydrochloride			
40	D 04	100	mM	Ethylenediaminetetraacetic acid disodium salt dihydrate			
41	D 05	100	mM	Magnesium chloride hexahydrate	100	mM	Calcium chloride dihydrate
42	D 06	100	mM	Cadmium chloride hydrate	100	mM	Cobalt(II) chloride hexahydrate
43	D 07	1,000	mM	Non Detergent Sulfobetaine 195 (NDSB-195)			
44	D 08	1,000	mM	Non Detergent Sulfobetaine 201 (NDSB-201)			
45	D 09	1,000	mM	Non Detergent Sulfobetaine 211 (NDSB-211)			
46	D 10	1,000	mM	Non Detergent Sulfobetaine 221 (NDSB-221)			

47	D 11	1,000	mM	Non Detergent Sulfobetaine 256 (NDSB-256)			
48	D 12	500	mM	Taurine			
49	E0 1	500	mM	Acetamide			
50	E0 2	500	mM	Oxalic acid dihydrate			
51	E0 3	500	mM	Sodium malonate pH 7.0			
52	E0 4	500	mM	Succinic acid pH 7.0			
53	E0 5	5	% v/v	Tacsimate pH 7.0			
54	E0 6	25	% w/v	Tetraethylammoniu m bromide			
55	E0 7	25	% w/v	Cholin acetate			
56	E0 8	25	% w/v	1-Ethyl-3-methylimidazolium acetate			
57	E0 9	25	% w/v	1-Butyl-3-methylimidazolium chloride			
58	E1 0	25	% w/v	Ethylammonium nitrate			
59	E1 1	500	mM	Ammonium sulfate			
60	E1 2	500	mM	Ammonium chloride			
61	F0 1	500	mM	Magnesium sulfate hydrate			
62	F0 2	500	mM	Potassium thiocyanate			
63	F0 3	250	mM	Gadolinium(III) chloride hexahydrate			
64	F0 4	250	mM	Cesium chloride			
65	F0 5	250	mM	4-Aminobutyric acid (GABA)			
66	F0 6	500	mM	Lithium nitrate			
67	F0 7	500	mM	DL-Malic acid pH 7.0			
68	F0 8	500	mM	Lithium citrate tribasic tetrahydrate			
69	F0 9	250	mM	Ammonium acetate			
70	F1 0	250	mM	Sodium benzenesulfonate			
71	F1 1	250	mM	Sodium p-toluenesulfonate			
72	F1 2	1,000	mM	Sodium chloride			

73	G 01	1,000	mM	Potassium chloride			
74	G 02	700	mM	Sodium phosphate monobasic monohydrate	1,300	mM	Potassium phosphate dibasic
75	G 03	1,000	mM	Sodium sulfate decahydrate			
76	G 04	1,000	mM	Lithium chloride			
77	G 05	1,000	mM	Sodium bromide			
78	G 06	40	% v/v	Glycerol	400	mM	Lithium chloride
79	G 07	50	% v/v	Glycerol			
80	G 08	10	% v/v	Ethylene glycol			
81	G 09	10	% v/v	Polyethylene glycol 200			
82	G 10	5	% v/v	Polyethylene glycol monomethyl ether 550			
83	G 11	5	% w/v	Polyethylene glycol monomethyl ether 750			
84	G 12	50	% v/v	Formamide			
85	H 01	50	% v/v	Polypropylene glycol P 400			
86	H 02	25	% v/v	Pentaerythritol ethoxylate (15/4 EO/OH)			
87	H 03	10	% w/v	1,2-Propanediol			
88	H 04	3	% w/v	Polyethylene glycol monomethyl ether 1,900			
89	H 05	3	% w/v	Polyethylene glycol 3,350			
90	H 06	3	% w/v	Polyethylene glycol 8,000			
91	H 07	2	% w/v	Polyvinylpyrrolidone K15			
92	H 08	100	mM	6-O-α-D-Maltosyl-β-cyclodextrin			
93	H 09	10	mM	(2-Hydroxypropyl)-β-cyclodextrin			
94	H 10	80	mM	α-Cyclodextrin			
95	H 11	10	mM	β-Cyclodextrin			
96	H 12	50	mM	Methyl-β-cyclodextrin			